

**Structural Studies on Charge-Transport and Emission Properties of
Materials for Organic Light-Emitting Diodes**

Furitsu Suzuki

2017

Contents

Chapter 1

General Introduction

1.1. Backgrounds	1
1.2. Outline of this thesis	7
References	10

PART I

Clarification of the Relationship between Aggregated Structure and Charge Transport Property

Chapter 2

Multiscale Simulation of Charge Transport in a Host Material, mCP, for Organic

Light-Emitting Diodes

2.1. Introduction	16
2.2. Computational section	19
2.3. Results and discussion	29
2.3.1. Reorganization energies and electronic couplings	29
2.3.2. Charge transport simulations	32
2.4. Conclusion	48
References	49

Chapter 3

Effect of Structural and Energetic Disorders on Charge Hopping in Amorphous Organic Thin Layer Studied by Multiscale Charge Transport Simulation

3.1. Introduction	51
3.2. Computational section	54
3.3. Results and discussion	57
3.3.1. Molecular structures and reorganization energies	57
3.3.2. Electronic couplings and energetic disorders	63

3.3.3. Charge transport simulations	72
3.4. Conclusion	102
References	104

PART II

Development of the Methodology for Structural Refinement and Its Relation with the Emissive Property

Chapter 4

Refined Structure Determination of Blue-Emitting Tris(8-hydroxyquinoline) Aluminum(III) (Alq₃) by the Combined Use of CP/MAS ¹³C Solid-State NMR and First-Principles Calculation

4.1. Introduction	108
4.2. Experimental and computational Section	113
4.2.1. Computation	113
4.2.2. Experimental	122
4.3. Results and discussion	123
4.3.1. Isotropic chemical shifts of γ -Alq ₃	123
4.3.2. Isotropic chemical shifts of δ -Alq ₃	130
4.4. Conclusion	147
References	148

Chapter 5

Clarification of Isomeric Structures and the Effect of Intermolecular Interactions in Blue-emitting Aluminum Complex Alq₃ using First-principles ²⁷Al NMR Calculations

5.1. Introduction	153
5.2. Experimental and computational section	156
5.2.1. Experimental	156
5.2.2. Computations	157
5.3. Results and discussion	162
5.3.1. ²⁷ Al NMR of γ -Alq ₃	162

5.3.2. ^{27}Al NMR of $\delta\text{-Alq}_3$	166
5.4. Conclusion	175
References	176

Chapter 6

Probing Intermolecular Structures of β Sheet of Alanine Oligomer and Silk Fibroin by High Resolution ^1H NMR Spectroscopy with Ultra-Fast MAS under Ultra-High Field ^1H Resonant Frequency

6.1. Introduction	179
6.2. Experimental and computational section	181
6.2.1. Solid-state ^1H NMR experiments	181
6.2.2. Computations	181
6.3. Results and discussion	182
6.3.1. Solid-state ^1H NMR experiments	182
6.3.2. DQMAS solid-state ^1H NMR experiments	184
6.4. Conclusion	193
References	194

Summary	197
----------------	-----

List of Publications	203
-----------------------------	-----

Acknowledgements	210
-------------------------	-----

Chapter 1

General Introduction

1.1. Backgrounds

Organic light-emitting diodes (OLEDs) are one of the most attractive and promising devices for application to flexible ultra-thin displays and solid-state lighting source. In 1953, the first electroluminescence (EL) from organic compounds was observed by Bernanose et al. They applied an alternating electric field to thin polymer layers containing acridine dyes, and observed fluorescence from the organic dyes [1]. Helfrich et al. observed fluorescence resulting from the recombination of holes and electrons in anthracene single crystal under an applied electric field [2]. The first multi-layered OLEDs were reported in the pioneering work of Tang and VanSlyke in 1987 [3]. They have greatly improved the EL efficiency of OLEDs by the insertion of a hole transport layer between electrode and emissive/electron transport layer. Adachi et al. have further improved the EL efficiency using the multi-functional layered structures [4]. These early studies have emerged significant interest in OLEDs and have formed the basis of device structures of today's OLEDs. In general, materials for OLEDs are used in their amorphous aggregates. Hence, it is important to investigate electronic states of molecules by taking into account effects of surrounding molecules in the amorphous state. However, theoretical treatments of OLED compounds to date are far away from real devices, because electronic-state calculations are usually done for isolated molecules. One of the main purposes of this thesis is to establish a theoretical method for analyzing OLED characteristics as realistic as possible. Our multiscale simulation involves quantum chemical calculation of single molecules and molecular dynamics simulation of aggregated state, and link properties between single molecule and aggregated state. We would like to apply the method to investigate emission and charge transport properties of

OLED materials.

The charge-transport properties in organic thin films of the OLEDs is one of the most important factor. The optimization of the charge injection, charge transport, and charge blocking at the electrodes are essential to maximize the probability of recombination in the emissive layer. Among these factors, the charge blocking and the charge injection at the electrodes have often been discussed in terms of the energy of the highest occupied molecular orbital (HOMO) and the lowest unoccupied molecular orbital (LUMO) of the organic materials. Evaluation of the HOMO and the LUMO can be obtained using quantum chemical calculations for isolated molecules. However, the charge transport within an organic material is considered to strongly depend on the structure of the molecule not only in an isolated state and but also in an intermolecular aggregated state. In addition, it should be also noted that the materials for OLEDs are used not in crystalline state but in amorphous state in actual devices as described above. The crystallization sacrifices device performance and stability. However, understandings of charge transports in amorphous organic materials are limited. One of the reasons is that amorphous structures were hardly clarified is due to the difficulty of the analysis, although they were considered to be closely related with the charge-transport properties. Recently, some research groups [5-8] including our own [9, 10] have evaluated charge transport properties by quantum chemical calculations of the rate constant, k_{CT} , for charge hopping between two molecules. Although this method may lead to material design by taking into account the molecular structure, evaluating an amorphous system that is actually used in a device is difficult and so crystal structures are used. This causes uncertainty in the calculations. Also, the charge transfer rate constants between the two molecules were indirectly compared against the experimental charge carrier mobility [5, 7].

Since the pioneering works by Bässler et al. [11-13], evaluation of the charge transport

properties between the electrodes have been conducted energetically. However, because this approach including related ones [14-18] does not consider the organic molecule explicitly, it is somewhat difficult to link the macroscopic charge transfer and the microscopic molecular structure directly. A detailed study of the charge transfer processes between electrodes is thought to be possible using a combination of Monte Carlo simulations and the charge transfer rate constants between the two molecules. Such attempts have been made in recent years [19-26]. For example, Kwiatkowski et al. performed simulations of the charge mobility using a model structure of amorphous Alq₃ by approximating the Alq₃ molecule as a rigid body [19]. Although the absolute value of the experimental charge carrier mobility of Alq₃ could not be reproduced, they succeeded in explaining the difference between hole and electron mobility. This difference originated from the delocalization of the HOMO and the LUMO on the Alq₃ molecule. Lukyanov et al. constructed an Alq₃ model structure using molecular dynamics (MD) simulations without applying the rigid body approximation and investigated the influence of the force fields on the charge mobility in detail [20]. However, such investigations are still limited and nature of charge transport in organic thin layer is not fully understood. Also, there are a number of important molecules in OLEDs and the method should be applied to molecular systems other than Alq₃ to the development of excellent charge transfer materials.

In order to fabricate full-color displays or white solid-state lighting source, efficient emission of three primary colors, red-green-blue (RGB), is essential. Considerable effort has been devoted to improve the luminescence efficiency of emitting materials [27-32]. Among emissive materials, tris(8-hydroxyquinoline) aluminum(III) (Alq₃) has been a one of the most widely used material in OLEDs, since the seminal work of Tang et al. [3]. They used Alq₃ as an electron-transport and light-emitting layer. Alq₃ usually emits green fluorescence. However, recently, blue-emitting Alq₃ crystals in γ - and δ -polymorphs (γ - and δ -Alq₃) have been found [33-36].

The quantum yield of the blue-emitting Alq₃ is very high; almost double that of conventional Alq₃. Two isomeric forms of Alq₃ are known, one is called “*facial*” and the other is called “*meridional*”, as shown in Figure 1.1a and 1.1b. The *facial* isomer has C₃ symmetry with three equivalent ligands, while the *meridional* isomer has lower C₁ symmetry and its three ligands are non-equivalent. While the TD-DFT calculation predicted blue-shift emission for the *facial*-Alq₃ [37], Experimental investigations on the origin of the change in emission wavelength have been few and the origin is still controversial. Some researchers have considered that the difference of the isomeric state is the origin of the change in the emission wavelength [33, 36-46]. In contrast, other researchers assumed that the origin is intermolecular interaction [47-50], and definite conclusions still have not been drawn [34,51,52]. Therefore, further studies are needed to reveal the origin of the blue shift.

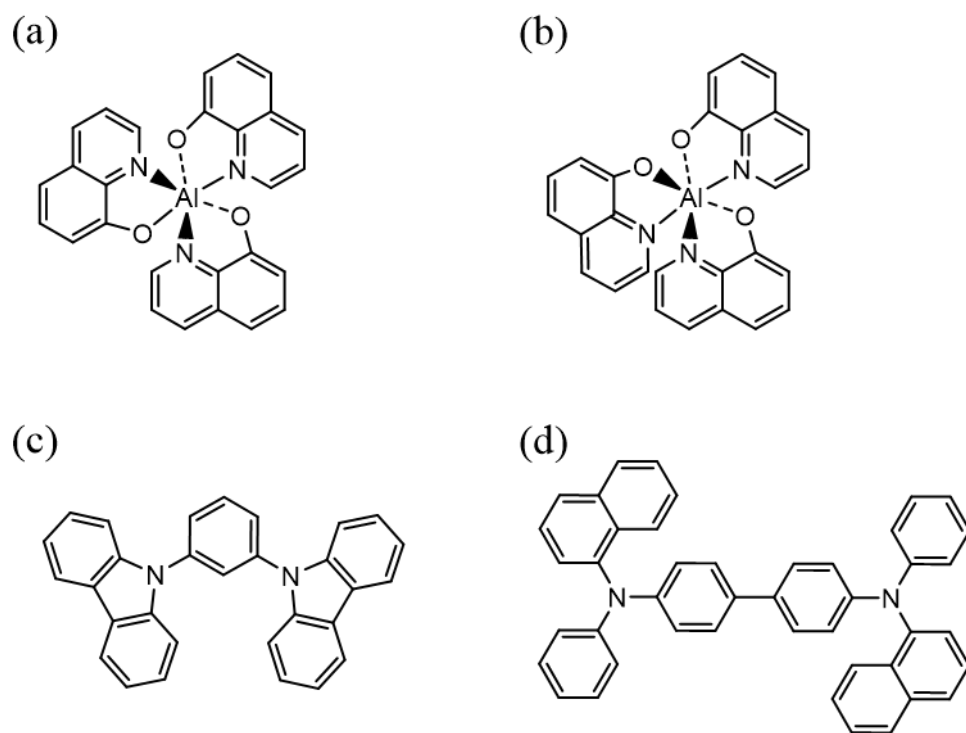


Fig. 1.1. Chemical structures of (a) Alq₃ in *facial* isomerization, (b) Alq₃ in *meridional* isomerization, (c) mCP and (d) α -NPD.

In general, the crystal structure is analyzed by X-ray diffraction analysis. However, the X-ray diffraction analysis of OLEDs materials, including Alq₃, is often rather difficult, because the crystals of OLEDs materials are sometimes disordered and contaminated by other polymorphs. In the paper by Brinkmann et al. [47], γ -Alq₃, which has been found to have blue emission, is considered to be composed of disordered *meridional* isomers according to X-ray diffraction analysis. In contrast, Muccini et al. suggested that the isomeric state of γ -Alq₃ is *facial* by X-ray diffraction analysis [36]. The first X-ray diffraction analysis of δ -Alq₃, which is another blue-emitting Alq₃ was performed by Braun et al., but to be incorrect because the crystals were contaminated by γ -Alq₃ [33]. The X-ray diffraction analysis of δ -Alq₃ was corrected by the same group [34, 51]. In the case of δ -Alq₃, another group reported a different crystal structure according to single-crystal X-ray diffraction analysis [53]. In light of these situations, structural analysis of Alq₃ other than X-ray diffraction method is eagerly desired. Kaji et al. has performed the cross polarization/magic-angle spinning (CP/MAS) ¹³C NMR experiments [42], which provide newly structural information on Alq₃. In the case of γ -Alq₃, the clear experimental evidence is obtained that γ -Alq₃ consists of *facial* isomers. On the other hand, resonance line splitting in the spectrum of δ -Alq₃ has not been completely understood whether its origin is intramolecular or intermolecular. As described above, the distinction of intra- and intermolecular effects is important for understanding the origin of blue-shifted emission.

The detailed structure analysis is important not only for synthetic-based materials but also for biological-based materials. The solid-state crystalline structures in those materials are often dominated by the driving force of forming maximum of hydrogen bonds [54]. Investigations of hydrogen bonds, particularly their geometry, provide profound understandings of the structures and properties of the materials. Single crystal X-ray diffraction is the most commonly used for those biological-based materials. However, determination of accurate positions of hydrogen

atoms in the hydrogen bond network is usually not possible via X-ray diffraction. Therefore, further studies are desired to reveal the structure-property relationships of these materials.

1.2. Outline of this thesis

In the Chapter 2, multiscale charge transport simulations are performed in organic amorphous thin films by explicitly considering organic molecules. The hopping transport simulations are based on Marcus theory and a Monte Carlo method. The amorphous layer is composed of *N,N'*-dicarbazole-3,5-benzene (mCP, Figure 1.1c), which is widely used as a host material in the emissive layer of blue-emitting organic light-emitting diodes. This layer is constructed using MD simulations. The hole mobility is calculated to be several times larger than the electron mobility. This trend is consistent with the experimentally obtained mobilities. It is also found that the charges are transported dominantly by diffusion-type character at low applied electric fields and the contribution of the drift-type character increased as the applied electric field increased. The total number of hops during the hopping transport process increased when there is a large electronic coupling, but the hopping direction is in both the forward and backward directions to the direction of the applied electric field, especially at low electric fields. The difference between the number of hops in the forward and the backward directions contributes to the actual charge transport. From the detailed analysis, it is turned out that the molecular pairs with a large electronic coupling do not necessarily contribute to the charge transport and can temporarily trap charges. The important molecular pairs which form effective charge transfer paths and improve charge mobilities are found, although the electronic coupling is not substantially large.

In the Chapter 3, contributions of diagonal (energetic) and off-diagonal (structural) disorder on charge transports in a crystal and an amorphous phase are clarified using molecular-based kinetic

Monte Carlo simulation. A amorphous and a crystal phase of *N,N'*-diphenyl-*N,N'*-bis(1-naphthyl)-1,1'-biphenyl-4,4'-diamine (NPD, Figure 1.1d) are used as example structures having small and large structural disorder. The origin of experimentally obtained bipolar charge transport property of NPD in amorphous phase, which is conventionally considered to be a hole-transporting material, is also examined. A sharp contrast is observed in charge transport pathways in the crystal (small structural disorder) and the amorphous (large structural disorder) phase: In the crystal phase, charges show linear and less diffusional transport, whereas complicated, strongly diffusive routes are observed in the amorphous phase, especially under low electric fields. Under high applied electric field the charge transport pathway in the amorphous phase becomes similar with that of the crystal phase. It is found that the structural disorder and applied electric field strength play a major role for the linearity of charge transport pathway. On the other hand, energetic disorder plays a significant role to the applied electric field dependence of charge transport. These characteristics can be well understood by considering the distribution of hopping probability from each molecule. Especially, charge-hopping probability to move out of each molecular pair is proposed to be a key factor for the degree of contribution of the molecular pair to charge transport.

In the Chapter 4, successful examples of the crystal structure refinements are presented for blue-emitting Alq₃s, γ - and δ -Alq₃, by the combined use of CP/MAS ¹³C NMR spectroscopy and recently developed [55] gauge-including projector-augmented wave (GIPAW) calculations. The structures obtained in this study are found to be more refined than those conventionally-determined by X-ray diffraction analysis. The GIPAW calculations clearly show that γ - and δ -Alq₃ have basically the same intramolecular structure, but have different intermolecular structures. This information is important for the understanding of structure–property relationship. The fluorescence wavelengths are mainly determined by isomeric states, not by intermolecular

interaction; the origin of the blue-shifted emission of γ - and δ -Alq₃ compared to emission from conventional Alq₃ is found to be the isomeric state, not intermolecular interaction. The distinction of isomeric states is a crucial issue not only for Alq₃ and for other OLED materials, such as phosphorescent iridium complexes, but also for various types of complexes. The combined method employed in this study will become a robust way to distinguish the isomeric states of complexes.

In the Chapter 5, structural analysis of γ - and δ -Alq₃ is performed by the combination of DD/MAS ²⁷Al NMR and GIPAW calculations. In sharp contrast to the isotropic chemical shifts obtained by ¹³C CP/MAS NMR experiments in the Chapter 4, NMR quadrupolar parameters obtained by DD/MAS ²⁷Al NMR are found to be insensitive to intermolecular interactions but very sensitive to intramolecular structures. From the results of Chapter 4, ¹³C CP/MAS NMR is found to be very sensitive to the intermolecular structure and insensitive to the intramolecular structure. In this meaning, ¹³C and ²⁷Al NMR are complementary to each other, which enables us to carry out precise intramolecular structure determination without considering intermolecular interactions. The findings obtained in these Chapters are important not only for fundamental science but also for design of excellent fluorescent materials.

In the Chapter 6, the structural investigation for the biological-based materials, crystals of alanine tripeptides (Ala₃), in the parallel and anti-parallel forms is performed. ¹H chemical shifts of parallel and anti-parallel β sheet structures of Ala₃ are assigned by using double-quantum magic-angle spinning (DQMAS) measurements with ultra-high field and ultra-fast MAS NMR. The assignments are compared with chemical shift calculations by GIPAW method on the geometry-optimized structures for hydrogen coordinates. The chemical shifts of amide protons are well described by the function of the distance of intermolecular NH...OC hydrogen bonding. The hydrogen bonding character of *Bombyx mori* silk fibroin with different crystalline forms is

discussed on the basis of the hydrogen bond distances.

References

- [1] A. Bernanose, *J. Chim. Phys.*, 50 (1953) 64.
- [2] W. Helfrich and W. G. Schneider, *Phys. Rev. Lett.*, 14 (1965) 229.
- [3] C. W. Tang and S. A. VanSlyke, *Appl. Phys. Lett.*, 51 (1987) 913.
- [4] C. Adachi, T. Tsutsui and S. Saito, *Appl. Phys. Lett.*, 55 (1989) 1489.
- [5] B. C. Lin, C. P. Cheng, Z. Q. You and C. P. Hsu, *J. Am. Chem. Soc.*, 127 (2005) 66.
- [6] C. Lee and K. Sohlberg, *Chem. Phys.*, 367 (2010) 7.
- [7] H. Gao, *Theor. Chem. Acc.*, 127 (2010) 759.
- [8] B. C. Lin, C. P. Cheng, Z. Q. You and C. P. Hsu, *Phys. Chem. Chem. Phys.*, 13 (2011) 20704.
- [9] T. Yamada, T. Sato, K. Tanaka and H. Kaji, *Org. Electron.*, 11 (2010) 255.
- [10] T. Yamada, F. Suzuki, A. Goto, T. Sato, K. Tanaka and H. Kaji, *Org. Electron.*, 12 (2011) 169.
- [11] H. Bässler, *Phys. Status Solidi B*, 175 (1993) 15.
- [12] H. Bässler and B. Schweitzer, *Acc. Chem. Res.*, 32 (1999) 173.
- [13] I. I. Fishchuk, A. Kadashchuk, H. Bässler and S. Nešpůrek, *Phys. Rev. B*, 67 (2003) 2243031.
- [14] S. J. Martin, A. Kambili and A. B. Walker, *Macromol. Symp.*, 212 (2004) 263.
- [15] A. Ohno and J. Hanna, *Appl. Phys. Lett.*, 82 (2003) 751.
- [16] N. Ogawa and H. Naito, *Elect. Eng. Japan*, 140 (2002) 1.
- [17] V. R. Nikitenko and M. N. Strikhanov, *J. Appl. Phys.*, 115 (2014) 073704.
- [18] S. R. Mohan, M. P. Singh, M. P. Joshi and L. M. Kukreja, *J. Phys. Chem. C*, 117 (2013) 24663.
- [19] J. J. Kwiatkowski, J. Nelson, H. Li, J. L. Bredas, W. Wenzel and C. Lennartz, *Phys. Chem.*

Chem. Phys., 10 (2008) 1852.

[20] A. Lukyanov, C. Lennartz and D. Andrienko, Phys. Status Solidi A:, 206 (2009) 2737.

[21] A. Lukyanov and D. Andrienko, Phys. Rev. B, 82 (2010) 193202.

[22] F. May, V. Marcon, M. R. Hansen, F. Grozema and D. Andrienko, J. Mater. Chem., 21 (2011) 9538.

[23] V. Rühle, A. Lukyanov, F. May, M. Schrader, T. Vehoff, J. Kirkpatrick, B. Baumeier and D. Andrienko, J. Chem. Theory Comput., 7 (2011) 3335.

[24] F. May, M. Al-Helwi, B. Baumeier, W. Kowalsky, E. Fuchs, C. Lennartz and D. Andrienko, J. Am. Chem. Soc., 134 (2012) 13818.

[25] B. Baumeier, F. May, C. Lennartz and D. Andrienko, J. Mater. Chem., 22 (2012) 10971.

[26] A. Fuchs, T. Steinbrecher, M. S. Mommer, Y. Nagata, M. Elstner and C. Lennartz, Phys. Chem. Chem. Phys., 14 (2012) 4259.

[27] C. Hosokawa, H. Higashi, H. Nakamura and T. Kusumoto, Appl. Phys. Lett., 67 (1995) 3853.

[28] J. Kido, M. Kimura and K. Nagai, Science, 267 (1995) 1332.

[29] R. Abbel, C. Grenier, M. J. Pouderoijen, J. W. Stouwdam, P. E. L. G. Leclère, R. P. Sijbesma, E. W. Meijer and A. P. H. J. Schenning, J. Am. Chem. Soc., 131 (2008) 833.

[30] A. C. Grimsdale, K. Leok Chan, R. E. Martin, P. G. Jokisz and A. B. Holmes, Chem. Rev., 109 (2009) 897.

[31] C. Yuan, S. Saito, C. Camacho, S. Irle, I. Hisaki and S. Yamaguchi, J. Am. Chem. Soc., 135 (2013) 8842.

[32] S. Reineke, M. Thomschke, B. Lüssem and K. Leo, Rev. Mod. Phys., 85 (2013) 1245.

[33] M. Braun, J. Gmeiner, M. Tzolov, M. Cölle, F. D. Meyer, W. Milius, H. Hillebrecht, O. Wendland, J. U. von Schütz and W. Brütting, J. Chem. Phys., 114 (2001) 9625.

[34] M. Cölle, R. E. Dinnebier and W. Brütting, Chem. Commun., 23 (2002) 2908.

- [35] M. Cölle, J. Gmeiner, W. Milius, H. Hillebrecht and W. Brütting, *Adv. Funct. Mater.*, 13 (2003) 108.
- [36] M. Muccini, M. A. Loi, K. Kenevey, R. Zamboni, N. Masciocchi and A. Sironi, *Adv. Mater.*, 16 (2004) 861.
- [37] M. Amati and F. Lej, *Chem. Phys. Lett.*, 358 (2002) 144.
- [38] A. Curioni, M. Boero and W. Andreoni, *Chem. Phys. Lett.*, 294 (1998) 263.
- [39] M. Amati and F. Lej, *J. Phys. Chem. A*, 107 (2003) 2560.
- [40] H. Kaji, Y. Kusaka, G. Onoyama and F. Horii, *Jpn. J. Appl. Phys.*, 44 (2005) 3706.
- [41] M. M. Levichkova, J. J. Assa, H. Fröb and K. Leo, *Appl. Phys. Lett.*, 88 (2006) 201912.
- [42] H. Kaji, Y. Kusaka, G. Onoyama and F. Horii, *J. Am. Chem. Soc.*, 128 (2006) 4292.
- [43] L. L. Li, C.-J. Fang, Q. Yuan and C. H. Yan, *Appl. Phys. Lett.*, 90 (2007) 231908.
- [44] Y. Nishiyama, T. Fukushima, K. Takami, Y. Kusaka, T. Yamazaki and H. Kaji, *Chem. Phys. Lett.*, 471 (2009) 80.
- [45] T. Tsuboi and Y. Torii, *Mol. Cryst. Liq. Cryst.*, 529 (2010) 42.
- [46] H. Bi, H. Y. Zhang, Y. Zhang, H. Z. Gao, Z. M. Su and Y. Wang, *Adv. Mater.*, 22 (2010) 1631.
- [47] M. Brinkmann, G. Gadret, M. Muccini, C. Taliani, N. Masciocchi and A. Sironi, *J. Am. Chem. Soc.*, 122 (2000) 5147.
- [48] M. Tagaya and M. Ogawa, *Phys. Chem. Chem. Phys.*, 10 (2008) 6849.
- [49] G. Baldacchini, P. Chiacchiaretta, R. Reisfeld and E. Zigansky, *J. Lumin.*, 129 (2009) 1849.
- [50] H. Bi, D. Chen, D. Li, Y. Yuan, D. Xia, Z. Zhang, H. Zhang and Y. Wang, *Chem. Commun.*, 47 (2011) 4135.
- [51] M. Cölle, J. Gmeiner, W. Milius, H. Hillebrecht and W. Brütting, *Adv. Funct. Mater.*, 13 (2003) 108.
- [52] M. Cölle and W. Brütting, *Phys. Status Solidi A*, 201 (2004) 1095.

[53] M. Rajeswaran, T. N. Blanton and K. P. Klubek, *Z. Kristallogr. New Cryst. Struct.*, 218 (2003) 439.

[54] D. F. Stickle, L. G. Presta, K. A. Dill and G. D. Rose, *J. Mol. Biol.*, 226 (1992) 1143.

[55] C. J. Pickard and F. Mauri, *Phys. Rev. B*, 63 (2001) 245101.

PART I

Clarification of the Relationship between Aggregated Structure and Charge Transport Property

Chapter 2

Multiscale Simulation of Charge Transport in a Host Material, mCP, for Organic Light-Emitting Diodes

2.1. Introduction

In the development of the organic light-emitting diodes (OLEDs), the optimization of the charge injection and charge blocking at each interface, and charge transport in each layer is required to maximize the probability of recombination of holes and electrons in the emissive layer. Among these factors, the injection and the blocking of charges have often been discussed in terms of energy levels of the highest occupied molecular orbital (HOMO) and the lowest unoccupied molecular orbital (LUMO) of organic molecules. The HOMO and the LUMO can be estimated using quantum chemical calculations for isolated molecules. However, the charge transport in organic aggregate systems is considered to depend on the structure of the molecule in an isolated state and also in an intermolecular aggregated state. Recently, some research groups [1-4] including our own [5,6] have evaluated charge transport properties by quantum chemical calculations of the rate constant, k_{CT} , for charge hopping between two molecules. This approach will provide some hints for the material design. However, calculated k_{CT} instead of the calculated mobility was compared against the experimental mobility. Moreover, crystal structures are used for the calculation of k_{CT} in most cases in spite that actual OLEDs are composed of amorphous thin layers.

We can find another approach for the understanding of charge transport properties; Bäessler et al. [7-9] evaluated the charge transport properties between the electrodes using Monte Carlo simulation. This is one of the most successful studies for charge transports in amorphous organic aggregates. However, because this approach including related ones [10-17] does not consider

the organic molecule explicitly, it is somewhat difficult to link the macroscopic charge transfer and the microscopic molecular structure directly.

We can assume that a detailed study of the charge transfer processes between electrodes is possible by the combination of these two approaches and such attempts have been made in recent years [18-24]. For example, Kwiatkowski et al. performed simulations of the charge mobility using a structure of amorphous tris(8-hydroxyquinoline) aluminum (III) (Alq_3) by approximating the Alq_3 molecule as a rigid body [18]. This is the first attempt for the charge transfer simulation considering organic molecules explicitly, as far as we know. Although the absolute value of the experimental charge mobility of Alq_3 could not be reproduced, they succeeded in explaining the difference between hole and electron mobility. Lukyanov et al. constructed an Alq_3 aggregated structure using molecular dynamics (MD) simulations without applying the rigid body approximation and investigated the influence of the force fields on the charge mobility in detail [19]. However, such investigations are still limited and more development is essential. Also, there are a number of important molecules in OLEDs other than Alq_3 , and the method should be applied to other molecular systems to the development of excellent charge transfer materials.

In this Chapter, we have performed multiscale charge transport simulations for the amorphous structure of *N,N'*-dicarbazole-3,5-benzene (mCP; shown in Figure 2.1a), which has been used as a host material for the emissive layer in blue-emitting OLEDs. We also investigated the contribution of respective molecular pairs to the charge transport in amorphous thin films. We show that molecular pairs with large electronic couplings are not most important in charge transport processes. We will show some molecular pairs effectively transport charges in the forward direction, although they do not have substantially large electronic couplings.

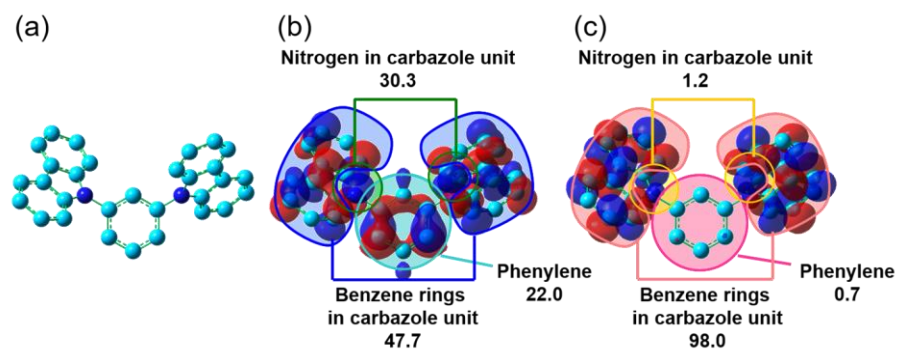
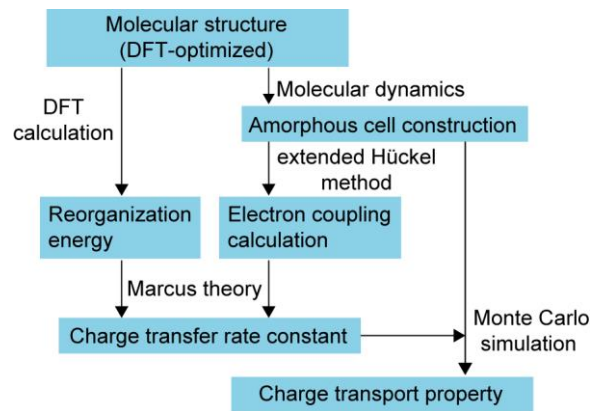


Fig. 2.1. (a) Molecular structure of mCP; (b) distribution of the HOMO of mCP; (c) distribution of the LUMO of mCP. The squared molecular orbital coefficients of benzene rings in carbazole unit, nitrogen in carbazole unit, and central phenylene unit to the molecular orbitals are also shown.

2.2. Computational section

The entire computational flow is shown in Scheme 2.1. The geometry optimization of the mCP in its neutral, cationic, and anionic states were performed using density functional theory (DFT) implemented in the Gaussian 09 program package using the B3LYP/6-31G(d) level of theory [25]. The reorganization energy for hole transport (λ^+) was obtained from the energies of the optimized structures of the neutral and cationic states. The reorganization energy for electron transport (λ^-) was calculated in a similar way. The details are provided in refs. 7 and 8. The construction of the amorphous structure was carried out by MD simulation for 100 molecules of mCP in a cubic cell (denoted as “mCP-100”). To mimic the deposition process, the initial construction of the structure was performed at a density of 0.1 g cm^{-3} and at a temperature of 598 K. Pre-optimization was then conducted. The MD simulation was performed until the density of the system becomes constant, which was over 300 ps with the constant-pressure, constant-temperature (NPT) ensembles at 298 K. A system consists of ten molecules of mCP (denoted as “mCP-10”) was also constructed in the same way. The final density of the structure was 1.0 g cm^{-3} for both the mCP-100 structure and the mCP-10 structure. The Dreiding force field was used for the MD simulation. Each parameter for the force field is corrected individually to maintain the initial value of each bond length, which is obtained by DFT calculations shown above. For the MD simulations, a cubic cell with bond lengths of 40.8 \AA was used for the mCP-100 structure, and a cubic cell with bond lengths of 19.5 \AA was used for mCP-10 structure. Information of the manipulated Dreiding force field is shown in Figure 2.2, Tables 2.1 and 2.2. The force field parameters were modified to keep the bond lengths constant during the MD calculations, which are optimized at the DFT level (B3LYP/6-31G(d)).



Scheme 2.1. Flow of the charge transport simulations for the amorphous mCP layer.

The manipulated parameters were as follows:

Bond stretch

$$E = \frac{K_0}{2}(R - R_0)^2$$

$K_0 : kcal\ mol^{-1}\text{\AA}^{-2}$
 $R_0 : \text{\AA}$

Angle bend

$$E = \frac{K_0}{2}(\theta - \theta_0)^2$$

$K_0 : kcal\ mol^{-1}rad^{-2}$

Torsion

$$E = \frac{1}{2} \sum_j \{B_j(1 - d_j \cos[n_j \phi])\}$$

$B : kcal\ mol^{-1}$

Inversion

$$E = K_0(1 - \cos \omega_0)$$

$K_0 : kcal\ mol^{-1}$

Van der Waals

$$E = D_0 \left[\left(\frac{R_0}{R}\right)^{12} - 2 \left(\frac{R_0}{R}\right)^6 \right]$$

$D_0 : kcal\ mol^{-1}$

Coulombic

$$E = C \frac{q_i q_j R_0}{\varepsilon R^2}$$

Hydrogen bond

$$E = D_0 \left[5 \left(\frac{R_0}{R}\right)^{12} - 6 \left(\frac{R_0}{R}\right)^{10} \right] \cos^4 \phi$$

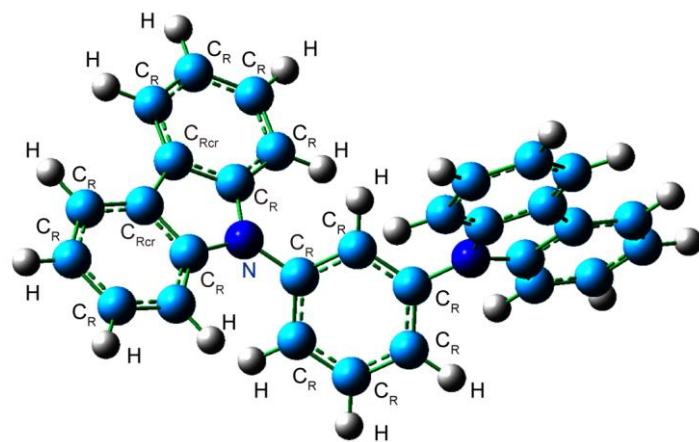


Fig. 2.2. Structure and atom types of the mCP molecule.

Table 2.1. Manipulated force field parameters for the mCP molecule. The asterisks

indicate the atoms of any type.

Parameters		R_0 (Å)	θ_0 (degree)	B (kcal mol ⁻¹)	d (-)	n (-)	ω_0 (rad)	K_0 (kcal mol ⁻¹)
Bond stretch	C _R -C _R	1.399						10500
	N-C _R	1.407						10500
	C _R -H	1.086						7000
	C _{Rcr} -C _{Rcr}	1.448						10500
	C _{Rcr} -C _R	1.399						10500
Angle bend	*-C _R -*		120					100
	-C _{Rcr} -		120					100
Torsion	*-C _R -C _R -*			25	1	2		
	-C _{Rcr} -C _{Rcr} -			25	1	2		
	-C _{Rcr} -C _R -			25	1	2		
Inversion	C _R -*-*-*						0	40
	C _{Rcr} -*-*-*						0	40

Table 2.2. Force field parameters for the mCP molecule (non-bonded).

Parameters	R_0 (Å)	D_0 (kcal mol ⁻¹)	C (Å kcal mol ⁻¹ e ⁻²)
Coulombic	1		332
Hydrogen bond	2.75	4	

The amorphous structures thus obtained are shown in Figure 2.3. The calculation of the electronic coupling for hole and electron transfer (H_{AB}^+ and H_{AB}^- , respectively) was performed for the molecular pairs that have an adjacent center-to-center distance within 20 Å in the amorphous structure. The total number of pairs, approximately 270,000, was reduced to about 5,000 pairs at the 20 Å cut-off. As shown in Figure 2.4, the values of H_{AB} of the molecular pairs, whose adjacent center-to-center distance is more than 20 Å, is negligibly small, less than 1×10^{-10} meV. We verified that these molecular pairs with small H_{AB} do not take part in the charge transport.

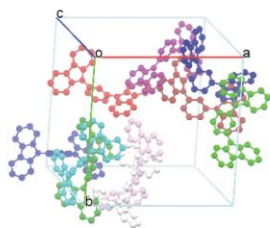
Using the values of H_{AB}^+ (H_{AB}^-) and λ^+ (λ^-) obtained above, the rate constants for hole and electron transfer (k_{CT}^+ and k_{CT}^- , respectively) under the applied external electric field was calculated according Eq. (2.1) [7,26],

$$k_{CT} = \frac{4\pi^2}{h} H_{AB}^2 \frac{1}{\sqrt{4\pi\lambda k_B T}} \exp\left[-\left(\frac{\lambda + \Delta G}{4\lambda k_B T}\right)^2\right], \quad (2.1)$$

where ΔG is the free energy difference between the initial and final states, T is the temperature, h is Plank's constant and k_B is Boltzmann's constant. Under the applied external electric field, the free energy change, ΔG , is given by Eq. (2.2),

$$\Delta G = qF\Delta x, \quad (2.2)$$

(a) mCP-10



(b) mCP-100

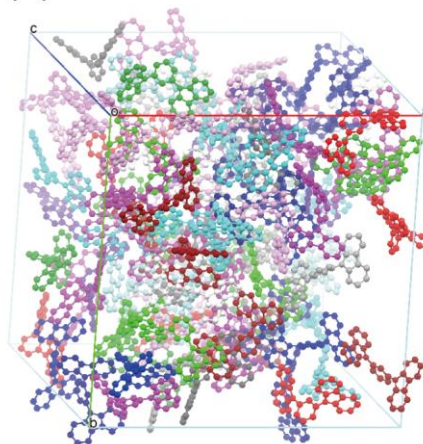


Fig. 2.3. Amorphous structures for (a) mCP-10 and (b) mCP-100. Each of the molecules is color-coded for clarity.

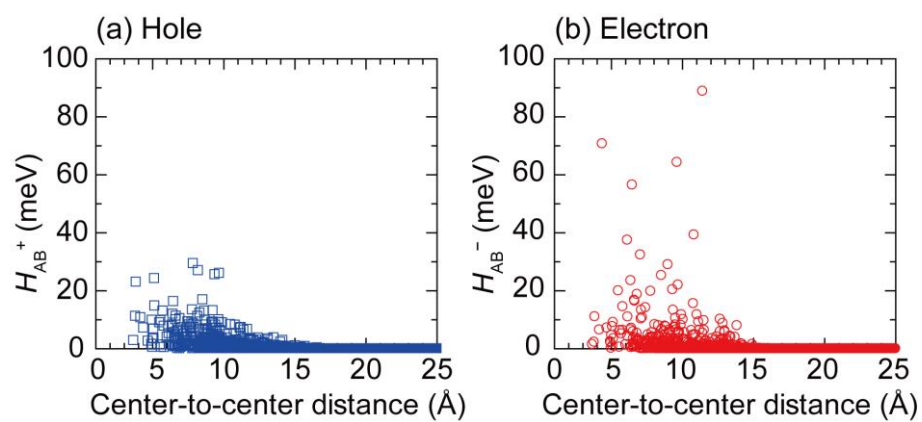


Fig. 2.4. Dependence of the electronic coupling (H_{AB}^+ and H_{AB}^-) on the center-to-center distance for (a) holes and for (b) electrons.

where q is the elementary charge (unit charge), F is the applied external electric field strength and Δx is the distance between the neighboring relevant molecules along the electric field. The calculations of k_{CT} were performed for the pairs of molecules with an adjacent center-to-center distance within 20 Å as described above.

The charge hopping was performed using a Monte Carlo simulation based on the hopping probability corresponding to the calculated value of k_{CT} . The hoppings of 1,000 charges were simulated and the charge mobilities for holes and electrons (μ_{CT}^+ and μ_{CT}^- , respectively) were calculated. Periodic boundary conditions were set in all directions. The thickness of the film was 100 nm and the electric field was applied in this direction. The square root of the external electric field was 300–1,000 V^{1/2} cm^{-1/2}, which corresponded to a voltage of 0.9–10 V. The temperature was set to 298 K. The amorphous structures constructed in this Chapter should be isotropic; therefore, the a-, b- and c-axis should be statistically equivalent. To verify this, charge transport simulations were performed by applying the electric field along the a-, b- or c-axis of the cubic cell individually. As described in below, anisotropy was observed in the charge mobility for the mCP-10 structure, so the statistical average in mCP-10 was not sufficient. The charge mobility along each axis was isotropic for the mCP-100 structure, so the results of the calculations using the mCP-100 structure along a-axis are mainly described in this Chapter. Amorphous cell and Forcite programs (Dassault Systèmes Biovia Corp., San Diego, CA, USA) were used for the construction of the amorphous structure. Calculations of H_{AB} was performed by the Gaussian 09 program package using the extended Hückel theory and in-house program written in C. Charge transport Monte Carlo simulations was performed using the in-house C program.

2.3. Results and discussion

2.3.1. Reorganization energies and electronic couplings

The calculated λ^+ and λ^- were 0.077 eV and 0.14 eV, respectively. Figure 2.1b and 2.1c shows distribution of the HOMO and the LUMO of mCP, respectively. The squared molecular orbital coefficients of respective fragments of mCP are also shown. While the HOMO is delocalized over the entire molecule including the central phenylene moiety, the LUMO is strongly localized on the outer benzene rings in carbazole moieties. Figure 2.5 shows the calculated H_{AB} between the neighboring molecules in the mCP-100 structure. The values of H_{AB}^- (Figure 2.5b) have a larger distribution compared with those of H_{AB}^+ (Figure 2.5a). This implies that the overlap of the LUMOs among neighboring mCP molecules is significantly increased when there is close contact of the carbazole moieties. As shown in Figure 2.6a and 2.6b, the pair of molecules with the maximum value of H_{AB}^- ($H_{AB}^-_{\max}$) has closer contact of the carbazole moieties than that with maximum value of H_{AB}^+ ($H_{AB}^+_{\max}$).

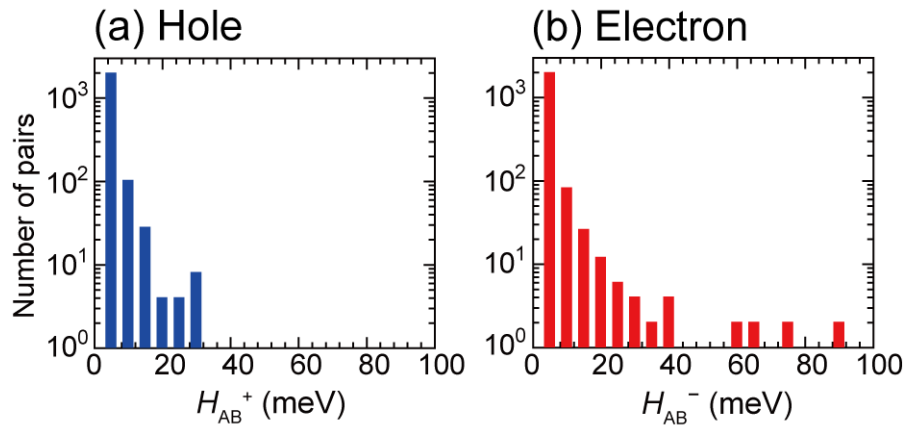


Fig. 2.5. Histograms of the number of pairs with the electronic coupling for (a) holes (H_{AB}^+) and (b) electrons (H_{AB}^-) in the mCP-100 structure.

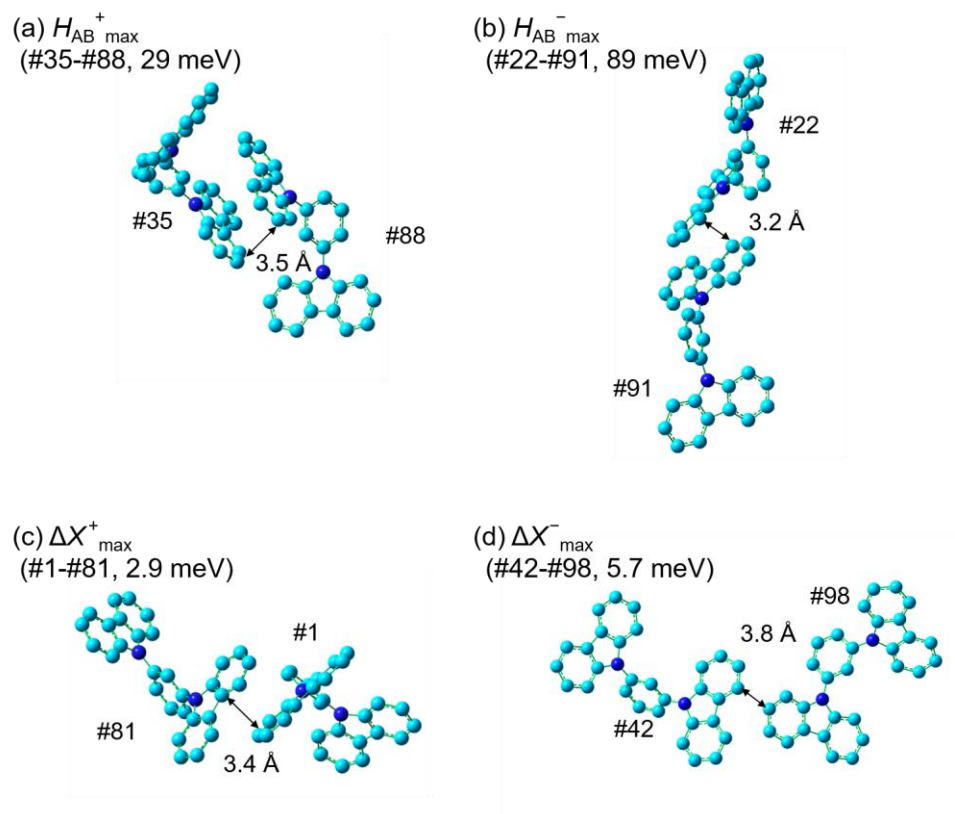


Fig. 2.6. Pairs of molecules with the maximum values of H_{AB} for (a) hole ($H_{AB}^+_{\max}$) and (b) electron ($H_{AB}^-_{\max}$), and pairs of molecules with the largest values of migration distance for (c) hole (ΔX^+_{\max}) and (d) electron (ΔX^-_{\max}).

2.3.2. Charge transport simulations

Figure 2.7 shows the electric field dependence of the hole and electron mobilities along the a-, b- and c-axes of the amorphous mCP-10 and mCP-100 structure by Monte Carlo simulations. The ratio of the charge mobility for hole/electron transfer, μ^+/μ^- , varied between 2.7 and 4.2 within the range of 300–1,000 $\text{V}^{1/2} \text{cm}^{-1/2}$ for the mCP-100 structure (Figure 2.7b). This suggests that the mCP-100 structure has better hole transport than electron transport. Although the absolute mobilities are 1–2 orders of magnitude higher than the experimental values [27-29], the ratio of μ^+/μ^- is almost the same as that experimentally obtained. Also, compared with the results for the mCP-10 structure (Figure 2.7a), the difference in the charge mobility for the mCP-100 structure along each axis is significantly small. The mCP-100 structure can sufficiently reproduce the isotropic nature of an amorphous system.

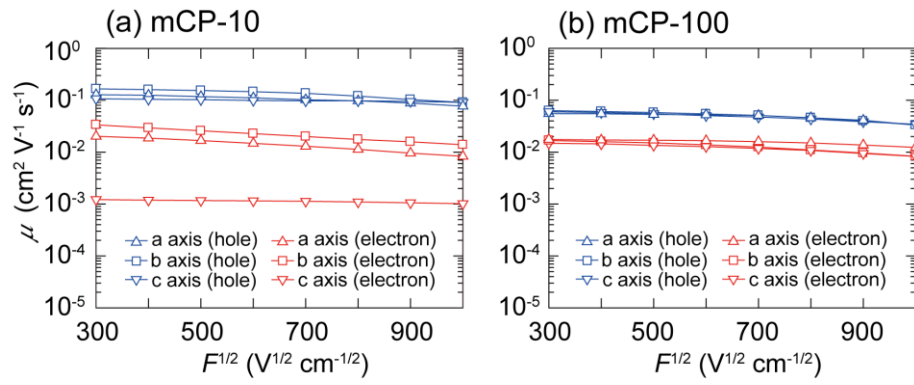


Fig. 2.7. Simulated field dependence of the charge mobilities for (a) the mCP-10 structure and (b) the mCP-100 structure. The thickness was set to 100 nm.

Figure 2.8 shows the charge transport trajectories for the one-hole and the one-electron simulations using the mCP-100 structure. At $300 \text{ V}^{1/2} \text{ cm}^{-1/2}$, the hole (Figure 2.8a) reached the counter electrode guided by the applied electric field as well as by using more complicated routes, indicating a strong diffusive behavior. This included the direction opposite to the applied electric field and/or components in perpendicular directions. At $1,000 \text{ V}^{1/2} \text{ cm}^{-1/2}$, the hopping of the hole in the direction of the applied field was more efficient (Figure 2.8b). The trajectories for electron transport had a similar trend depending on the applied electric field (Figure 2.8c and 2.8d). These results clearly indicate that there is increased contribution of the drift transport as the applied electric field strength was increased.

As shown in Figure 2.5, H_{AB}^- is greater than H_{AB}^+ . For the two molecular pairs which have H_{AB}^- and H_{AB}^+ , k_{CT}^- and k_{CT}^+ were calculated using Eq. (2.1). They are denoted as k_{CT}^- and k_{CT}^+ , respectively. For $300\text{--}1,000 \text{ V}^{1/2} \text{ cm}^{-1/2}$, the k_{CT}^- and k_{CT}^+ were obtained to be $9.1 \times 10^{13}\text{--}3.2 \times 10^{14} \text{ s}^{-1}$ and $2.6 \times 10^{13}\text{--}5.1 \times 10^{13} \text{ s}^{-1}$, respectively. From the results, we imagine mCP has superior electron transport property rather than hole transport. However, Monte Carlo simulations tell us that μ^+ is larger than μ^- as shown in Figure 2.7. To clarify the details, we analyzed the relationship of H_{AB} and the charge transport between the electrodes. Figure 2.9 shows the relationship of H_{AB} and the total number of hops, N_{all} . Here, N_{all} is the number of times that hopping occurred between the two molecules during the simulation (the sum of the hops in the forward direction (N_{fwd}) and in the backward direction (N_{bwd}); $N_{\text{all}} = N_{\text{fwd}} + N_{\text{bwd}}$). The values of N_{all} , N_{fwd} and N_{bwd} are the averages of the 1000 times of the Monte Carlo simulations. At $300 \text{ V}^{1/2} \text{ cm}^{-1/2}$, N_{all} for both of holes and electrons monotonously increased with H_{AB}^+ and H_{AB}^- . However, at $1,000 \text{ V}^{1/2} \text{ cm}^{-1/2}$, a deviation from the trend was observed. In Figure 2.10a and 2.10b, N_{fwd} , N_{bwd} , and their difference (N_{diff} ; $N_{\text{diff}} = N_{\text{fwd}} - N_{\text{bwd}}$) are shown for the top 40 pairs of large N_{all} at $300 \text{ V}^{1/2} \text{ cm}^{-1/2}$. The corresponding data for 1,000

$V^{1/2} \text{ cm}^{-1/2}$ is shown in Figure 2.10c and 2.10d. A clear relationship was not seen between N_{fwd} and N_{diff} . This suggests that hopping transport may not always proceed efficiently in the forward direction even if N_{fwd} is high.

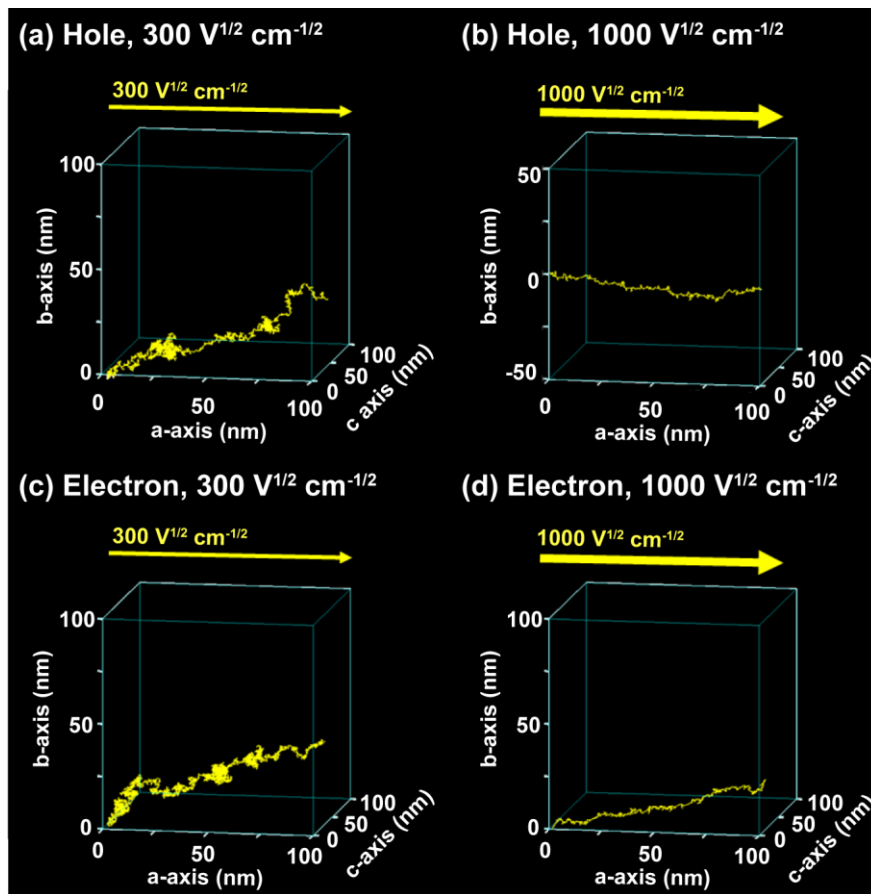


Fig. 2.8. Charge transfer trajectory under the electric fields applied in the direction of the a-axis: (a) hole at $300 \text{ V}^{1/2} \text{ cm}^{-1/2}$; (b) hole at $1000 \text{ V}^{1/2} \text{ cm}^{-1/2}$; (c) electron at $300 \text{ V}^{1/2} \text{ cm}^{-1/2}$; (d) electron at $1000 \text{ V}^{1/2} \text{ cm}^{-1/2}$. The simulations were started from the origin of the cell with one hole or one electron, respectively.

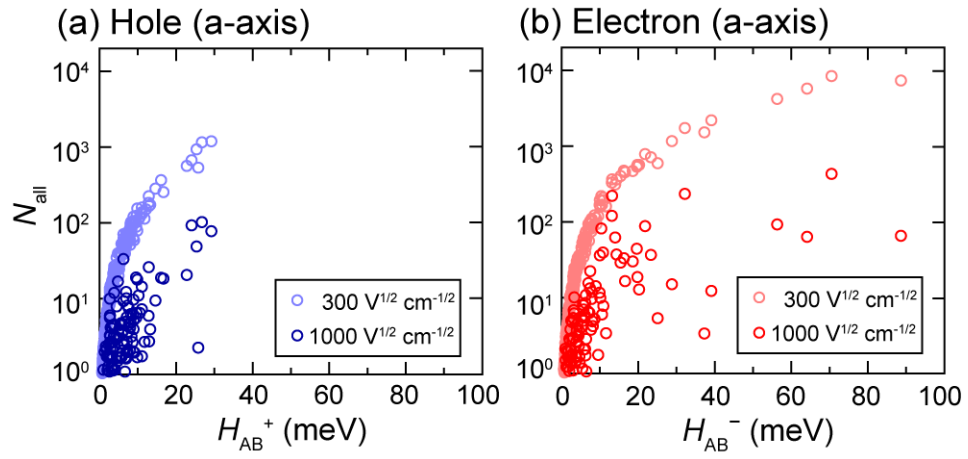


Fig. 2.9. Correlation of the total number of hops (N_{all}) and the electronic coupling ((a) for holes, H_{AB}^+ , and (b) for electrons, H_{AB}^-) under the different electric fields in the direction of the a-axis.

“Round-trips”, that is, carriers hop forward but return back to the original molecule, occur. As shown in Figure 2.10, even though the number of hops in the forward direction, N_{fwd} , was greater than 10^2 , there was approximately the same number of hops in the backward direction, N_{bwd} . The actual number of hops in the forward direction (N_{diff}) was at most approximately 5.

Here, we define ΔX by the product of N_{diff} and Δx ,

$$\Delta X = N_{\text{diff}}\Delta x. \quad (2.3)$$

ΔX is the contribution of each pair for the migration distance of a charge (average migration distance of 1,000 charges) in the direction of the applied electric field. Although, no relationships were observed between H_{AB} and ΔX (Figure 2.11), and between N_{fwd} and ΔX (Figure 2.12), we found a correlation between N_{diff} and ΔX (Figure 2.13). These results show that the charge transport is not uniquely determined by the value of H_{AB} in the case of amorphous systems. This is different from the crystal systems [5,6].

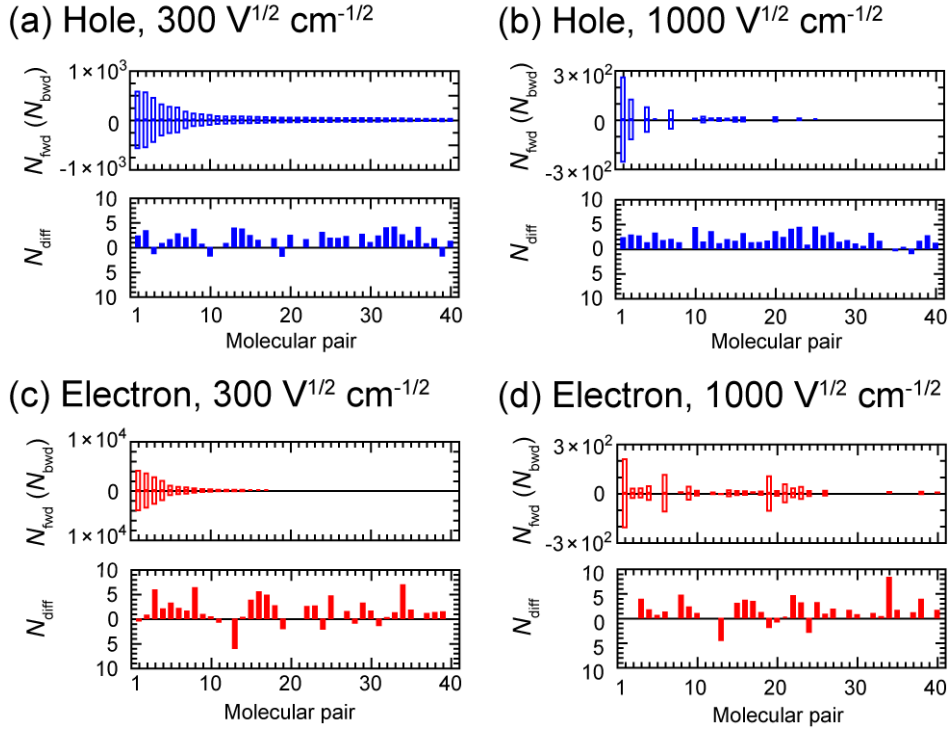


Fig. 2.10. Number of hops in the forward direction (N_{fwd}), backward direction (N_{bwd}), and difference between the forward direction and the backward direction (N_{diff}): (a) hole at $300 \text{ V}^{1/2} \text{ cm}^{-1/2}$; (b) hole at $1000 \text{ V}^{1/2} \text{ cm}^{-1/2}$, (c) electron at $300 \text{ V}^{1/2} \text{ cm}^{-1/2}$; (d) electron at $1000 \text{ V}^{1/2} \text{ cm}^{-1/2}$. The molecular pairs are numbered in order of decreasing N_{all} at $300 \text{ V}^{1/2} \text{ cm}^{-1/2}$. The top 40 molecular pairs with high N_{all} are shown in the figure. The charge transport simulations were performed using either holes or electrons with the electric field in the direction of the a-axis. The values of N_{fwd} and N_{bwd} are the averages of the 1000 times of the Monte Carlo simulations. Note that N_{fwd} and N_{bwd} are shown in positive and negative values, respectively.

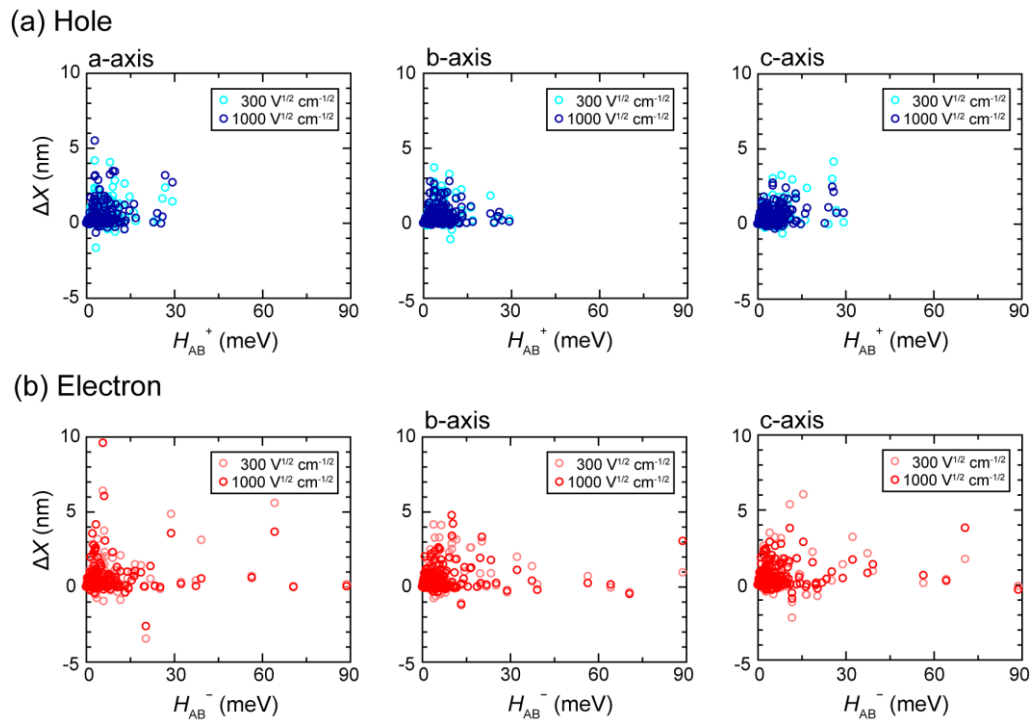


Fig. 2.11. Correlation of H_{AB} and ΔX .

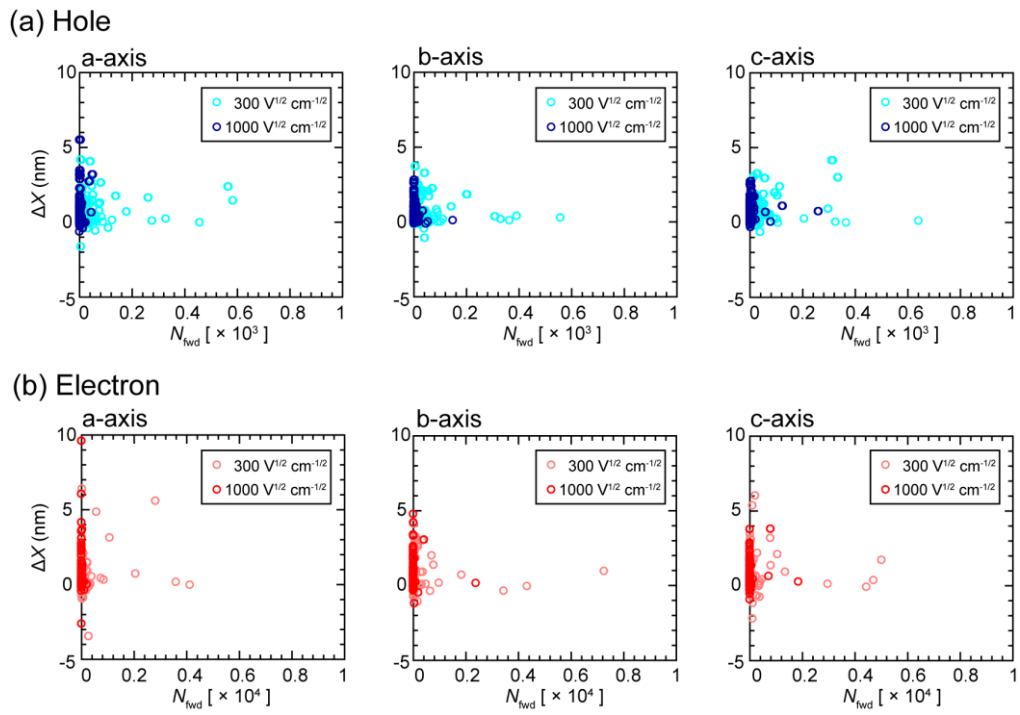
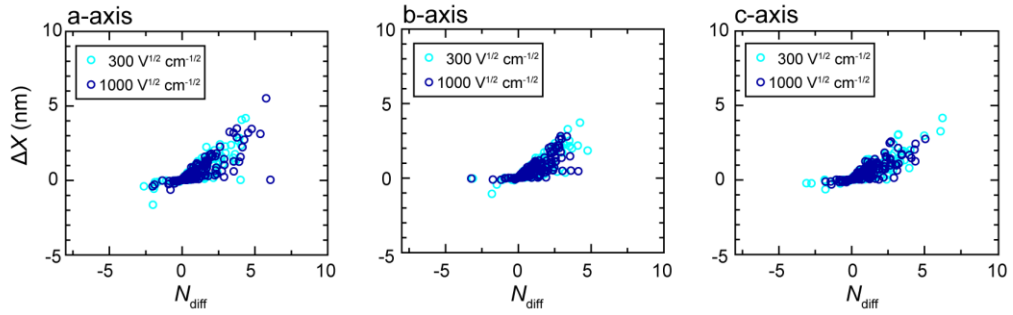


Fig. 2.12. Correlation of N_{fwd} and ΔX .

(a) Hole



(b) Electron

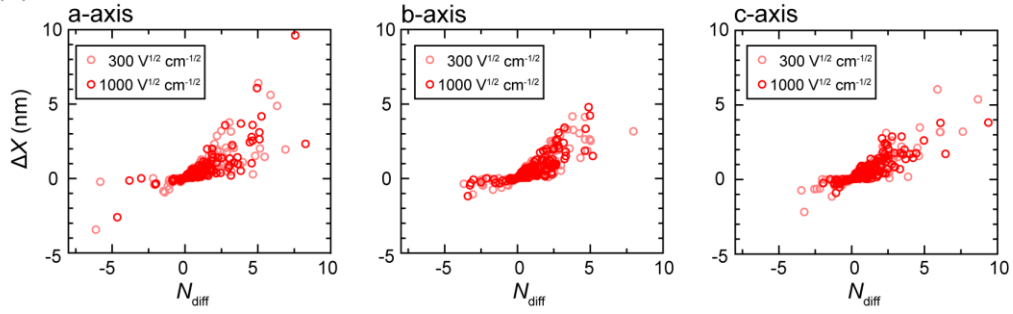


Fig. 2.13. Correlation of N_{diff} and ΔX .

Figure 2.14 shows the pairs with $H_{AB\text{ max}}$ and the pairs with the largest migration distance in the amorphous structure, ΔX_{max} , respectively (see also Figure 2.6). While ΔX_{max} is 4.2 nm for hole transport (the H_{AB}^+ is 2.9 meV), ΔX of the pair with $H_{AB}^+_{\text{max}}$ (29 meV) is only 1.4 nm. For electron transport, ΔX_{max} is 6.4 nm (the H_{AB}^- 5.7 meV), whereas ΔX is only 0.16 nm for the molecular pair with $H_{AB}^-_{\text{max}}$ (89 meV). Table 2.3 summarizes N_{fwd} , N_{bwd} , N_{all} and N_{diff} for the respective molecular pairs shown in Figure 2.14. The ratio of the total number of hops, $N_{\text{all}} / N_{\text{diff}}$, and ΔX are also shown. For the molecular pairs with $H_{AB}^+_{\text{max}}$, the charges hopped in the direction of the applied electric field once in every 515 times of hops at $300 \text{ V}^{1/2} \text{ cm}^{-1/2}$, and it became approximately once in every 18 times of hops at $1,000 \text{ V}^{1/2} \text{ cm}^{-1/2}$. It is clear that while the diffusion transport is dominant at low applied electric fields, the contribution of the drift transport increased as the applied electric field increased. For the molecular pairs with ΔX^+_{max} , the charges hop in the direction of the applied field once in every 3 times of hops at $300 \text{ V}^{1/2} \text{ cm}^{-1/2}$. The charges hopped almost every time in the direction of the applied electric field when the field was increased to $1000 \text{ V}^{1/2} \text{ cm}^{-1/2}$. The hops for the molecular pairs with ΔX^-_{max} and $H_{AB}^-_{\text{max}}$ showed similar trends to those with ΔX^+_{max} and $H_{AB}^+_{\text{max}}$. Charge-hopping for the molecular pairs with $H_{AB}^+_{\text{max}}$ and $H_{AB}^-_{\text{max}}$ occurred mainly through diffusion and so charges tend to take “round-trips” between the two molecules, especially at low electric fields. For molecular pairs with ΔX^+_{max} and ΔX^-_{max} , the contribution of the drift transport increased. For the pairs with large ΔX , the free energy difference between the initial and final states, ΔG , is large as found from Eq. (2.2) and (2.3). The large ΔG is the origin of the effective forward hopping.

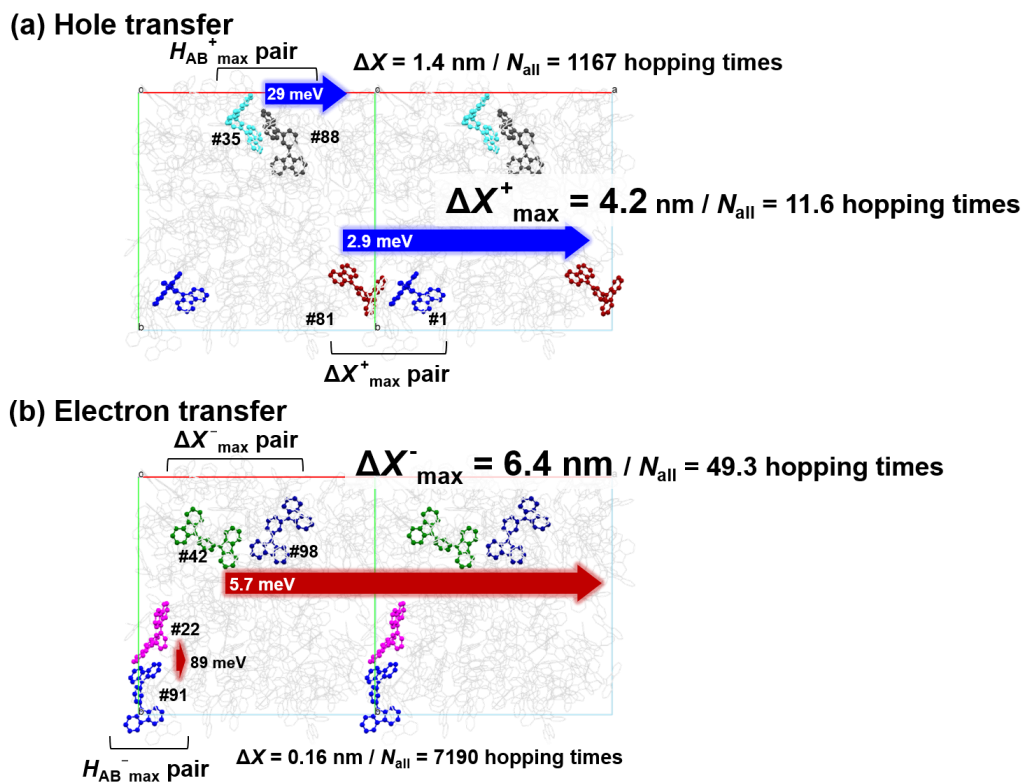


Fig. 2.14. The values of H_{AB}^+ and ΔX^+ (H_{AB}^- and ΔX^-) for the molecular pairs with $H_{AB}^+_{\text{max}}$ and ΔX^+_{max} as well as $H_{AB}^-_{\text{max}}$ and ΔX^-_{max} : (a) for hole transfers and (b) electron transfers along the a-axis at a $300 \text{ V}^{1/2} \text{ cm}^{-1/2}$. The length of the arrow is proportional to the actual migration distance, ΔX .

Table 2.3. Number of hops in the forward direction (N_{fwd}), backward direction (N_{bwd}), the sum (N_{all}) and the difference (N_{diff}) for the respective molecular pairs that are shown in Fig. 2.14. The ratio of $N_{\text{all}} / N_{\text{diff}}$ and the average migrated distance (ΔX) are also shown.

	Molecule pairs	H_{AB} (meV)	$F^{1/2}$ ($\text{V}^{1/2}$ $\text{cm}^{-1/2}$)	Number of hops				$N_{\text{all}} / N_{\text{diff}}$	ΔX (nm)
				N_{fwd}	N_{bwd}	N_{all}	N_{diff}		
Hole	$H_{\text{AB}}^+_{\text{max}}$	29	300	584.7	582.4	1167.1	2.3	515	1.4
			1000	40.2	35.9	76.1	4.3	18	2.7
	ΔX^+_{max}	2.9	300	8.0	3.6	11.6	4.4	3	4.2
			1000	5.8	0.0	5.8	5.8	1	5.5
Electron	$H_{\text{AB}}^-_{\text{max}}$	89	300	3595.3	3594.5	7189.8	0.8	9289	0.16
			1000	32.2	32.1	64.3	0.1	495	0.026
	ΔX^-_{max}	5.7	300	27.2	22.1	49.3	5.1	10	6.4
			1000	7.8	0.2	8.0	7.6	1	9.6

Figure 2.15 shows the results of the charge transport simulations (the electric field is applied along the a-axis). The hole and electron mobilities along the a-axis in Fig. 2.7 are replotted in Fig. 2.15 as filled squares. Compared to these, both hole and electron mobilities were reduced when the molecular pairs with ΔX^+_{\max} and ΔX^-_{\max} were not used for charge transport simulations (filled circles). In particular, the electron mobility reduced significantly. It is obvious that the molecular pairs with ΔX^+_{\max} and ΔX^-_{\max} form a critical hopping path for charge transports and improve charge mobilities. In sharp contrast, both hole and electron mobilities were unchanged, regardless of whether the molecular pair with $H_{AB}^+_{\max}$ and $H_{AB}^-_{\max}$ were used (filled squares) or not (open circles). These results show that the molecular pairs with $H_{AB}^+_{\max}$ and $H_{AB}^-_{\max}$ are not critical for charge transports between electrodes.

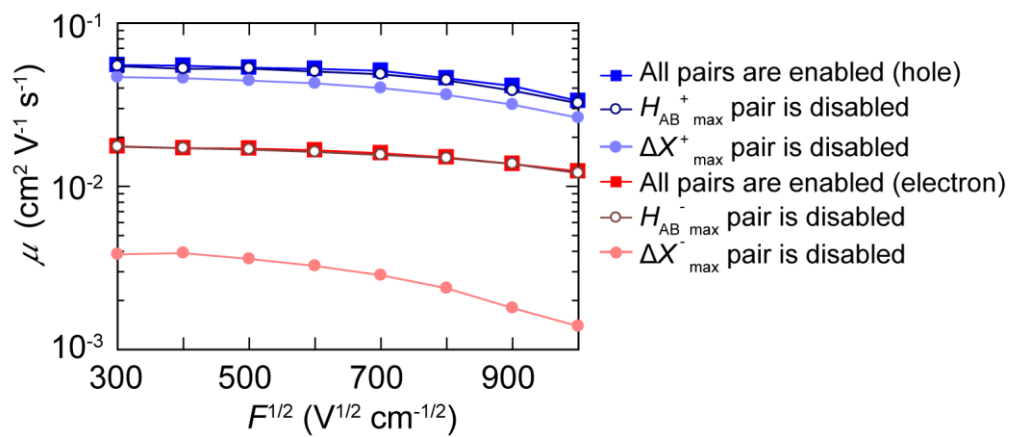


Fig. 2.15. Simulation of the charge mobility with the molecular pairs with $H_{AB\ max}$ or $\Delta X_{\ max}$ either enabled or disabled. The thickness of the charge transport layer was set to 100 nm.

2.4. Conclusion

In this Chapter, we performed the charge transport simulations in an amorphous mCP thin layer. Organic molecules were explicitly considered to link the macroscopic charge transfer and the microscopic molecular structure directly. The hole mobility of mCP was calculated to be three to four times larger than the electron mobility. This result was in good agreement with the experimentally determined ratio of the charge mobility for hole and electron transfer. It was clearly shown that while the diffusion transport is dominant at low applied electric fields, the contribution of the drift transport increased as the applied electric field increased. At a low electric field strength, both holes and electrons reached the counter electrode not through simple routes directly toward the direction of the applied electric field but through complicated routes, including the direction opposite to and perpendicular to the electric field. At a high electric field strength, charge hopping in the direction of the applied electric field can be advantageous and becomes significantly efficient. Charge hopping for molecular pairs with large H_{AB} was mainly diffusive and so back and forth between the two molecules tended to occur more frequently. Therefore, these molecular pairs are not crucial for charge transports. In contrast, the contribution of the drift transport was dominant for molecular pairs with large ΔX . The molecular pair substantially improve charge mobilities by forming effective charge transfer path. Further development of this approach is in progress for multi-layered amorphous systems composed of hole transport, emission, and electron transport layers, and for more complex systems, including charge blocking layers, etc.

(Chapter 2 is the unedited Author's version of a Submitted Work that was subsequently accepted for publication in *J. Mater. Chem. C* copyright © Royal Chemical Society after peer review. To access the final edited and published work see the following website: <http://pubs.rsc.org/-/content/articlelanding/2015/tc/c5tc00543d>)

REFERENCES

- [1] B. C. Lin, C. P. Cheng, Z. Q. You and C. P. Hsu, *J. Am. Chem. Soc.*, 127 (2005) 66.
- [2] C. Lee and K. Sohlberg, *Chem. Phys.*, 367 (2010) 7.
- [3] H. Gao, *Theor. Chem. Acc.*, 127 (2010) 759.
- [4] B. C. Lin, C. P. Cheng, Z. Q. You and C. P. Hsu, *Phys. Chem. Chem. Phys.*, 13 (2011) 20704.
- [5] T. Yamada, T. Sato, K. Tanaka and H. Kaji, *Org. Electron.*, 11 (2010) 255.
- [6] T. Yamada, F. Suzuki, A. Goto, T. Sato, K. Tanaka and H. Kaji, *Org. Electron.*, 12 (2011) 169.
- [7] H. Bässler, *Phys. Status Solidi B*, 175 (1993) 15.
- [8] H. Bässler and B. Schweitzer, *Acc. Chem. Res.*, 32 (1999) 173.
- [9] I. I. Fishchuk, A. Kadashchuk, H. Bässler and S. Nešpůrek, *Phys. Rev. B*, 67 (2003) 2243031.
- [10] D. H. Dunlap, P. E. Parris and V. M. Kenkre, *Phys. Rev. Lett.*, 77 (1996) 542.
- [11] A. Hirao and H. Nishizawa, *Phys. Rev. B*, 54 (1996) 4755.
- [12] A. Hirao and H. Nishizawa, *Phys. Rev. B*, 56 (1997) R2904.
- [13] S. V. Novikov, D. H. Dunlap, V. M. Kenkre, P. E. Parris and A. V. Vannikov, *Phys. Rev. Lett.*, 81 (1998) 4472.
- [14] A. Ohno and J. Hanna, *Appl. Phys. Lett.*, 82 (2003) 751.
- [15] S. Yin and Y. Lv, *Org. Electron.*, 9 (2008) 852.
- [16] S. R. Mohan, M. P. Singh, M. P. Joshi and L. M. Kukreja, *J. Phys. Chem. C*, 117 (2013) 24663.

- [17] V. R. Nikitenko and M. N. Strikhanov, *J. Appl. Phys.*, 115 (2014) 073704.
- [18] J. J. Kwiatkowski, J. Nelson, H. Li, J. L. Bredas, W. Wenzel and C. Lennartz, *Phys. Chem. Chem. Phys.*, 10 (2008) 1852.
- [19] A. Lukyanov, C. Lennartz and D. Andrienko, *Phys. Status Solidi A*, 206 (2009) 2737.
- [20] J. Nelson, J. J. Kwiatkowski, J. Kirkpatrick and J. M. Frost, *Acc. Chem. Res.*, 42 (2009) 1768.
- [21] V. Rühle, A. Lukyanov, F. May, M. Schrader, T. Vehoff, J. Kirkpatrick, B. Baumeier and D. Andrienko, *J. Chem. Theory Comput.*, 7 (2011) 3335.
- [22] F. May, M. Al-Helwi, B. Baumeier, W. Kowalsky, E. Fuchs, C. Lennartz and D. Andrienko, *J. Am. Chem. Soc.*, 134 (2012) 13818.
- [23] B. Baumeier, F. May, C. Lennartz and D. Andrienko, *J. Mater. Chem.*, 22 (2012) 10971.
- [24] A. Fuchs, T. Steinbrecher, M. S. Mommer, Y. Nagata, M. Elstner and C. Lennartz, *Phys. Chem. Chem. Phys.*, 14 (2012) 4259.
- [25] M.J. Frisch et al., *Gaussian 09*, Gaussian, Inc., Wallingford CT, 2009.
- [26] R. A. Marcus and N. Sutin, *Biochim. Biophys. Acta*, 811 (1985) 265.
- [27] M. F. Wu, S. J. Yeh, C. T. Chen, H. Murayama, T. Tsuboi, W. S. Li, I. Chao, S. W. Liu and J. K. Wang, *Adv. Funct. Mater.*, 17 (2007) 1887.
- [28] C. H. Hsiao, S. W. Liu, C. T. Chen and J. H. Lee, *Org. Electron.*, 11 (2010) 1500.
- [29] T. Tsuboi, *J. Non-Cryst. Solids*, 356 (2010) 1919.

Chapter 3

Effect of Structural and Energetic Disorders on Charge Hopping in Amorphous Organic Thin Layer Studied by Multiscale Charge Transport Simulation

3.1. Introduction

Understanding the charge transport properties of organic thin films is of great interest not only for fundamental science but also for practical applications to organic electronics such as organic light-emitting diodes (OLEDs), organic solar cells, and organic thin-film transistors [1]. For these devices, materials having high charge mobility have attracted much attention because they can crucially contribute to their device performances. Charge transport in the organic amorphous layer is considered to occur by intermolecular charge hopping. Many models [2-4] have been proposed to understand the charge transport in the organic amorphous aggregates; the Gaussian disorder model [4] succeeded in describing the macroscopic charge transport process in amorphous organic solids. However, the model lacks microscopic (molecular level) description of charge transport processes. In contrast, charge transport simulations based on Marcus theory [5] have been carried out for amorphous aggregates [6-15], including our own [16, 17], to reproduce experimental charge mobilities. However, microscopic behavior of charge transport in organic amorphous aggregates is not entirely understood. There is distributions of energy levels of frontier orbitals in amorphous aggregates. This effect is usually called diagonal (energetic) disorder. Energetic disorder originates from the dipole-dipole or ion-dipole interaction and is caused by the disorder of surrounding molecules.

Organic amorphous layers in the device essentially have structural distribution by nature, such as intermolecular distance and relative orientation among adjacent molecule. This structural

distribution in the organic aggregate is usually called off-diagonal (structural) disorder. However, few studies have focused on the effect of structural disorder on charge-hopping phenomena in molecular level. Here, we design this study to investigate the contribution of respective molecular pairs to the charge hopping in structures having different degrees of structural disorder. In this Chapter we perform charge transport simulations with a comparison of a crystal [19] and an amorphous structure of *N,N'*-diphenyl-*N,N'*-bis(1-naphthyl)-1,1'-biphenyl-4,4'-diamine (NPD, Figure 3.1), which is widely used as a hole transport material in OLEDs. The crystal and the amorphous phases are used as ordered and disordered structures having small (negligible) and large structural disorders, respectively. It is meaningful to make a comparison between the crystal and the amorphous phases to clarify the effect of structural disorder on the charge hopping. We investigate the effect of structural disorder, as well as the energetic disorder on charge hopping phenomena at the level of respective molecular pairs based on the quantum chemical and kinetic Monte Carlo framework by explicitly taking into account the molecular configurations.

Another purpose of this Chapter is to clarify the origin of bipolar charge transport in NPD. Although NPD has been used and considered as a hole transport material [20-28], it has been found to exhibit unexpected high electron mobility [29-33] in addition to its hole transporting ability. In this Chapter, we investigate the molecular-level origin of electron transport in NPD being the amorphous phase using a computational model reproducing the experimental charge mobility quantitatively.

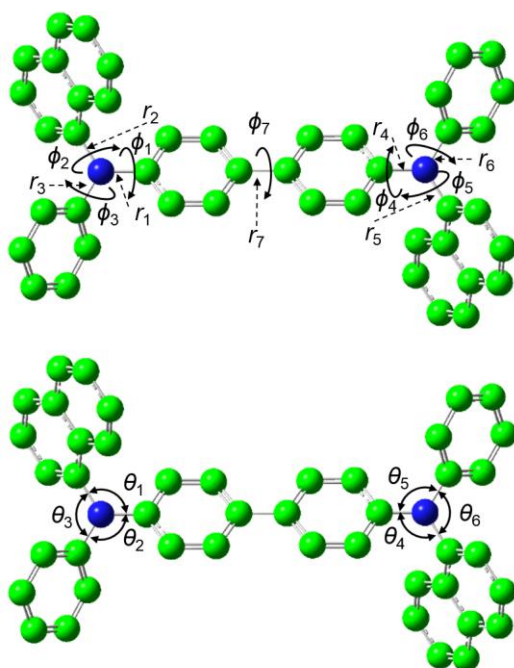


Fig. 3.1. Chemical structure of NPD. ϕ_i , θ_i , and r_i represent torsion angles, bond angles, and bond lengths, respectively. Green: carbon atoms, blue: nitrogen atoms. Proton atoms are omitted for clarity.

3.2. Computational section

For the crystal phase, the X-ray diffraction determined structure reported by Cheng et al. [19] was used without further structure optimization (denoted as “cry-NPD”). As shown in Figure 3.2a, it has two crystallographically independent molecules, labeled as I and II. The density of the structure was 1.22 g cm^{-3} . The construction of the amorphous structure was carried out by molecular dynamics (MD) simulation for 4000 molecules of NPD in a cubic cell (denoted as “amo-NPD”). The MD simulation was performed using LAMMPS program [34]. For the MD calculation, Dreiding force-field was used and the bond length parameters were modified to reproduce DFT-optimized molecular structure (labeled as amo-NPD-mole). To mimic the deposition process, the initial MD simulation was performed in constant-volume, constant-temperature (NVT) ensemble at a density of 0.1 g cm^{-3} and at a temperature of 573 K for 10 ps. Then the MD simulation was performed under the constant-pressure, constant-temperature (NPT) ensembles for 1.0 ns at 298 K until the density of the system becomes constant. Finally, the structure was geometry optimized. The final density of the structure was 0.95 g cm^{-3} . The amorphous structure, amo-NPD, thus obtained is shown in Figure 3.2b.

The reorganization energies for the isolated NPD molecule (λ_{iso}) and for molecules in the aggregated structure (λ_{agg}) were calculated as provided elsewhere [16, 17, 35, 36]. For the calculations of λ_{agg} , quantum mechanics / molecular mechanics (QM/MM) approach [37] were used to consider intermolecular interaction between molecules. QM/MM calculation (DFT and Dreiding force-field) was performed with surrounding molecules that have a center-to-center distance within 30 \AA . The calculation of the electronic coupling for hole and electron transfer (H_{ij}^+ and H_{ij}^- , respectively) was performed as described in previous work [16, 17, 35, 36] for the molecular pairs that have a center-to-center distance within 25 \AA . Using the values of H_{ij}^+ , H_{ij}^- , λ_{agg}^+ and λ_{agg}^- obtained above, the rate constants for hole and electron transfers

(k_{CT^+} and k_{CT^-} , respectively) under the applied external electric field were calculated according to the following equation based on Marcus theory [4, 5],

$$k_{ij} = \frac{4\pi^2}{h} H_{ij}^2 \frac{1}{\sqrt{4\pi\lambda k_B T}} \exp\left[-\frac{(\lambda + \Delta G_{ij})^2}{4\lambda k_B T}\right], \quad (3.1)$$

where T is the temperature, h is Plank's constant and k_B is Boltzmann's constant. ΔG_{ij} , the free energy difference between the initial and final states of charge hopping between relevant two charged and neutral molecules i and j , is given by Eq. (3.2),

$$\Delta G_{ij} = \Delta E_j - \Delta E_i - qF\Delta x_{ij}, \quad (3.2)$$

where ΔE_i and ΔE_j are the energy of molecules i and j , q is the elementary charge (unit charge), F is the applied external electric field strength, and Δx_{ij} is the distance between molecules i and j along the direction of the applied electric field. The energetic disorder was calculated according to Ref. 17, with taking into account the difference in Coulombic interaction between neighboring molecules. Using the obtained k_{ij} , the probability of charge hopping from a molecule i to molecule j is calculated by the following Eq. (3.3):

$$P_{ij} = \frac{k_{ij}}{\sum k_{ij}} \quad (3.3)$$

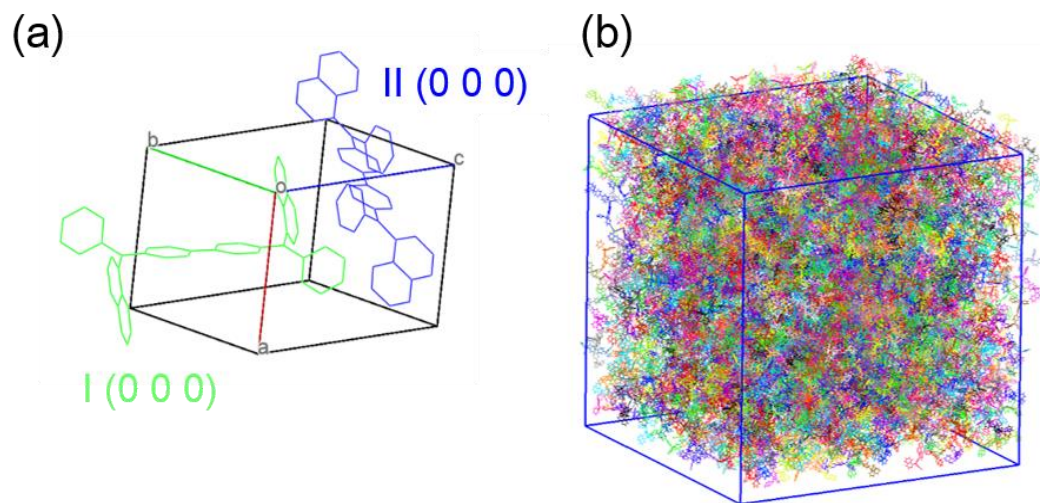


Fig. 3.2. (a) Crystal structure of NPD (cry-NPD). The molecules labeled as I and II are crystallographically independent. (b) MD constructed amorphous structure consists of 4000 molecules of NPD (amo-NPD).

3.3. Results and discussion

3.3.1. Molecular structures and reorganization energies

The experimental and calculated structure parameters of molecules I and II in cry-NPD are shown in Figure 3.1 and Table 3.1. As I and II have almost identical conformation, we will discuss the calculation of I here. From Table 3.1, the calculated bond lengths (r_i) and angles (θ_i) of I in neutral state in the isolated state are in good agreement with experimental values. In contrast, the calculated torsion angles (ϕ_i) are different from the experimental ones, especially for the torsions between two central phenylene (biphenylene) rings (ϕ_7). Figure 3.3 shows the dependence of the relative energy on ϕ_7 of I in neutral and the isolated state when all of the other parameters are fixed. The potential has a minimum at $\phi_7 = 34^\circ$. Thus, experimental ϕ_7 in I (0°), means the central biphenylene of cry-NPD is planar and indicates that it is not in the most stable geometry. In addition, a negative frequency at the B3LYP/6-31G(d) level was found in I. This difference is considered to originate from the effect of intermolecular packing in cry-NPD. In this Chapter, we use the DFT-optimized conformation of I in the isolated state for the λ_{iso} calculation for cry-NPD, according to the previous study [36]. For the calculation of λ_{agg} of cry-NPD, I and II with considering the crystal structure to include intermolecular packing effect, are used and averaged. The optimized structures of neutral, cationic, anionic states for amo-NPD-mole in the isolated state are also shown in Table 3.1. The calculated λ_{iso} and λ_{agg} for cry-NPD as well as amo-NPD are summarized in Table 3.2. In all the cases calculated λ_{iso} (or λ_{agg}) for electron transfer are smaller than those for hole transfer, which indicates a smaller structural relaxation in the anionic state than in the cationic state of an NPD molecule. In the comparison of λ_{iso} for cry-NPD and amo-NPD, they give comparable values,

reflecting their similar optimized geometries. Smaller λ_{agg} for cry-NPD than that of amo-NPD suggest the presence of a higher steric effect in cry-NPD.

Table 3.1. Experimental and calculated structural parameters of the two crystallographically independent NPD molecules (labeled as I and II) in cry-NPD and the structure used for amorphous construction (labeled as amo-NPD-mole). The notation of the structural parameters are shown in Fig. 3.1.

Bond length (Å)			r_1	r_2	r_3	r_4	r_5	r_6	r_7
I	Exp.		1.41	1.43	1.41	1.41	1.43	1.41	1.48
		Neutral	1.42	1.43	1.42	1.42	1.43	1.42	1.48
	Calc.	Cation	1.38	1.44	1.43	1.38	1.44	1.43	1.46
		Anion	1.42	1.44	1.41	1.42	1.44	1.41	1.48
II	Exp.		1.41	1.43	1.42	1.41	1.43	1.42	1.47
		Neutral	1.42	1.43	1.42	1.42	1.43	1.42	1.48
	Calc.	Cation	1.38	1.44	1.43	1.38	1.44	1.43	1.46
		Anion	1.42	1.44	1.41	1.42	1.44	1.41	1.48
amo-NPD-mole		Neutral	1.42	1.43	1.42	1.42	1.43	1.42	1.48
	Calc.	Cation	1.39	1.44	1.43	1.39	1.44	1.44	1.46
		Anion	1.42	1.43	1.41	1.42	1.43	1.41	1.47
Bond angle (°)			θ_1	θ_2	θ_3	θ_4	θ_5	θ_6	
I	Exp.		122	121	118	122	121	118	
	Calc.	Neutral	120	121	118	120	121	118	
		Cation	122	121	117	122	121	117	
		Anion	119	122	119	119	122	119	
II	Exp.		120	122	118	120	122	118	
		Neutral	120	121	118	120	121	118	
	Calc.	Cation	121	122	117	121	122	117	
		Anion	119	122	119	119	122	119	
amo-NPD- mole		Neutral	118	121	119	118	121	119	
	Calc.	Cation	119	122	119	119	122	118	
		Anion	117	122	120	118	122	120	

Torsion angle (°)			ϕ_1	ϕ_2	ϕ_3	ϕ_4	ϕ_5	ϕ_6	ϕ_7
I	Exp.		159	118	137	159	118	137	0
	Calc.	Neutral	151	125	146	153	125	147	34
		Cation	161	118	136	161	118	136	0
		Anion	146	117	153	147	117	154	31
II	Exp.		158	117	134	158	117	134	0
	Calc.	Neutral	151	125	146	153	125	147	34
		Cation	161	118	136	161	118	136	0
		Anion	146	117	154	147	118	154	31
amo-NPD-mole	Calc.	Neutral	147	124	148	148	126	151	35
		Cation	156	114	137	158	114	137	0
		Anion	140	112	152	141	117	159	29

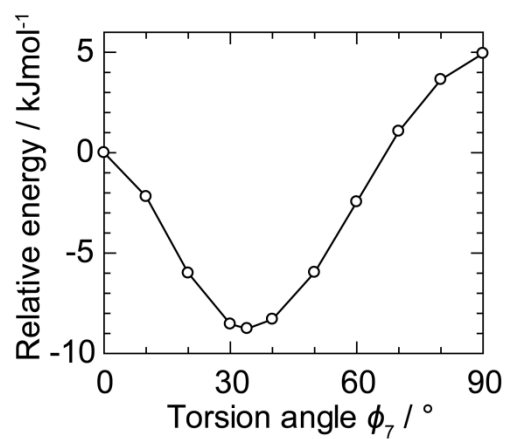


Fig. 3.3. Potential energy surface of I in an isolated state as a function of torsion angle ϕ_7 calculated at the B3LYP/6-31G(d) level. The energy zero is set to the energy at $\phi_7 = 0^\circ$. The torsion angles, bond angles, and bond lengths other than ϕ_7 were fixed at the optimized values of I in Table 3.1.

Table 3.2. Reorganization energies calculated for an isolated molecule (λ_{iso}) and for a molecule including the intermolecular packing effect in cry-NPD or amo-NPD (λ_{agg}).

	cry-NPD		amo-NPD	
	λ_{iso}	λ_{agg}	λ_{iso}	λ_{agg}
Hole	0.323	0.200	0.286	0.289
Electron	0.163	0.130	0.164	0.151

3.3.2. Electronic couplings and energetic disorders

The calculated H_{ij} for cry-NPD and amo-NPD are shown in Figure 3.4. The maximum value for H_{ij}^- ($H_{ij}^-_{\max}$) is larger than that of H_{ij}^+ ($H_{ij}^+_{\max}$) for both cry-NPD and amo-NPD. These results and the calculated λ values in Table 3.2 suggest that NPD has potential as a good electron transporter not only in the crystal but also in the amorphous phase. It can be explained by considering the difference in distribution of the frontier orbitals. Figure 3.5 shows the highest occupied molecular orbital (HOMO) and the lowest unoccupied molecular orbital (LUMO) of I. Compared to the HOMO, which is relatively distributed throughout the entire molecule, the LUMO is strongly localized on two outer naphthyl segments (see also Table 3.3). The frontier orbitals for amo-NPD-mole give a similar result (see Figure 3.6). By taking a closer look at the case of cry-NPD, the pair which gives $H_{ij}^-_{\max}$ has face-to-face intermolecular contact between naphthyl segments (Figure 3.7a). On the other hand, intermolecular contact between naphthyl segments in the pair which gives $H_{ij}^+_{\max}$ (Figure 3.7b) is off the face-to-face position; less effective intermolecular overlaps between orbitals can be formed. This result confirms the research by other authors [38]. In the case of amo-NPD, H_{ij} values have much larger distribution than cry-NPD. In addition, $H_{ij}^+_{\max}$ and $H_{ij}^-_{\max}$ in amo-NPD are larger than those of cry-NPD. No clear correlation is found between H_{ij} and the intermolecular distance both for cry-NPD and for amo-NPD (Figure 3.8). H_{ij} becomes larger when not only intermolecular distance but also relative intermolecular configuration make the frontier orbital overlap large. The overlap of frontier orbitals is significant especially when intermolecular packing of LUMO on the naphthyl segments is close, resulting in large $H_{ij}^-_{\max}$.

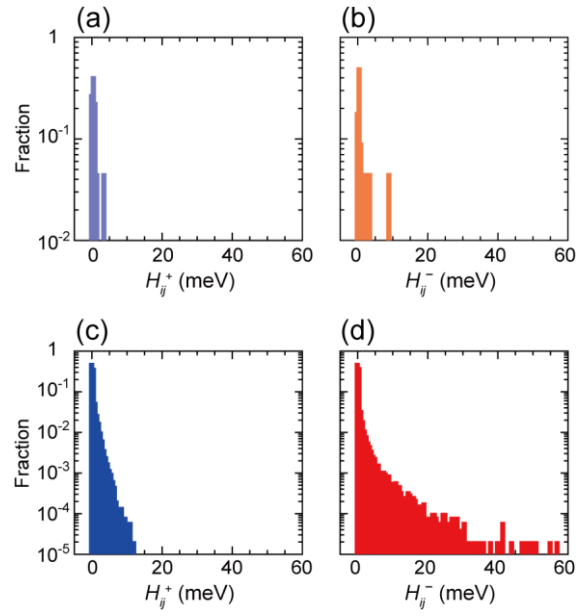


Fig. 3.4. Distribution of the electronic couplings (H_{ij}) for (a) hole in cry-NPD, (b) electron in cry-NPD, (c) hole in amo-NPD and (d) electron in amo-NPD.

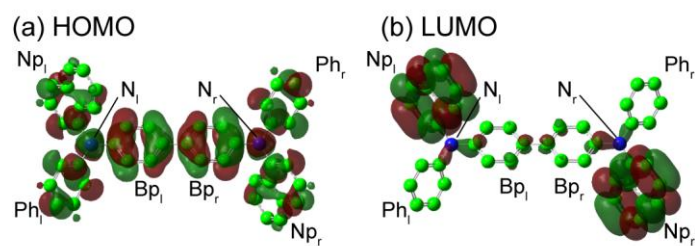


Fig. 3.5. HOMO and LUMO of the NPD molecule I. Ph, Np, and Bp denote the phenyl, naphthyl and biphenyl segments, respectively. N denotes nitrogen atoms. The subscripts l and r denote left and right.

Table 3.3. Contributions of the nitrogen (N), biphenylene (Bp), phenyl (Ph) and naphthyl (Np) moieties of I and amo-NPD-mole to the HOMO and LUMO. The subscript of l or r indicates the left or right side of the molecule in Figs. 3.5 and 3.6.

		N _l	N _r	Bp _l	Bp _r	Ph _l	Ph _r	Np _l	Np _r
I	HOMO	17.6	17.7	18.5	18.4	7.5	7.5	6.4	6.4
	LUMO	0.2	0.2	1.5	1.5	0.5	0.5	47.8	48.0
amo-NPD-mole	HOMO	16.8	16.3	17.0	16.8	8.5	8.4	8.1	8.2
	LUMO	0.2	0.2	2.2	2.2	0.3	0.4	45.7	48.8

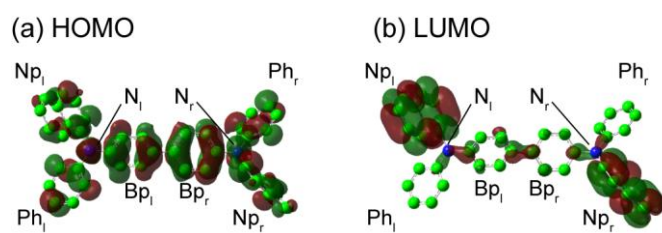


Fig. 3.6. The HOMO and LUMO of amo-NPD-mole. Ph, Np, and Bp denote the phenyl, naphthyl and biphenyl segments, respectively. N denotes nitrogen atoms. The subscripts l and r denote left and right.

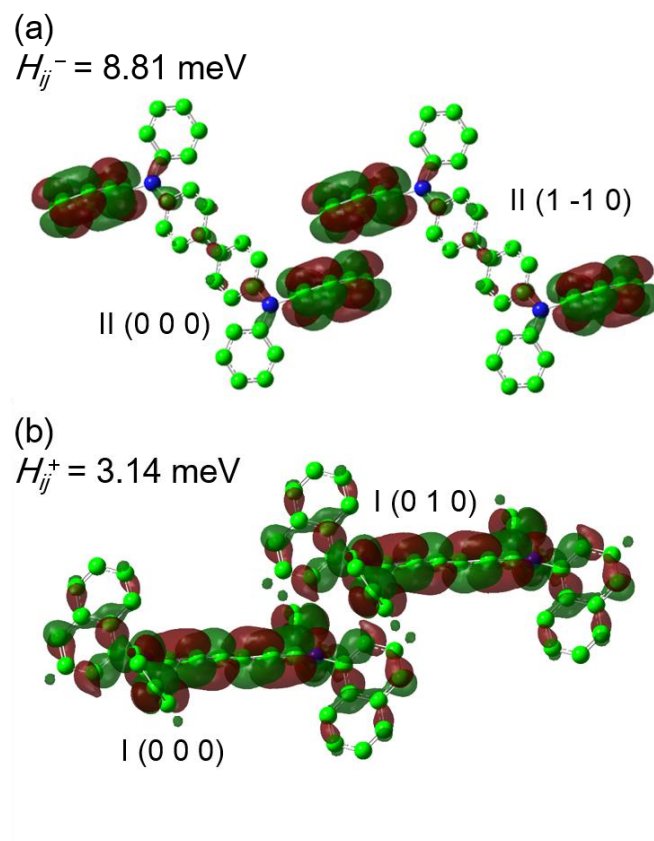


Fig. 3.7. Molecular pairs having the large H_{ij} values for (a) electron and (b) hole transport.

The LUMO and HOMO at the extended Hückel level are also shown.

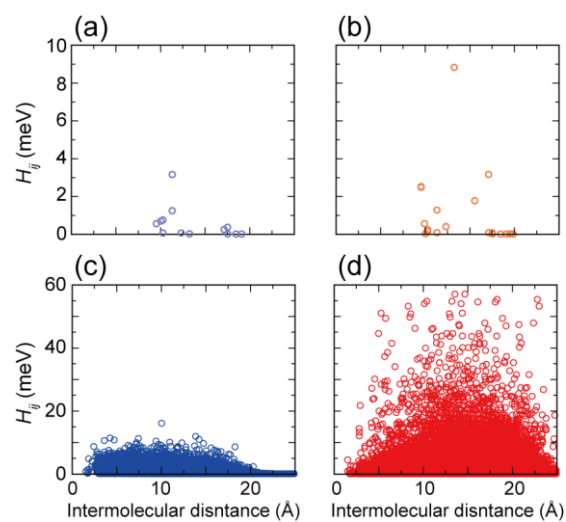


Fig. 3.8. The correlation between H_{ij} and intermolecular distance for (a) hole transfer in cry-NPD, (b) electron transfer in cry-NPD, (c) hole transfer in amo-NPD and (d) electron transfer in amo-NPD.

Figure 3.9 shows the energetic disorders in cry-NPD and amo-NPD. Molecules I and II have slightly different site energies from each other for both electron and hole transfer (Figures 3.9a and 3.9b). As shown in Table 3.1, these molecules have similar geometries, but the energetic disorder in cry-NPD reflects the difference in the steric influence of the surrounding molecules. This result shows that the energetic disorder in the crystal is small but exists. The energetic disorder is small, because the number of different molecules is limited, only two, in the NPD crystals and their structures are similar. On the other hand, the energetic disorder in amo-NPD shows a much larger distribution (Figures 3.9c and 3.9d), reflecting various intermolecular interaction of surrounding molecules in the amorphous phase. GDM assumes Gaussian type distribution for the energetic disorder. However, as is found from Figures 3.9c and 3.9d, the distribution is found to be slightly skewed to the higher energy region for electron transfer. The cause of the deviation from the Gaussian distribution is under investigation. The effect of the energetic disorder on the charge transport is described below.

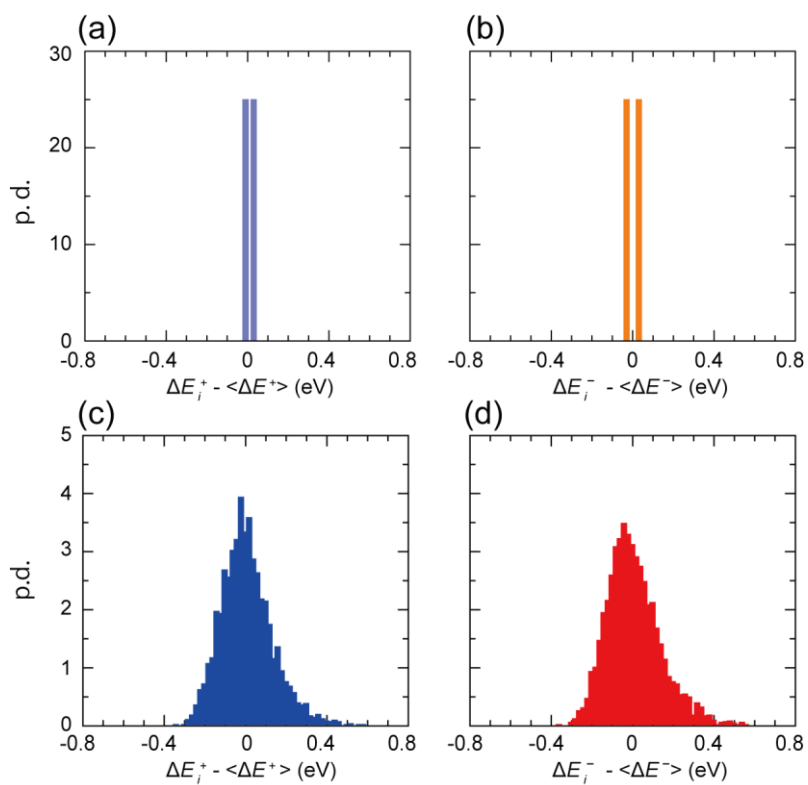


Fig. 3.9. Distributions of site energies for (a) hole in cry-NPD, (b) electron in cry-NPD, (c) hole in amo-NPD and (d) electron in amo-NPD.

3.3.3. Charge transport simulations

Figure 3.10a shows the electric field dependence of the hole and electron mobilities calculated by the kinetic Monte Carlo simulation for cry-NPD with considering energetic disorder. The charge mobilities along the x-, y- and z-axes (See Figure 3.11 for respective axes) provide significantly different values, indicating the highly anisotropic charge transports in cry-NPD. Electron mobility is higher than hole mobility by 1-2 orders of magnitude. This suggests that cry-NPD has a better electron transport ability than hole transport. Compared with the electric field dependence of charge mobility without the energetic disorder (also shown in Figure 3.10a), a slightly lower charge mobility and weakly positive field dependence is observed by considering the energetic disorder. Figure 3.10b shows the electric field dependence of the hole and electron mobilities for amo-NPD. The difference in the charge mobilities for amo-NPD along each axis is significantly small, which indicates that amo-NPD, consisting of 4,000 molecules, successively reproduces the nature of an amorphous structure with random molecular orientations. Experimental charge mobility and its electric field dependencies from Ref. 29 are also shown in Figure 3.10b. When compared with experimental results, the charge mobility calculated without energetic disorder is higher by 1-2 orders of magnitude and has negative field dependence. Consideration of energetic disorder reproduces a positive electric field dependence but gives one order smaller hole mobility. However, electron mobility, as well as its electric field dependence, are well reproduced by considering the energetic disorder.

The electron mobility shows downward convex curves in lower electric field dependence. The charge transport simulation for both the two different structural models (crystal and amorphous models) clarify that the energetic disorder is an essential factor in representing the positive electric field dependence regardless of the degree of structural disorder. Indeed, lower charge mobilities in amo-NPD compared to those in cry-NPD indicate that the charge mobilities in amo-

NPD are lower than those expected from $H_{ij}^-_{\max}$ and $H_{ij}^+_{\max}$ values in amo-NPD (which are larger than those of cry-NPD). This is because $H_{ij}^-_{\max}$ and $H_{ij}^+_{\max}$ do not necessarily contribute to the charge transport. This feature is described in the following sections.

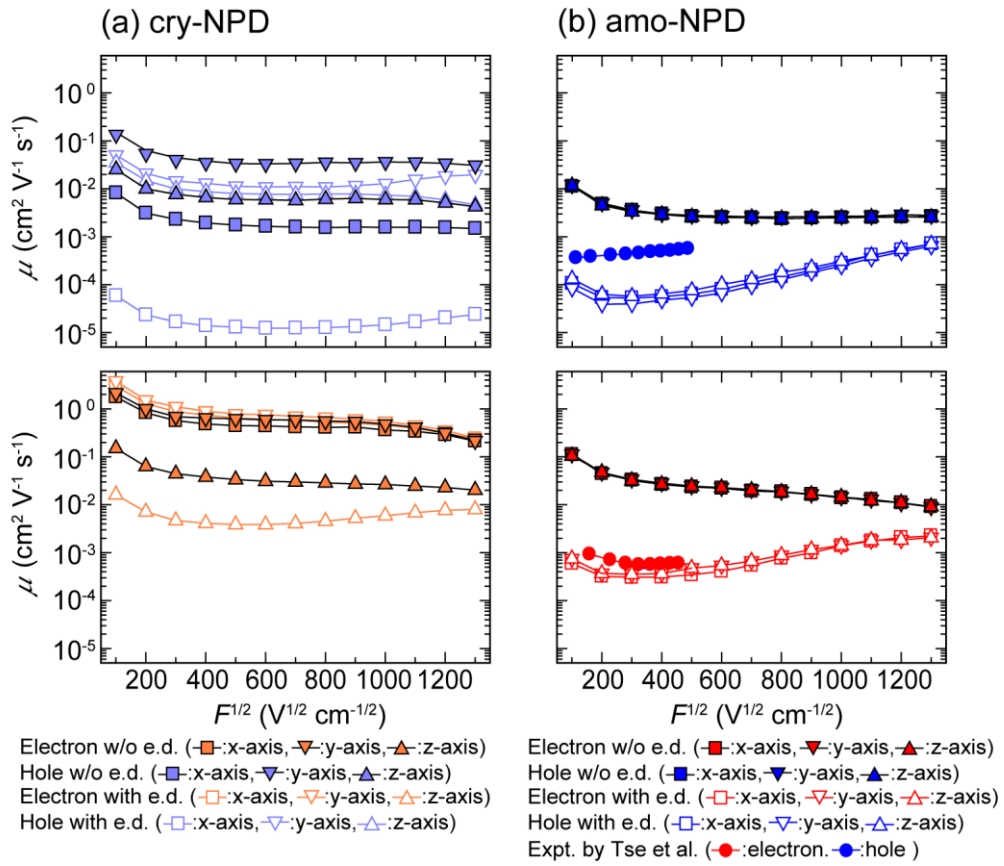


Fig. 3.10. Calculated charge mobility in (a) cry-NPD and (b) amo-NPD. Open symbols: calculated with energetic disorder (e. d.). Filled symbols: calculated without e.d for comparison. Filled circles: experimental data from Ref. 29.

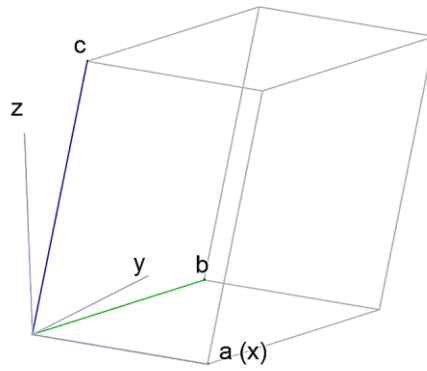


Fig. 3.11. The unit cell axes (a , b , and c) and orthogonal coordinate axes (x , y , and z) for cry-NPD. a -axis is in the same direction as the x -axis.

Figure 3.12 shows the comparison of charge transport trajectories for one electron in cry-NPD and amo-NPD considering energetic disorder; there is a clear difference in the trajectories between them. For the case of cry-NPD at $300 \text{ V}^{1/2}\text{cm}^{-1/2}$, the electron reaches the counter electrode using mostly linear routes, with some small fluctuations (Figure 3.12a). From detailed analysis, not only forward hops but also a certain degree of backward hops occur. At $1300 \text{ V}^{1/2}\text{cm}^{-1/2}$, an almost linear route is used, although the route is tilted from the electric field direction (Figure 3.12b). This trend is similar in the case calculated without the energetic disorder (see also Figure 3.13). On the contrary, much more complicated routes are observed in amo-NPD at $300 \text{ V}^{1/2}\text{cm}^{-1/2}$ (Figure 3.12c). Forward and backward charge hopping in many directions occur, indicating diffusive behavior in amo-NPD. The diffusive behavior is unchanged irrespective of the presence of the energetic disorder, although the charge hopping pathway changes to some degree. At a higher applied electric field, $1300 \text{ V}^{1/2}\text{cm}^{-1/2}$, the charge in amo-NPD reaches the counter electrode using more linear routes (Figure 3.12d). The charge transport pathway in the amo-NPD becomes similar with that of in the cry-NPD. This is because $-qF\Delta x_{ij}$ in Eq. (3.1) preferentially determines ΔG under higher electric field and results in the increased contribution of the drift transport. Similarly in the case at $300 \text{ V}^{1/2}\text{cm}^{-1/2}$, the linearity of charge transport path at $1300 \text{ V}^{1/2}\text{cm}^{-1/2}$ is substantially unchanged irrespective of the presence of the energetic disorder. Here, again, our study is designed to assess the effect of small and large structural disorder on the charger transport using NPD in the crystal and the amorphous phase. These results can be interpreted as that the more linear pathway in cry-NPD compared with amo-NPD at the same field strength is mainly related to its smaller structural disorder. Oppositely, as shown in the case of amo-NPD, the larger structural disorder is the major factor for the complicated charge-transport trajectory. These are as a matter of course. However, the trajectory becomes close to linear even for amo-NPD under higher applied electric field.

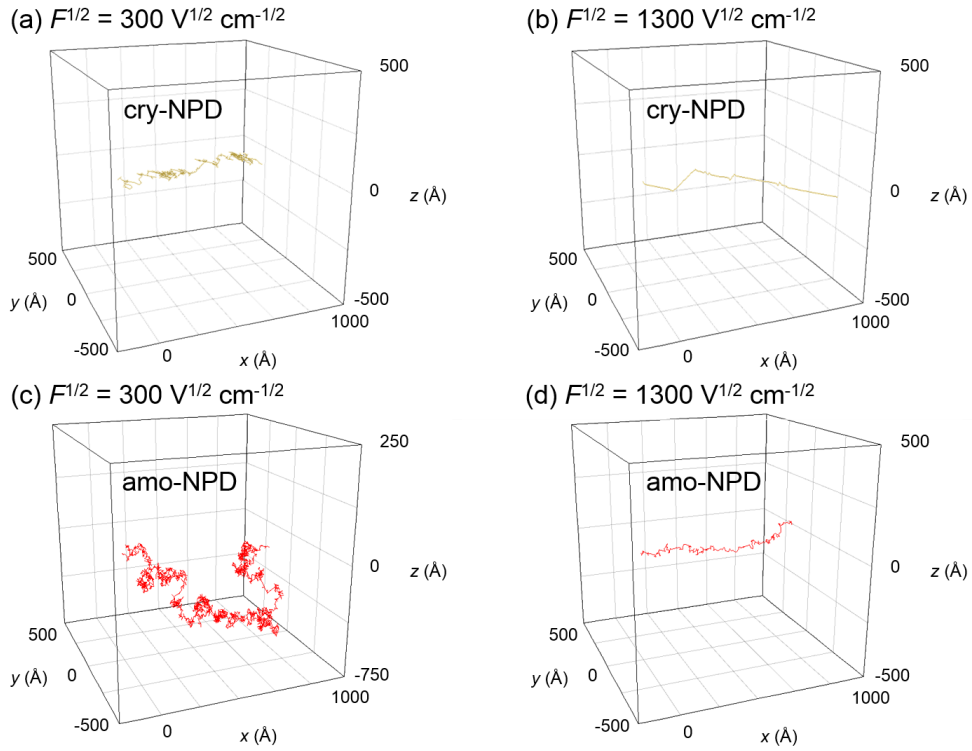


Fig. 3.12. Electron transport trajectories under the electric fields applied in the direction of x-axis at (a) $300 \text{ V}^{1/2} \text{ cm}^{-1/2}$ in cry-NPD, (b) $1300 \text{ V}^{1/2} \text{ cm}^{-1/2}$ in cry-NPD, (c) $300 \text{ V}^{1/2} \text{ cm}^{-1/2}$ in amo-NPD and (d) $1300 \text{ V}^{1/2} \text{ cm}^{-1/2}$ in amo-NPD. The energetic disorders are considered for all the calculations.

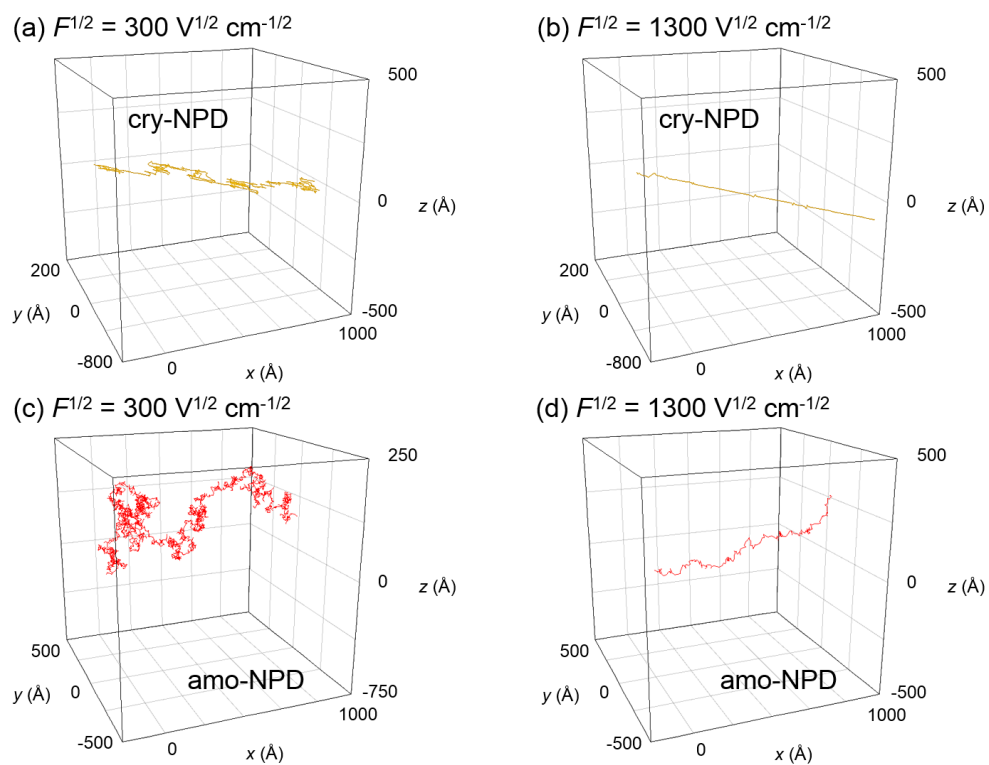


Fig. 3.13. Electron transport trajectories under the electric fields applied in the direction of x-axis (in the same direction as the a-axis) at (a) $300 \text{ V}^{1/2} \text{ cm}^{-1/2}$ in cry-NPD, (b) $1300 \text{ V}^{1/2} \text{ cm}^{-1/2}$ in cry-NPD, (c) $300 \text{ V}^{1/2} \text{ cm}^{-1/2}$ in amo-NPD and (d) $1300 \text{ V}^{1/2} \text{ cm}^{-1/2}$ in amo-NPD. The energetic disorders are ignored for all the calculations.

In order to understand the contributions of energetic and structural disorders in more detail, we analyzed the numbers of difference between forward and backward charge hops (N_{diff}), which is an important factor in understanding charge-hopping phenomena [16]. Figure 3.14a and 3.14b (in the left axis) show the correlation between N_{diff} and H_{ij}^- for cry-NPD. A strong dependence is observed between N_{diff} and H_{ij}^- for cry-NPD for both lower and higher electric field. Calculated results without energetic disorder are shown in Figure 3.15. A similar trend is observed regardless of the presence of the energetic disorder. Figures 3.14c and 3.14d show the correlation between N_{diff} and H_{ij}^- for amo-NPD. In this case, no clear relationship is found between N_{diff} and H_{ij}^- . Instead, there is a correlation between N_{diff} and energetic disorder in amo-NPD especially in lower electric field (Figure 3.16). On the other hand, relatively weak correlation is observed in the higher electric field. This indicates the increased contribution of $-qF\Delta x_{ij}$ in Eq. (3.1) on ΔG reduces the contribution of $\Delta E_j - \Delta E_i$ and H_{ij}^- . Here, we introduce the contribution of each molecular pair to the migration distance (averaged for the trials of 10,000 charges) as follows:

$$\Delta X = N_{\text{diff}} \cdot \Delta x \quad (3.4)$$

Here, ΔX is the distance between the neighboring relevant molecules along the electric field. Figures 3.17 and 3.18 show the correlation between N_{diff} and ΔX calculated with and without the energetic disorder. It is evident that N_{diff} strongly correlates with ΔX for both cry-NPD and amo-NPD without the regards of the presence of the energetic disorder. Figures 3.14 and 3.15 (in the right axis) also show a trend between H_{ij} and ΔX . The trend is similar with the case for the correlation between N_{diff} and H_{ij}^- . In order to understand the differences in charge hopping for cry-NPD and amo-NPD, molecular-level approach is required. Table 3.4 shows the number of charge hops in forward (N_{fwd}), backward (N_{bwd}), the sum of them ($N_{\text{all}} = N_{\text{fwd}} + N_{\text{bwd}}$) and the difference ($N_{\text{diff}} = N_{\text{fwd}} - N_{\text{bwd}}$) during the electron transport for the pairs with the highest three

ΔX values (see Figures 3.19-3.22 for respective molecular pairs). $N_{\text{all}} / N_{\text{diff}}$ in this Table exhibits the efficiency of charge hops of each pair. In the present kinetic Monte Carlo simulations, charges travel between the two electrodes with 100 nm distances. Therefore, the sum of ΔX for a charge is 100 nm. In the case of cry-NPD with the energetic disorder (Table 3.4), the pairs having top two H_{ij} are mostly used at $300 \text{ V}^{1/2}\text{cm}^{-1/2}$ (the sum of ΔX is $51.4 + 37.7 = 89.1 \text{ nm}$). The other pairs are seldom used during the charge transport. For all the pairs, frequent forward and backward charge hopping are seen at $300 \text{ V}^{1/2}\text{cm}^{-1/2}$; the values of $N_{\text{all}} / N_{\text{diff}}$ were 4.47-5.69. These results agree with a relatively linear but fluctuating charge transport trajectory at $300 \text{ V}^{1/2}\text{cm}^{-1/2}$ in Figure 3.12. In contrast, at $1300 \text{ V}^{1/2}\text{cm}^{-1/2}$, $N_{\text{all}} / N_{\text{diff}}$ for the pairs with top three ΔX values are almost 1, indicating charges hop only forward direction under a higher applied electric field. This trend is unchanged when the simulation is performed without the energetic disorder. In order to elucidate the mechanism of charge hopping in cry-NPD, we focused on the distribution of the P_{ij} (the definition is provided in Eq. (3.3) above in this Chapter) of each molecular pair. Specifically, P_{ij} provides information about the charge hopping destination in whether or not the charge can move out of that molecular pair, otherwise returns to the starting molecule. Figures 3.23a and 3.23b show the P_{ij} in cry-NPD at $300 \text{ V}^{1/2}\text{cm}^{-1/2}$ with considering energetic disorder. The $H_{ij}^-_{\text{max}}$ (II (0 0 0) - II (1 -1 0)) pair has P_{ij} of 0.46 for the charge hopping toward the applied electric field direction, which is the largest among charge hoppings from II (0 0 0). P_{ij} of the $H_{ij}^-_{\text{max}}$ (II (0 0 0) - II (-1 1 0)) pair toward the opposite direction has a smaller value (0.30). The second largest H_{ij}^- pair of (I (0 0 0) - I (1 1 0)) (denoted as $H_{ij}^-_{\text{2nd}}$) toward the applied electric field direction (0.43) is also larger than that in the opposite direction, $H_{ij}^-_{\text{2nd}}$ (I (0 0 0) - I (-1 -1 0)) (0.30). The difference in P_{ij} along the applied electric field and its opposite direction indicates that the charge hopping toward the applied electric field direction is totally advantageous. Other than above, charge hopping from I to II (or II to I) have

several percent of the total P_{ij} . Once these pairs are used, the hopping site (I or II) shifts to either II or I. This is considered to be how the partial fluctuation of charge transport path and some deviation from a linear trajectory is observed in cry-NPD at $300 \text{ V}^{1/2}\text{cm}^{-1/2}$. In more detail, the sum of P_{ij} values for the hopping from II (or I) to I (or II) explains the degree of contribution of each pair at $300 \text{ V}^{1/2}\text{cm}^{-1/2}$. The sum of P_{ij} values for the hops from I to II ($0.02 + 0.051 + 0.068 = 0.139$, with considering the energetic disorder) is smaller than the sum of P_{ij} values for hops from II to I ($0.076 + 0.082 + 0.046 = 0.204$). This makes the hopping starting from I advantageous than that starting from II at $300 \text{ V}^{1/2}\text{cm}^{-1/2}$. These differences in P_{ij} can be an explanation for the reason why the ΔX of $H_{ij}^-_{\text{max}}$ (starting from II) is smaller than that of $H_{ij}^-_{\text{2nd}}$ (starting from I). At $1300 \text{ V}^{1/2}\text{cm}^{-1/2}$, as shown in Figures 3.23c and 3.23d, the distribution of P_{ij} changes. The $H_{ij}^-_{\text{max}}$ (II (0 0 0) - II (1 -1 0)) pair toward the applied electric field direction and $H_{ij}^-_{\text{2nd}}$ (I (0 0 0) - I (1 1 0)) pair toward the applied electric field direction occupy most of respective P_{ij} (0.91 and 0.76, respectively). On the other hand, respective P_{ij} in the opposite direction for those pairs become negligible (0.001 and 0.0009, respectively). Therefore, charge hopping in the forward direction will be much more advantageous. It should be noted that the (I (0 0 0) - II (1 0 -1)) pair has 0.17 of P_{ij} ; thus, theoretically, 17% of charges will hop from I to II. This makes the hopping starting from II more beneficial than I at $1300 \text{ V}^{1/2}\text{cm}^{-1/2}$. As a result the $H_{ij}^-_{\text{max}}$ (II (0 0 0) - II (1 -1 0)) pair will be certainly advantageous than other paths. Although there is some difference in P_{ij} values the trend is substantially unchanged when the simulation is performed without the consideration of energetic disorder (Figure 3.24). This could be an explanation for the linear charge hopping trajectory in cry-NPD at $1300 \text{ V}^{1/2}\text{cm}^{-1/2}$.

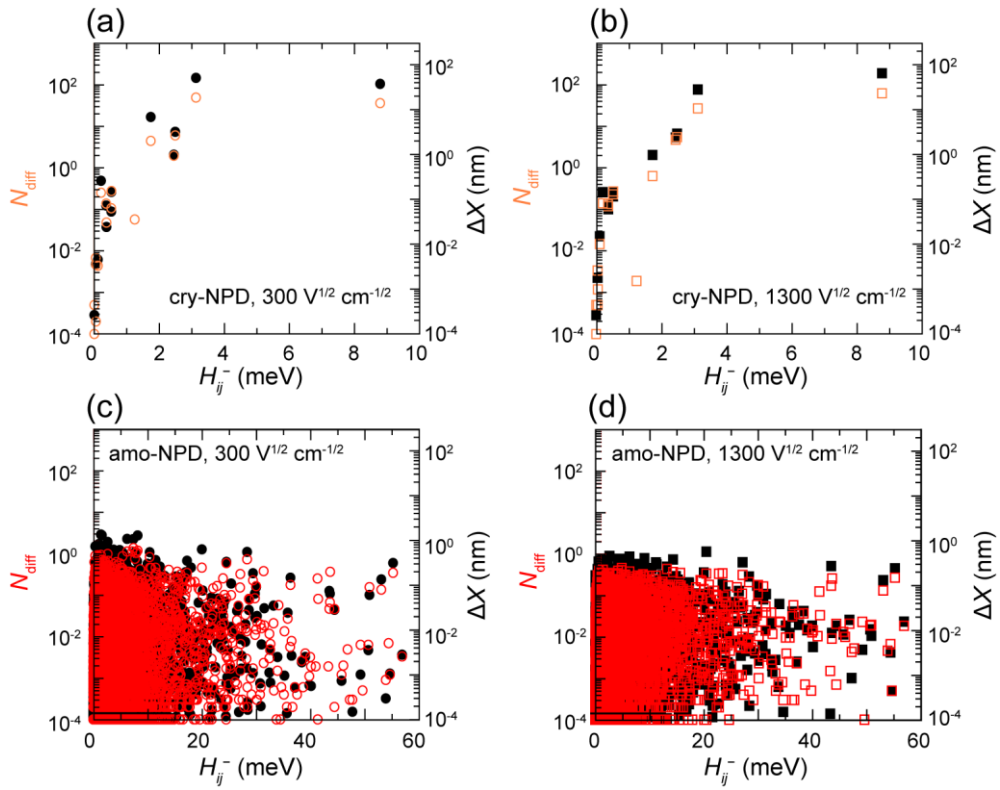


Fig. 3.14. Open symbols: Correlation of the numbers of difference between forward and backward charge hops (N_{diff}) and the electronic couplings (H_{ij}^-) for electron transfer. Filled symbols: Correlation of contributions to the migrations distance of a charge (ΔX) and H_{ij}^- . (a) $300 \text{ V}^{1/2} \text{ cm}^{-1/2}$ in cry-NPD, (b) $1300 \text{ V}^{1/2} \text{ cm}^{-1/2}$ in cry-NPD, (c) $300 \text{ V}^{1/2} \text{ cm}^{-1/2}$ in amo-NPD and (d) $1300 \text{ V}^{1/2} \text{ cm}^{-1/2}$ in amo-NPD. The energetic disorders are considered for all the calculations.

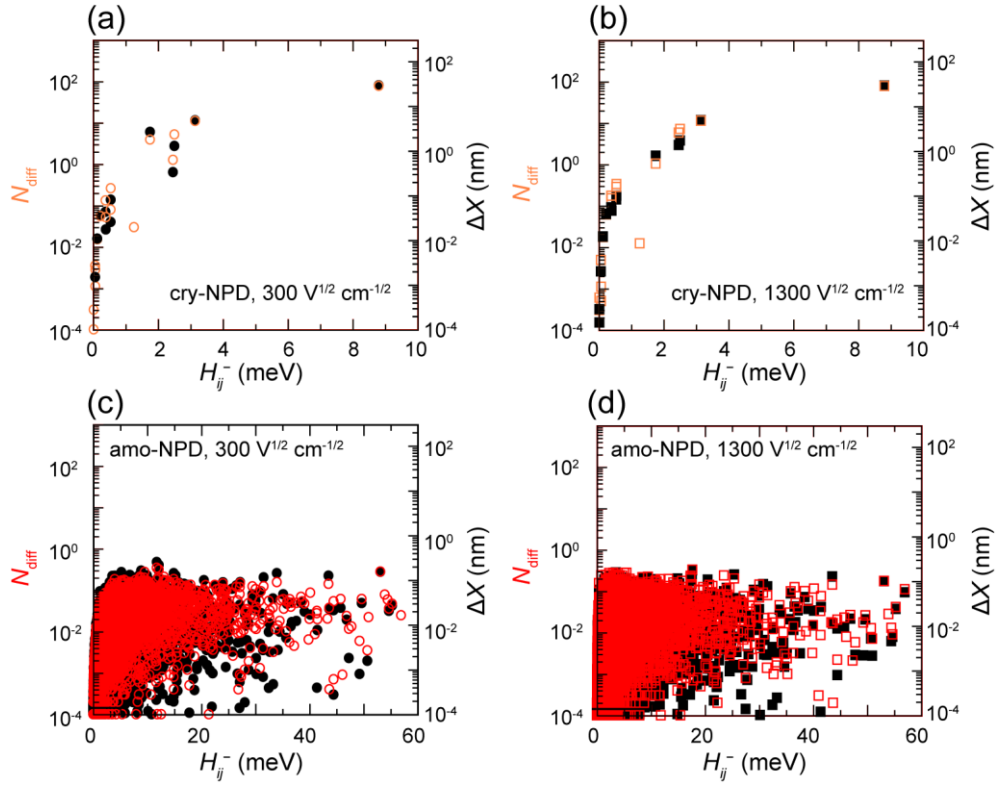


Fig. 3.15. Open symbols: Correlation of the numbers of the difference between forward and backward charge hops (N_{diff}) and the electronic coupling for electron transfer (H_{ij}^-). Filled symbols: Correlation of contributions to the migrations distance of a charge (ΔX) and H_{ij}^- . (a) $300 \text{ V}^{1/2} \text{ cm}^{-1/2}$ in cry-NPD, (b) $1300 \text{ V}^{1/2} \text{ cm}^{-1/2}$ in cry-NPD, (c) $300 \text{ V}^{1/2} \text{ cm}^{-1/2}$ in amo-NPD and (d) $1300 \text{ V}^{1/2} \text{ cm}^{-1/2}$ in amo-NPD. The energetic disorders are neglected for all the calculations.

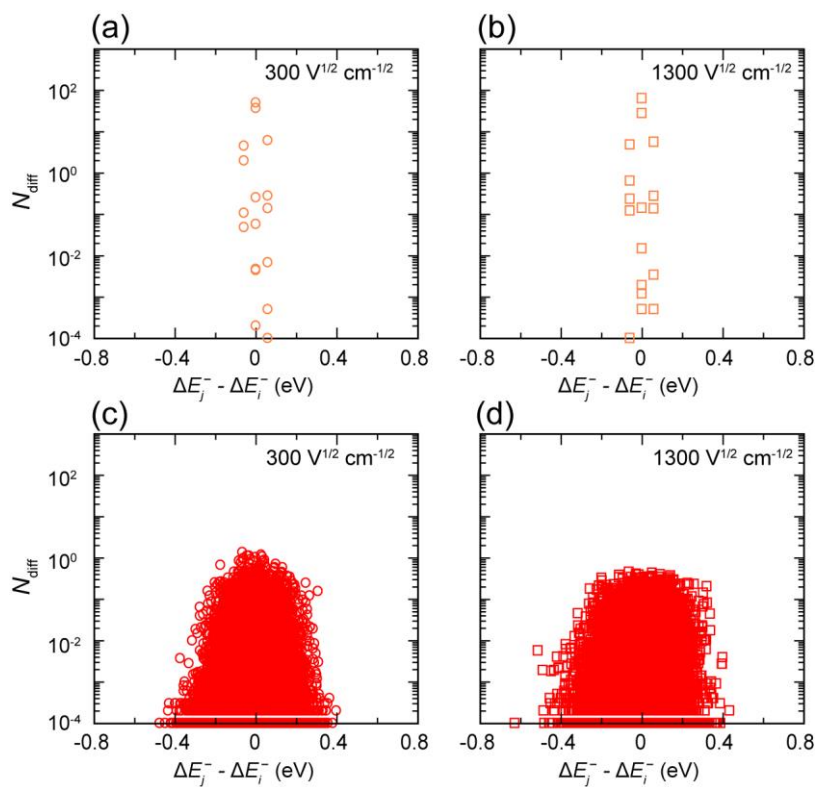


Fig. 3.16. Correlation of N_{diff} and energetic disorder for electron transfer at (a) $300 \text{ V}^{1/2} \text{ cm}^{-1/2}$ in cry-NPD, (b) $1300 \text{ V}^{1/2} \text{ cm}^{-1/2}$ in cry-NPD, (c) $300 \text{ V}^{1/2} \text{ cm}^{-1/2}$ in amo-NPD and (d) $1300 \text{ V}^{1/2} \text{ cm}^{-1/2}$ in amo-NPD.

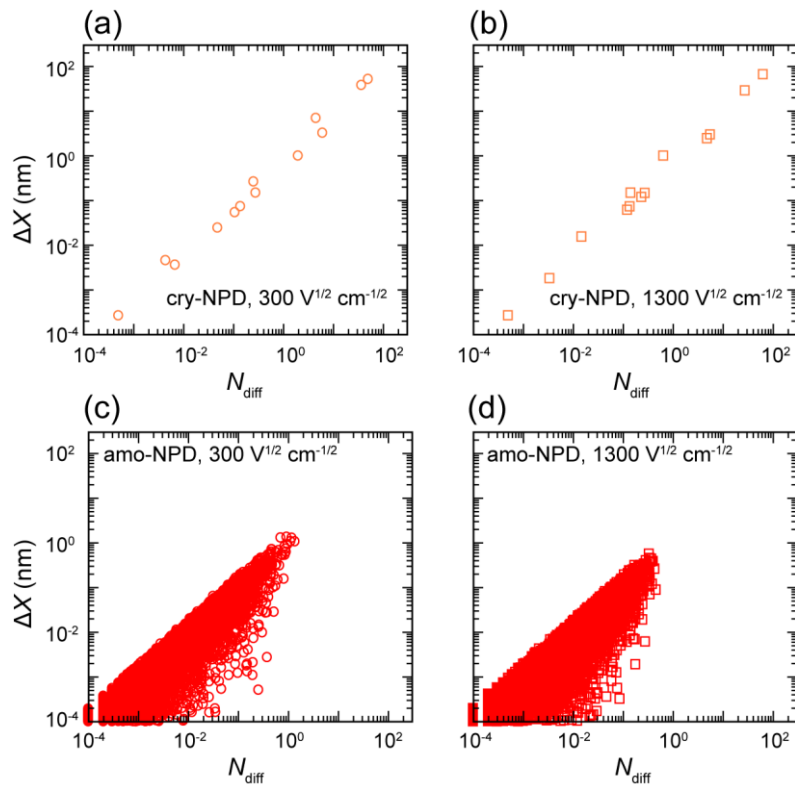


Fig. 3.17. Correlation of ΔX and N_{diff} for electron transfer at (a) $300 \text{ V}^{1/2} \text{ cm}^{-1/2}$ in cry-NPD, (b) $1300 \text{ V}^{1/2} \text{ cm}^{-1/2}$ in cry-NPD, (c) $300 \text{ V}^{1/2} \text{ cm}^{-1/2}$ in amo-NPD and (d) $1300 \text{ V}^{1/2} \text{ cm}^{-1/2}$ in amo-NPD. The energetic disorders are considered for all the calculations.

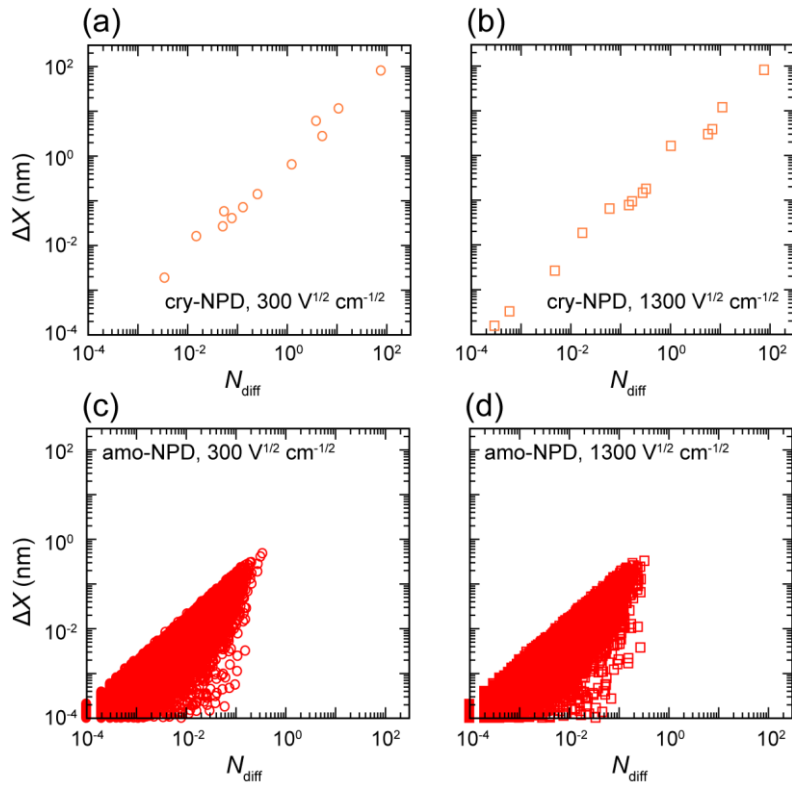


Fig. 3.18. Correlation of ΔX and N_{diff} for electron transfer at (a) $300 \text{ V}^{1/2} \text{ cm}^{-1/2}$ in cry-NPD, (b) $1300 \text{ V}^{1/2} \text{ cm}^{-1/2}$ in cry-NPD, (c) $300 \text{ V}^{1/2} \text{ cm}^{-1/2}$ in amo-NPD and (d) $1300 \text{ V}^{1/2} \text{ cm}^{-1/2}$ in amo-NPD. The energetic disorders are ignored for all the calculations.

Table 3.4. Number of hops in the forward direction (N_{fwd}), backward direction (N_{bwd}), the sum ($N_{\text{all}} = N_{\text{fwd}} + N_{\text{bwd}}$), and the difference ($N_{\text{diff}} = N_{\text{fwd}} - N_{\text{bwd}}$) for the molecular pairs having largest three ΔX values.

Energetic disorder	$F^{1/2}$ ($\text{V}^{1/2} \text{ cm}^{-1/2}$)	H_{ij}^- (meV)	Number of hops				$N_{\text{all}}/N_{\text{diff}}$	ΔX (nm)	
			N_{fwd}	N_{bwd}	N_{all}	N_{diff}			
cry- NPD	On	3.15	167	117	283	49.8	5.69	51.4	
		300	8.81	123	86.1	209	36.6	5.71	37.7
		1.76	12.3	7.80	20.1	4.50	4.47	6.90	
		8.81	63.6	0.08	63.7	63.5	1.00	65.5	
		1300	3.15	27.6	0.03	27.6	27.5	1.00	28.4
		2.51	6.13	0.55	6.69	5.58	1.20	2.95	
	Off	8.81	257	179	436	77.4	5.63	79.8	
		300	3.15	36.3	25.3	61.5	11.0	5.60	11.3
		1.76	11.1	7.21	18.3	3.88	4.71	5.96	
		8.81	77.9	0.09	78.0	77.8	1.00	80.2	
		1300	3.15	11.3	0.01	11.4	11.3	1.00	11.7
		2.51	7.34	0.21	7.55	7.14	1.06	3.77	
amo- NPD	On	1.42	2.45	1.52	3.97	0.93	4.27	1.34	
		300	1.60	3.51	2.80	6.30	0.71	8.93	1.29
		8.19	559	558	1116	1.12	948	1.28	
		20.5	1.23	0.89	2.12	0.33	6.40	0.56	
		1300	2.64	0.36	0.01	0.37	0.34	1.08	0.45
		6.34	0.56	0.19	0.76	0.37	2.05	0.43	
	Off	11.8	2.91	2.57	5.48	0.35	15.8	0.48	
		300	12.2	4.34	4.03	8.37	0.32	26.5	0.40
		12.1	2.46	2.25	4.71	0.21	22.8	0.30	
		17.7	0.43	0.10	0.52	0.33	1.59	0.32	
		1300	3.53	0.19	0.00	0.19	0.19	1.00	0.28
		25.4	0.21	0.01	0.20	0.20	1.11	0.25	

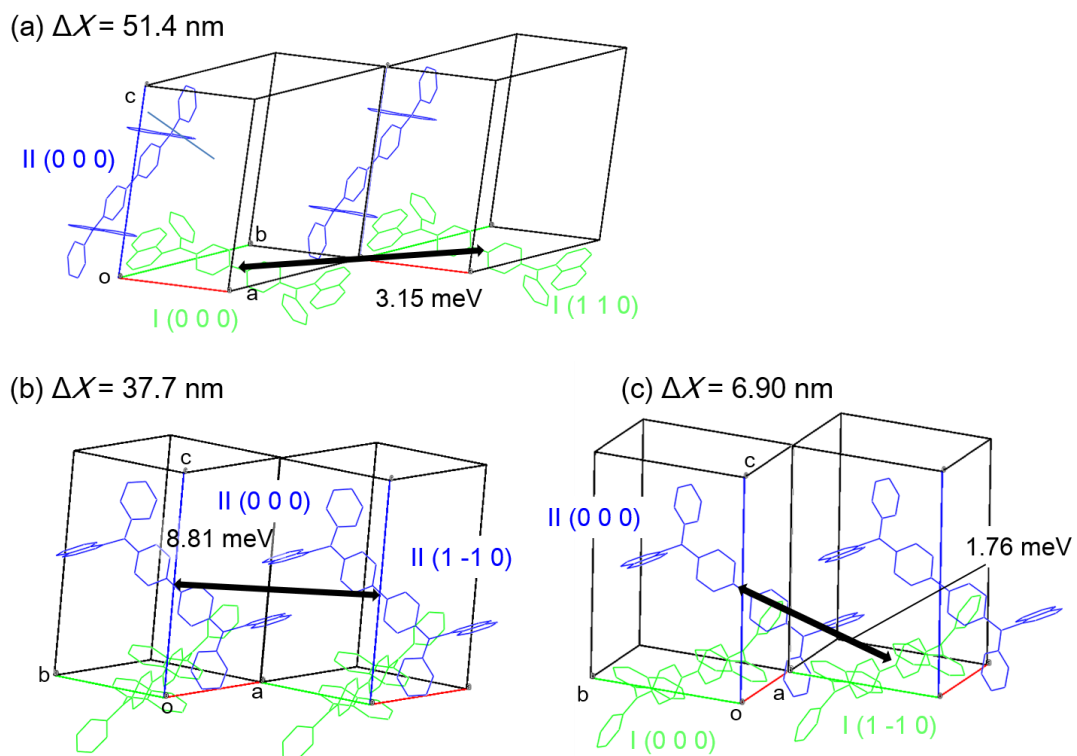


Fig. 3.19. The values of H_{ij}^- for the molecular pairs with (a) the largest ΔX , (b) the second largest ΔX and (c) the third largest ΔX for electron transfer in cry-NPD along a-axis (in the same direction as the x-axis) at a $300 \text{ V}^{1/2} \text{ cm}^{-1/2}$. The energetic disorders are considered for all the calculations.

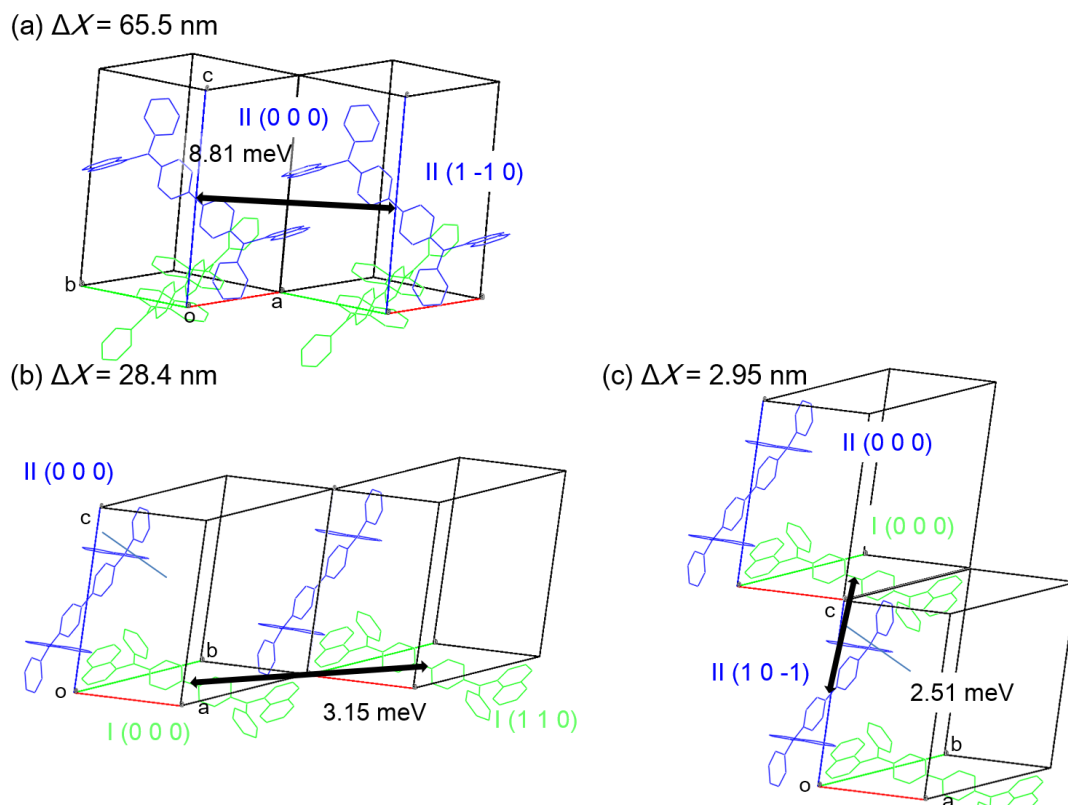


Fig. 3.20. The values of H_{ij}^- for the molecular pairs with (a) the largest ΔX , (b) the second largest ΔX and (c) the third largest ΔX for electron transfer in cry-NPD along a-axis (in the same direction as the x-axis) at a $1300 \text{ V}^{1/2} \text{ cm}^{-1/2}$. The energetic disorders are considered for all the calculations.

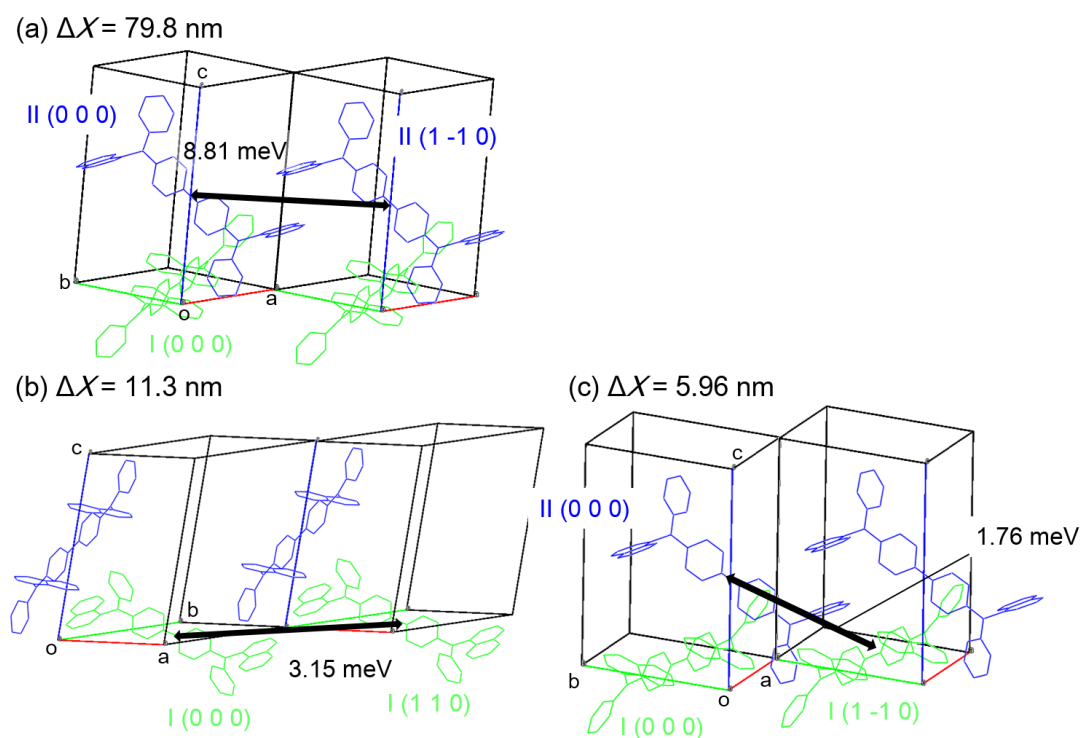


Fig. 3.21. The values of H_{ij}^- for the molecular pairs with (a) the largest ΔX , (b) the second largest ΔX and (c) the third largest ΔX for electron transfer in cry-NPD along a-axis (in the same direction as the x-axis) at a $300 \text{ V}^{1/2} \text{ cm}^{-1/2}$. The energetic disorders are ignored for all the calculations.

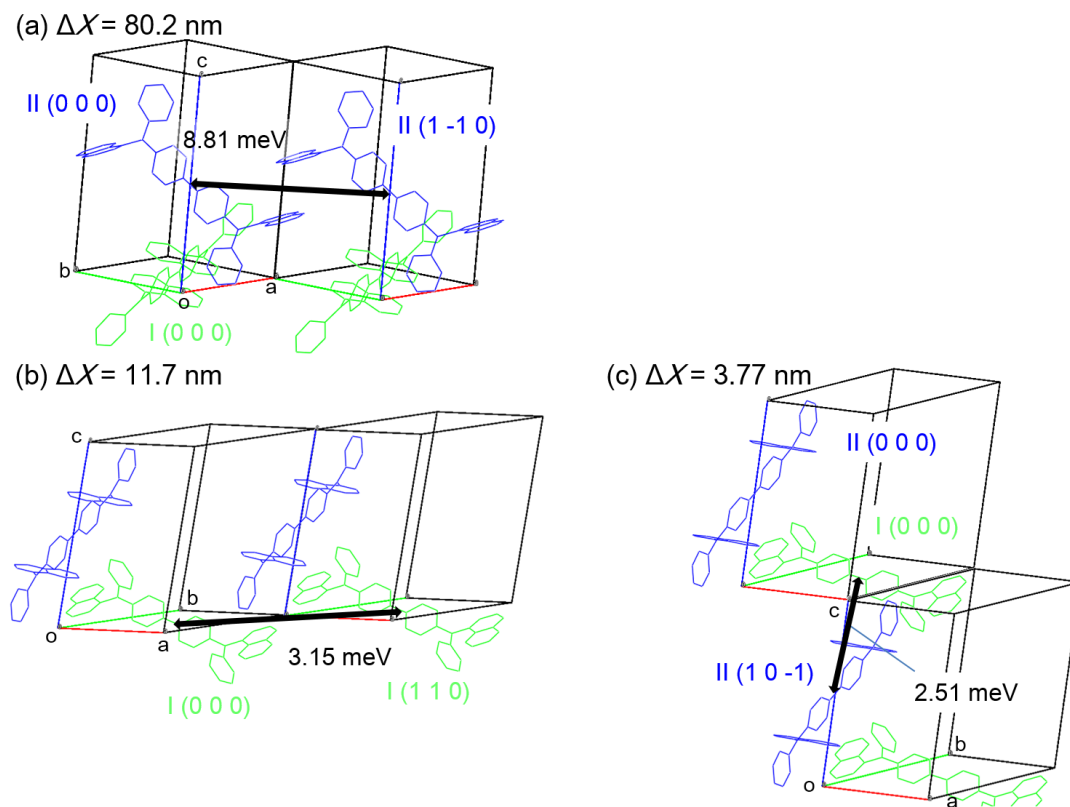


Fig. 3.22. The values of H_{ij}^- for the molecular pairs with (a) the largest ΔX , (b) the second largest ΔX and (c) the third largest ΔX for electron transfer in cry-NPD along a-axis (in the same direction as the x-axis) at a $1300 \text{ V}^{1/2} \text{ cm}^{-1/2}$. The energetic disorders are ignored for all the calculations.

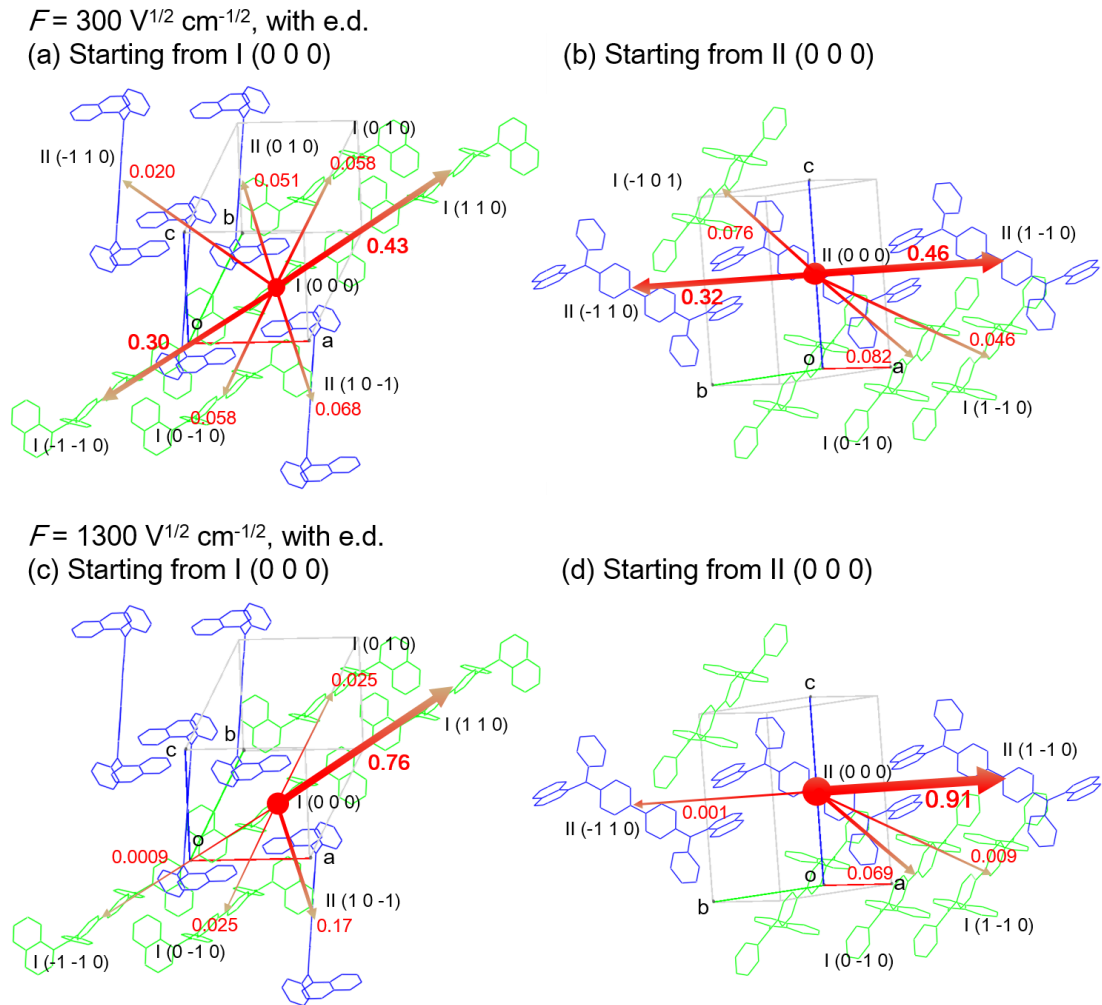


Fig. 3.23. The probabilities of hopping (P_{ij}) in cry-NPD at a (a) $300 \text{ V}^{1/2} \text{ cm}^{-1/2}$, $i = \text{I}$, (b) $300 \text{ V}^{1/2} \text{ cm}^{-1/2}$, $i = \text{II}$, (c) $1300 \text{ V}^{1/2} \text{ cm}^{-1/2}$, $i = \text{I}$, and (d) $1300 \text{ V}^{1/2} \text{ cm}^{-1/2}$, $i = \text{II}$. The electric field is applied along x-axis and the energetic disorder (e.d.) is considered.

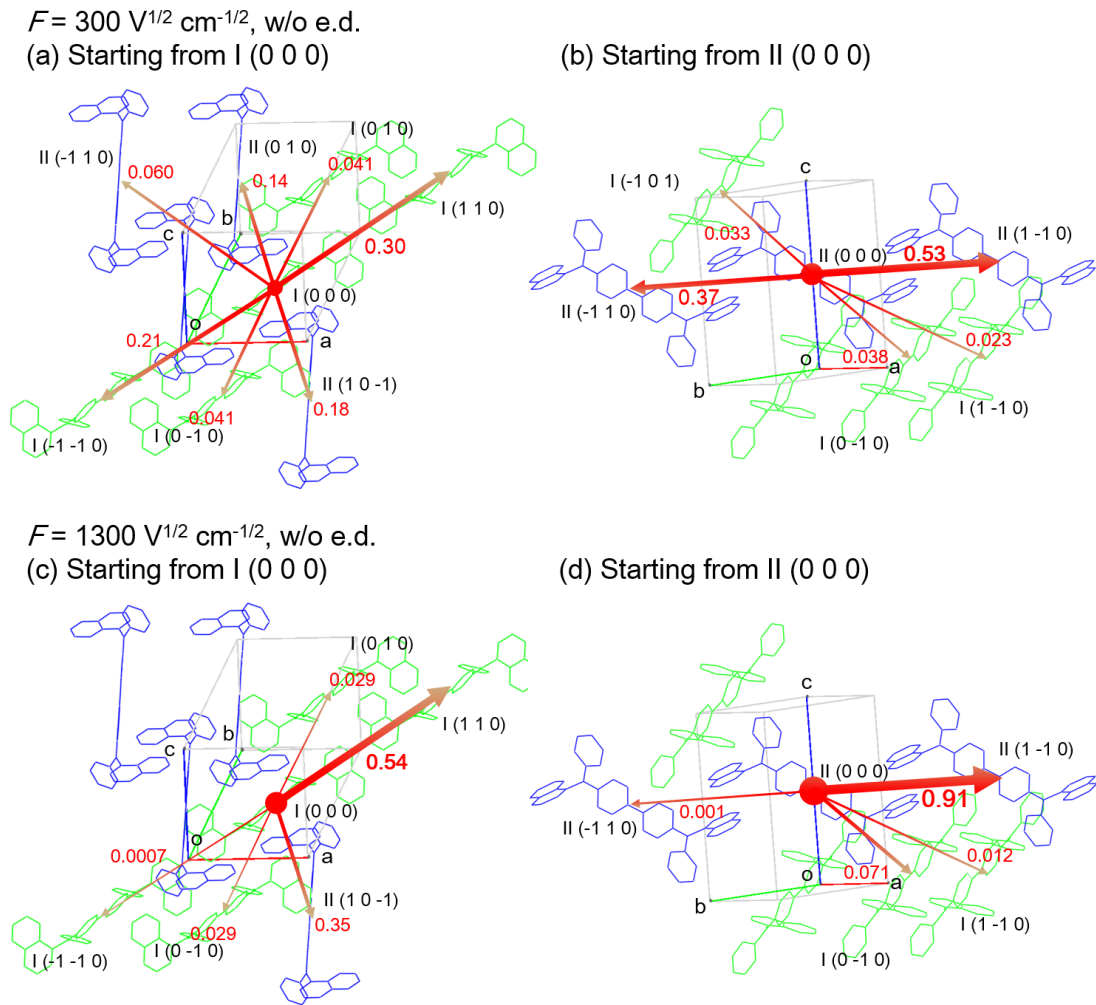


Fig. 3.24. The probabilities of hopping (P_{ij}) in cry-NPD at a (a) $300 \text{ V}^{1/2} \text{ cm}^{-1/2}$, $i = \text{I}$, (b) $300 \text{ V}^{1/2} \text{ cm}^{-1/2}$, $i = \text{II}$, (c) $1300 \text{ V}^{1/2} \text{ cm}^{-1/2}$, $i = \text{I}$, and (d) $1300 \text{ V}^{1/2} \text{ cm}^{-1/2}$, $i = \text{II}$. The electric field is applied along x-axis and the energetic disorder (e.d.) is ignored.

Table 3.4 also shows the case of amo-NPD. Many molecular pairs are used during the charge transport in amo-NPD and thus ΔX values for respective molecular pairs in amo-NPD are smaller than that of cry-NPD as a whole. Figures 3.25-3.28 show H_{ij}^- , ΔX_{\max} and $\Delta X_{2\text{nd}}$ pairs in amo-NPD. In amo-NPD, the contribution to ΔX from H_{ij}^- pair (Figures 3.25a, 3.26a, 3.27a and 3.28a) is significantly small, regardless of the inclusion of energetic disorder. The largest ΔX is given by the pairs that have a much smaller H_{ij} (Figures 3.25b, 3.26b, 3.27b and 3.28b). As confirmed by our previous papers [16, 17] it is not necessarily true that the largest ΔX_{\max} is given by the largest H_{ij} pair in the amorphous phase. This is completely different from the crystalline case, as analyzed above. As shown in Table 3.4, when the energetic disorder is considered, ΔX_{\max} at $300 \text{ V}^{1/2}\text{cm}^{-1/2}$ is given by the pair with $H_{ij} = 1.42 \text{ meV}$, of which the H_{ij} is smaller than those of the second (1.60 meV) and third (8.19 meV) largest pairs. Comparable N_{fwd} and N_{bwd} at $300 \text{ V}^{1/2}\text{cm}^{-1/2}$ tell us that the charges move back and forth frequently. $N_{\text{all}}/N_{\text{diff}}$ values of amo-NPD are equal to or greater than that of cry-NPD at $300 \text{ V}^{1/2}\text{cm}^{-1/2}$. $N_{\text{all}}/N_{\text{diff}}$ values in cry-NPD and amo-NPD indicate that the repeated charge hopping in the forward and the backward directions occur in the crystal phase as well as in the amorphous phase at low electric field. At $1300 \text{ V}^{1/2}\text{cm}^{-1/2}$, declines in ΔX of each pair is observed. This indicates that the charge transport at a higher applied electric field is less dependent on particular molecular pairs. This trend is unchanged when the energetic disorder is not applied. Detailed functions of the ΔX_{\max} pair can be analyzed by examining P_{ij} . Figures 3.29a and 3.29b show the values of P_{ij} from molecule #1088, which is the target site for the ΔX_{\max} pair (#3004 - #1088) at $300 \text{ V}^{1/2}\text{cm}^{-1/2}$ with the energetic disorder. Those P_{ij} mean a subsequent hopping destination after a charge hops from #3004 to #1088. The #1088-#3223 pair itself is not in the applied field direction rather almost perpendicular direction, but P_{ij} from the molecule (#1088) to the molecule (#3223) is very high (0.99). It is very advantageous for a charge on the molecule (#1088) to

move out to the molecule #3223 without going back to the starting molecule (#3004). As a result contribution of the #3004 - #1088 pair to the charge transport increases. Figures 3.29c and 3.29d show the values of P_{ij} , starting from #864, which is the target molecule of the #2389-#864 molecular pair. When the simulation is performed under the lower applied electric field condition ($300 \text{ V}^{1/2} \text{ cm}^{-1/2}$), charges arrived at the target molecule of this pair (#864) are forced to move back to the starting molecule (#2389). This means they tend to repeat back and forth charge hopping and thus this pair has only a small contribution at $300 \text{ V}^{1/2} \text{ cm}^{-1/2}$ (Figures 3.29c). At $1300 \text{ V}^{1/2} \text{ cm}^{-1/2}$ with the energetic disorder is applied, the #2389-#864 pair has the largest ΔX (Figures 3.29d). 0.60 of P_{ij} is assigned to the charge hopping going back to the starting molecule (#2389), but the rest of that are used to move out of the #2389-#864 pair; #864 to #3645 ($P_{ij} = 0.15$) and #2078 ($P_{ij} = 0.10$) give some possibility for a charge to move out of the #2389-#864 pair. From these results, it is found that the degree of contribution of each pair can be estimated by checking the distribution of P_{ij} work to move out of that pair without being trapped. An aggregated state of which each molecule has such the distribution of P_{ij} is proposed to be an important factor for materials design to satisfy this condition for formation of successive charge-transport pathway.

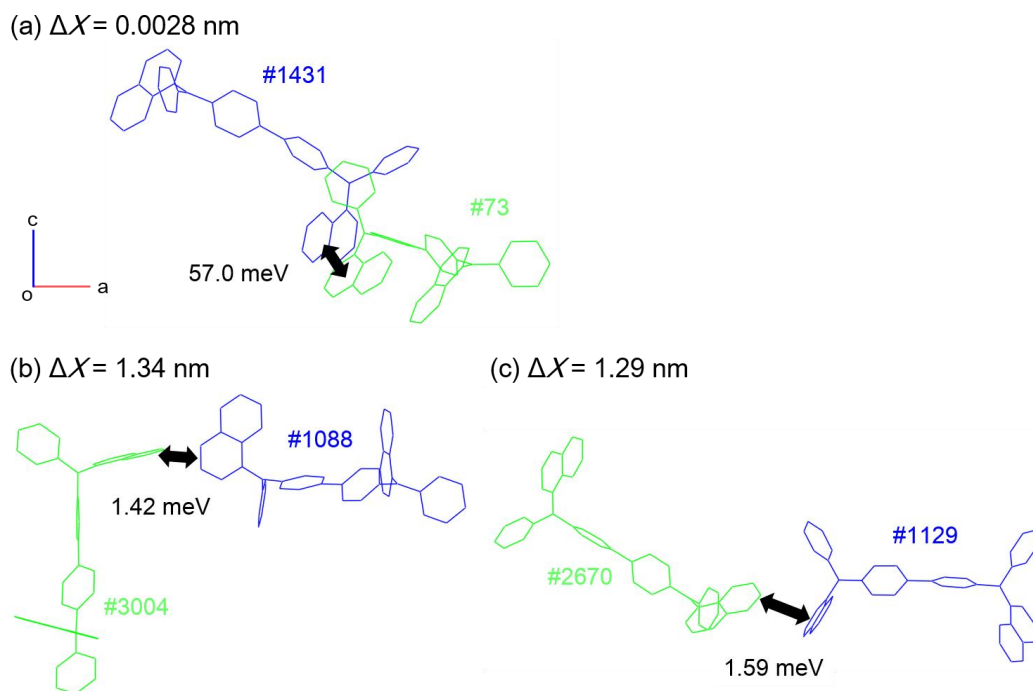


Fig. 3.25. The values of H_{ij}^- for the molecular pairs with (a) the largest H_{ij}^- , (b) the largest ΔX and (c) the second largest ΔX for electron transfer in amo-NPD along a-axis (in the same direction as the x-axis) at a $300 \text{ V}^{1/2} \text{ cm}^{-1/2}$. The energetic disorders are applied for all the calculations.

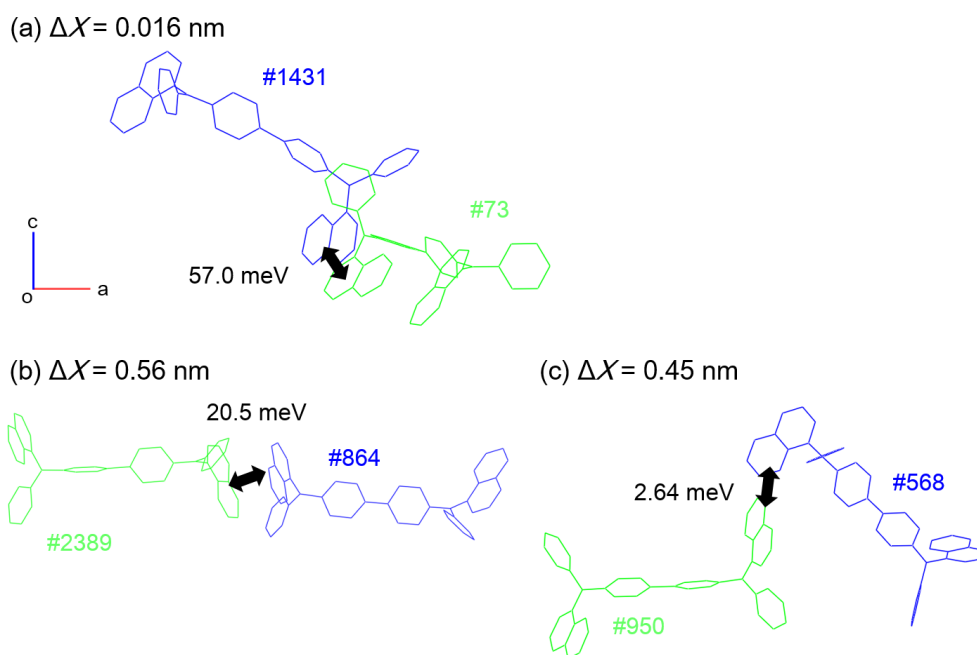


Fig. 3.26. The values of H_{ij}^- for the molecular pairs with (a) the largest H_{ij}^- , (b) the largest ΔX and (c) the second largest ΔX for electron transfer in amo-NPD along a-axis (in the same direction as the x-axis) at a $1300 \text{ V}^{1/2} \text{ cm}^{-1/2}$. The energetic disorders are applied for all the calculations.

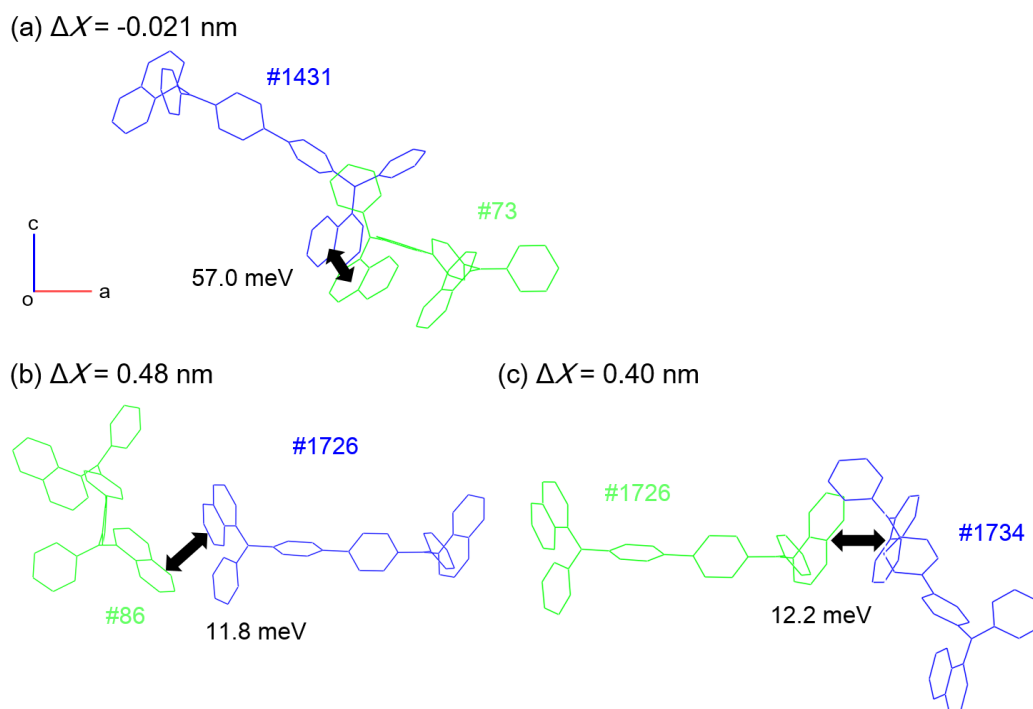


Fig. 3.27. The values of H_{ij}^- for the molecular pairs with (a) the largest H_{ij}^- , (b) the largest ΔX and (c) the second largest ΔX for electron transfer in amo-NPD along a-axis (in the same direction as the x-axis) at a $300 \text{ V}^{1/2} \text{ cm}^{-1/2}$. The energetic disorders are ignored for all the calculations.

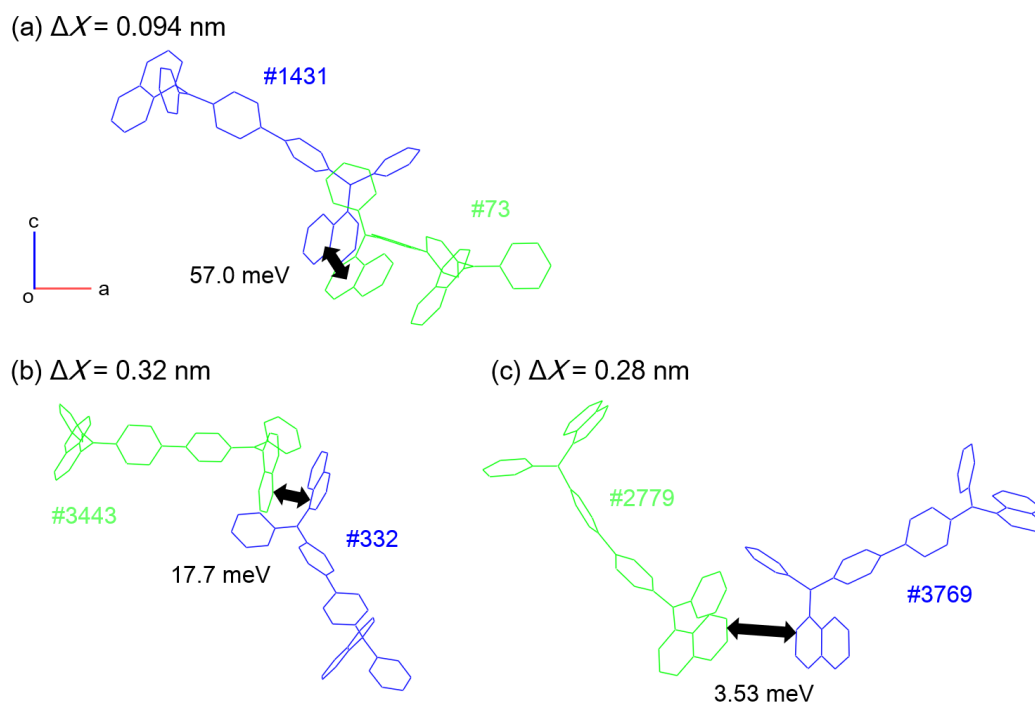
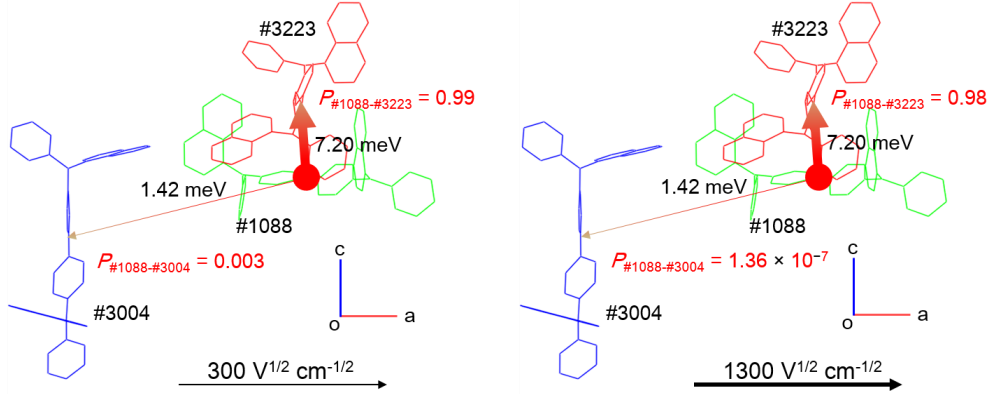


Fig. 3.28. The values of H_{ij}^- for the molecular pairs with (a) the largest H_{ij}^- , (b) the largest ΔX and (c) the second largest ΔX for electron transfer in amo-NPD along a-axis (in the same direction as the x-axis) at a $1300 \text{ V}^{1/2} \text{ cm}^{-1/2}$. The energetic disorders are ignored for all the calculations.

#3004-#1088 molecular pair
 Distribution of P_{ij} from the target molecule (#1088)
 (a) $F = 300 \text{ V}^{1/2} \text{ cm}^{-1/2}$, with e.d. ($\Delta X_{\max} = 1.34$) (b) $F = 1300 \text{ V}^{1/2} \text{ cm}^{-1/2}$, with e.d. ($\Delta X = 0.040$)



#2389-#864 molecular pair
 Distribution of P_{ij} from the target molecule (#864)
 (c) $F = 300 \text{ V}^{1/2} \text{ cm}^{-1/2}$, with e.d. ($\Delta X = 0.010$) (d) $F = 1300 \text{ V}^{1/2} \text{ cm}^{-1/2}$, with e.d. ($\Delta X_{\max} = 0.56$)

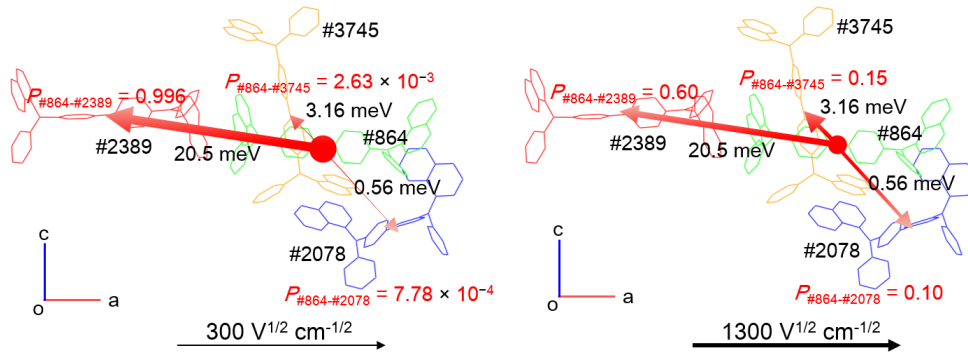


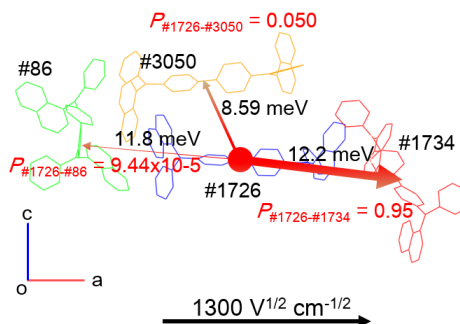
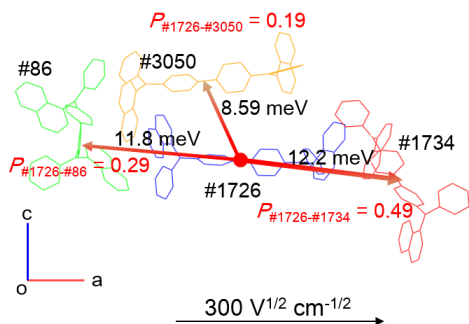
Fig. 3.29. P_{ij} for the ΔX_{\max} pair at $300 \text{ V}^{1/2} \text{ cm}^{-1/2}$ in amo-NPD along a-axis (a) at $300 \text{ V}^{1/2} \text{ cm}^{-1/2}$ and (b) at $1300 \text{ V}^{1/2} \text{ cm}^{-1/2}$. P_{ij} for the ΔX_{\max} pair at $1300 \text{ V}^{1/2} \text{ cm}^{-1/2}$ in amo-NPD along a-axis (c) at $300 \text{ V}^{1/2} \text{ cm}^{-1/2}$ and (d) at $1300 \text{ V}^{1/2} \text{ cm}^{-1/2}$. The energetic disorders are considered.

#86-#1726 molecular pair

Distribution of P_{ij} from the target molecule (#1726)

(a) $F = 300 \text{ V}^{1/2} \text{ cm}^{-1/2}$, with e.d. ($\Delta X_{\text{max}} = 0.48$)

(b) $F = 1300 \text{ V}^{1/2} \text{ cm}^{-1/2}$, with e.d. ($\Delta X = 0.12$)



#3443-#332 molecular pair

Distribution of P_{ij} from the target molecule (#332)

(c) $F = 300 \text{ V}^{1/2} \text{ cm}^{-1/2}$, with e.d. ($\Delta X = 0.089$)

(d) $F = 1300 \text{ V}^{1/2} \text{ cm}^{-1/2}$, with e.d. ($\Delta X_{\text{max}} = 0.32$)

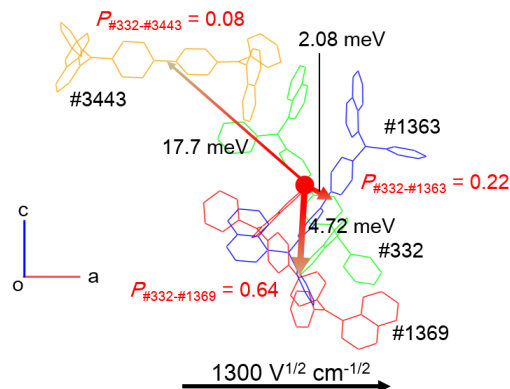
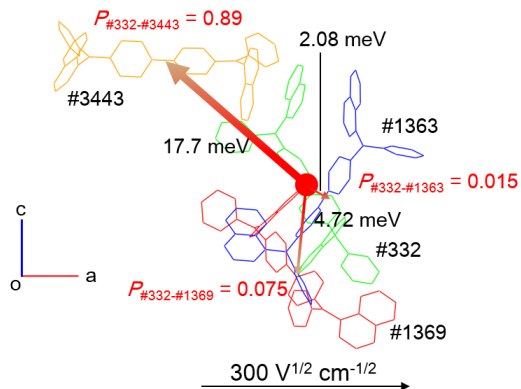


Fig. 3.30. P_{ij} for the ΔX_{max} pair at $300 \text{ V}^{1/2} \text{ cm}^{-1/2}$ in amo-NPD along a-axis (a) at $300 \text{ V}^{1/2} \text{ cm}^{-1/2}$ and (b) at $1300 \text{ V}^{1/2} \text{ cm}^{-1/2}$. P_{ij} for the ΔX_{max} pair at $1300 \text{ V}^{1/2} \text{ cm}^{-1/2}$ in amo-NPD along a-axis (c) at $300 \text{ V}^{1/2} \text{ cm}^{-1/2}$ and (d) at $1300 \text{ V}^{1/2} \text{ cm}^{-1/2}$. The energetic disorders are ignored.

3.4. Conclusion

We performed multiscale charge transport simulations to investigate the effects of energetic and especially, structural disorder on bipolar charge transport for NPD by comparing the crystal and amorphous aggregates. Calculated charge mobility and its field dependence in the amorphous thin layer were qualitatively reproduced, especially for electron transport. Both the crystal and the amorphous aggregates were found to exhibit electron transport ability as well as hole transport ability. Spatial overlap between naphthyl segments, on which the LUMO is mostly distributed, provides effective electron transport paths in the amorphous aggregates as well as in the crystals. Linear and less diffusive charge transport pathway, as well as highly anisotropic feature were observed in the crystals. They were quite different from the diffusive charge transport pathway observed in the amorphous phase. The charge transport pathways in the amorphous and crystal phase were both strongly affected by structural disorder. Energetic disorder showed a significant effect on electric field dependence regardless of the degree of the structural disorder. From the analysis of actual contribution of each molecular pair to the migration distance, we found a significant difference between crystalline and amorphous systems; charge migration is basically dominated by electronic coupling in the case of crystal, whereas it is dominated by the energetic disorder in the case of amorphous systems. These features can be understood by checking the values of P_{ij} for the charge hopping from a molecule, i , to various adjacent molecules, j . In the crystal phase, molecular pairs having large P_{ij} values are found to be quite limited and large P_{ij} values are provided for charge hoppings along the electric field direction. The repeated use of the same type of pairs with large P_{ij} values results in a relatively linear charge transport path. In the amorphous phase, it was shown that it is important for each molecular pair to have P_{ij} work to move out of that pair without being trapped, and such P_{ij} is not necessarily required to be in the direction of the applied electric field. These are proposed to be

an important factor for superior materials design of charge transport in the amorphous phase.

(Chapter 3 is the Author's version of an unsubmitted work that will be submitted for publication.)

References

- [1] V. Coropceanu, J. Cornil, D. A. da Silva Filho, Y. Olivier, R. Silbey and J. L. Bredas, *Chem. Rev.*, 107 (2007) 926.
- [2] W. D. Gill, *J. Appl. Phys.*, 43 (1972) 5033.
- [3] L. B. Schein, D. Glatz and J. C. Scott, *Phys. Rev. Lett.*, 65 (1990) 472.
- [4] H. Bässler, *Phys. Status Solidi B*, 175 (1993) 15.
- [5] R. A. Marcus and N. Sutin, *Biochim. Biophys. Acta*, 811 (1985) 265.
- [6] A. Lukyanov, C. Lennartz and D. Andrienko, *Phys. Status Solidi A*, 206 (2009) 2737.
- [7] V. Marcon, D. W. Breiby, W. Pisula, J. Dahl, J. Kirkpatrick, S. Patwardhan, F. Grozema and D. Andrienko, *J. Am. Chem. Soc.*, 131 (2009) 11426.
- [8] A. Lukyanov and D. Andrienko, *Phys. Rev. B*, 82 (2010) 193202.
- [9] T. Vehoff, B. Baumeier, A. Troisi and D. Andrienko, *J. Am. Chem. Soc.*, 132 (2010) 11702.
- [10] T. Vehoff, Y. S. Chung, K. Johnston, A. Troisi, D. Y. Yoon and D. Andrienko, *J. Phys. Chem. C*, 114 (2010) 10592.
- [11] F. May, V. Marcon, M. R. Hansen, F. Grozema and D. Andrienko, *J. Mater. Chem.*, 21 (2011) 9538.
- [12] V. Rühle, A. Lukyanov, F. May, M. Schrader, T. Vehoff, J. Kirkpatrick, B. Baumeier and D. Andrienko, *J. Chem. Theory Comput.*, 7 (2011) 3335.
- [13] B. Baumeier, F. May, C. Lennartz and D. Andrienko, *J. Mater. Chem.*, 22 (2012) 10971.
- [14] F. May, M. Al-Helwi, B. Baumeier, W. Kowalsky, E. Fuchs, C. Lennartz and D. Andrienko, *J. Am. Chem. Soc.*, 134 (2012) 13818.
- [15] C. Poelking, E. Cho, A. Malafeev, V. Ivanov, K. Kremer, C. Risko, J. L. Brédas and D. Andrienko, *J. Phys. Chem. C*, 117 (2013) 1633.
- [16] F. Suzuki, K. Shizu, H. Kawaguchi, S. Furukawa, T. Sato, K. Tanaka and H. Kaji, *J. Mater.*

Chem. C, 3 (2015) 5549.

[17] H. Uratani, S. Kubo, K. Shizu, F. Suzuki, T. Fukushima and H. Kaji, *Sci. Rep.*, 6 (2016) 39128.

[18] D. Yokoyama, *J. Mater. Chem.*, 21 (2011) 19187.

[19] J. A. Cheng and P. J. Cheng, *J. Chem. Crystallogr.*, 40 (2010) 557.

[20] Z. Deng, S. T. Lee, D. P. Webb, Y. C. Chan and W. A. Gambling, *Synth. Met.*, 107 (1999) 107.

[21] S. Naka, H. Okada, H. Onnagawa, Y. Yamaguchi and T. Tsutsui, *Synth. Met.*, 111 (2000) 331.

[22] N. D. Nguyen, M. Schmeits and H. P. Loeb, *Phys. Rev. B*, 75 (2007) 075307.

[23] C. H. Cheung, K. K. Tsung, K. C. Kwok and S. K. So, *Appl. Phys. Lett.*, 93 (2008) 083307.

[24] K. Shizu, T. Sato, K. Tanaka and H. Kaji, *Chem. Phys. Lett.*, 486 (2010) 130.

[25] B. Li, J. Chen, Y. Zhao, D. Yang and D. Ma, *Org. Electron.*, 12 (2011) 974.

[26] T. Chiba, K. I. Nakayama, Y. J. Pu, T. Nishina, M. Yokoyama and J. Kido, *Chem. Phys. Lett.*, 502 (2011) 118.

[27] T. Matsushima, K. Shiomura, S. Naka and H. Murata, *Thin Solid Films*, 520 (2012) 2283.

[28] C. Tang, H. Xu, X. L. Wang, W. Liu, R. L. Liu, Z. Rong, Q. L. Fan and W. Huang, *Thin Solid Films*, 542 (2013) 281.

[29] S. C. Tse, K. C. Kwok and S. K. So, *Appl. Phys. Lett.*, 89 (2006) 262102.

[30] S. C. Tse, K. K. Tsung and S. K. So, *Appl. Phys. Lett.*, 90 (2007) 213502.

[31] X. D. Gao, Y. He, S. T. Zhang, X. R. Yin, B. F. Ding, X. M. Ding and X. Y. Hou, *Appl. Phys. Lett.*, 95 (2009) 133306.

[32] S. Khademi, J. Y. Song, P. B. Wyatt, T. Kreouzis and W. P. Gillin, *Adv. Mater.*, 24 (2012) 2278.

[33] Y. Lou, Y. Okawa, Z. Wang, S. Naka and H. Okada, *Org. Electron.*, 14 (2013) 1015.

- [34] S. Plimpton, *J. Comput. Phys.*, 117 (1995) 1.
- [35] T. Yamada, T. Sato, K. Tanaka and H. Kaji, *Org. Electron.*, 11 (2010) 255.
- [36] T. Yamada, F. Suzuki, A. Goto, T. Sato, K. Tanaka and H. Kaji, *Org. Electron.*, 12 (2011) 169.
- [37] H. Li, L. Duan, D. Zhang and Y. Qiu, *J. Phys. Chem. C*, 118 (2014) 14848.
- [38] H. Gao, *Theor. Chem. Acc.*, 127 (2010) 759.

PART II

Development of the Methodology for Structural Refinement and Its Relation with the Emissive Property

Chapter 4

Unraveling the Origin of Blue Emission from Tris(8-hydroxyquinoline) Aluminum(III) (Alq_3) by the Combined Use of CP/MAS ^{13}C Solid-State NMR and First-Principles Calculation

4.1. Introduction

Solid-state nuclear magnetic resonance (NMR) is one of the best tools for analyzing structures of materials in solid states. So far, a variety of advanced solid-state NMR methods have been developed for the analysis of inter-nuclear distances and intersegment orientations [1-16]. In contrast, a facile cross polarization/magic-angle spinning (CP/MAS) ^{13}C experiment is a widely used technique in solid-state NMR analyses of organic materials, owing to the ease of conducting the experiments. Isotropic chemical shifts are the most important parameter in NMR, and those for all ^{13}C nuclear species are obtained simultaneously by CP/MAS ^{13}C measurements. Since isotropic chemical shifts depend on the conformation (especially torsion angles), hydrogen bonds, and intermolecular packing, CP/MAS ^{13}C experiments have been conducted to obtain such information [17, 18]. However, information obtained from CP/MAS experiments tends to be rather qualitative; as opposed to X-ray diffraction analysis, it has been difficult to precisely determine structures from results obtained by CP/MAS experiments. The isotropic chemical shifts are affected by the above-mentioned multiple factors, which often hide the origin of the change in chemical shift and make the respective analysis difficult. However, it is very attractive to obtain information on all ^{13}C nuclear species simultaneously by measurements without specific preparations, typically, isotopic labeling, which is sometimes necessary for advanced NMR spectroscopy. CP/MAS ^{13}C experiments allow powerful structural analysis of organic materials if they provide precise structural information.

One approach to obtain precise structural information from isotropic chemical shifts is the combined use of quantum chemical calculations [19]. The structural information is expected to be obtained by quantum chemical calculations of isotropic chemical shifts and comparison with experimental results. In fact, isotropic chemical shift calculations by employing the gauge-including atomic orbitals (GIAO) method [20-24] have been widely used in structural investigations. However, almost all the investigations have been for isolated molecules (molecules in gas phase). The extension to aggregated structures with intermolecular interactions, that is, to solid phases such as crystals, has been difficult and the calculations have been limited to single molecules for a long time. Under such conditions, Pickard and Mauri developed the gauge-including projector-augmented wave (GIPAW) method [25] to resolve this limitation. Employing the GIPAW method, isotropic chemical shift calculations considering intermolecular interaction have been successfully achieved using the plane-wave pseudopotential approach. Calculation of chemical shifts for isolated molecules and those for crystals are reported by the GIPAW [26-28] and a related approach [29]. The GIPAW calculations have been applied to organic molecules, and it has been shown the validity when combined with advanced solid-state NMR experiments as described in the literature [26, 27, 30-40]. In this Chapter, we demonstrate the usefulness of the combined analysis using CP/MAS measurements and GIPAW calculations for the structural refinement of organic crystals, tris(8-hydroxyquinoline) aluminum(III) (Alq_3).

Alq_3 has been a widely used material in organic light-emitting diodes since its first use by Tang and VanSlyke [41]. It has both electron transport and light-emitting properties, and normally has green luminescence. However, blue-emitting Alq_3 has also been reported [42]. The quantum yield of the blue-emitting Alq_3 is very high; almost double that of conventional Alq_3 . Investigations into the origin of the change in emission wavelength have been carried out, but the

origin is still controversial [42-62]. Alq_3 has two different isomeric states, namely *facial* and *meridional* states, as shown in Figures 4.1a and 4.1b, respectively. The three ligands in the *facial* isomer are equivalent, while one of three ligands is converted in the *meridional* isomer. Some researchers have considered that the difference of the isomeric state is the origin of the change in the emission wavelength [42-54]. In contrast, other researchers [55-58] assumed that the origin is intermolecular interaction. In refs. 59-62, definite conclusions were not drawn. Therefore, further studies are needed to reveal the origin of the blue shift, but it has been difficult to clearly distinguish between the intra- and intermolecular origins of the blue shift. The clarification of the origin of the change in emission wavelength is another purpose of this Chapter. The analysis of crystal structures is important because it provides both inter- and intramolecular information. However, there has been only one report on the crystal structure of $\gamma\text{-Alq}_3$ [46] probably owing to the difficulty of sample preparation. For $\delta\text{-Alq}_3$, the first powder wide-angle X-ray diffraction (WAXD) crystal structure analysis [42] was carried out for a sample contaminated by $\gamma\text{-Alq}_3$; it has been difficult to avoid contamination by different polymorphs [48]. The powder WAXD analysis for pure $\delta\text{-Alq}_3$ crystals was performed by the same group in the following year [59]. However, a different crystal structure was reported two years later, using $\delta\text{-Alq}_3$ single crystals [63]. Therefore, the precise and refined structure of these Alq_3 species needs to be determined to reveal the origin of blue-shift emission.

The approach taken in this Chapter does not require advanced solid-state NMR experiments, and only involves CP/MAS ^{13}C experiments, which can be easily conducted even by non-specialists in solid-state NMR. Therefore, this approach would be a robust, routine way to resolve crystal structures in detail. We ask whether precise, quantitative structural details can be obtained simply from CP/MAS experiments. Here, we show that precise structural analysis is possible by taking only a simple CP/MAS + GIPAW approach, which is almost beyond

discrimination by powder WAXD analysis. Results for more examples need to be obtained to verify the robustness of this method, but we show the successful implementation for an example in this Chapter.

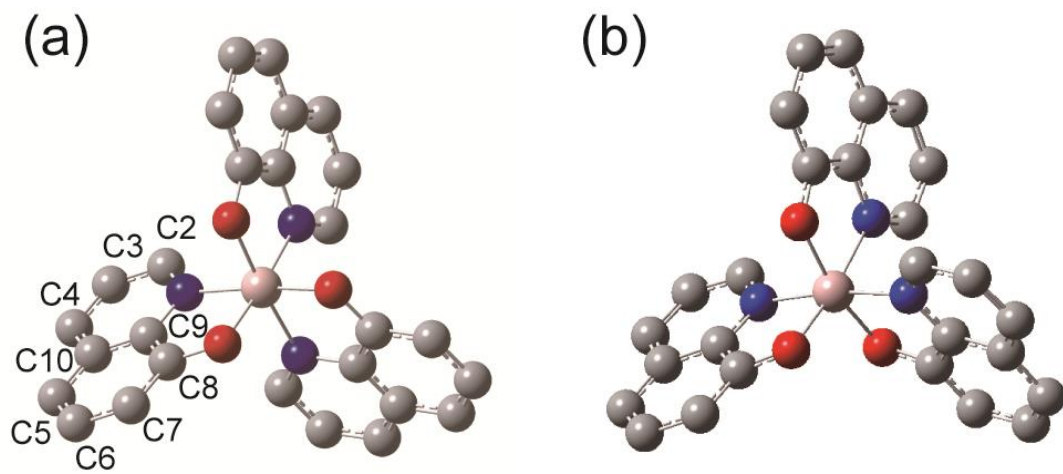


Fig. 4.1. Molecular structures of Alq₃ in (a) *facial* and (b) *meridional* isomeric states.

Hydrogen atoms are omitted for clarity.

4.2 Experimental and computational section

4.2.1. Computation

The NMR chemical shift calculations were carried out for the following crystal structures. For γ -Alq₃, three crystal structures were used in the calculations. One is the original crystal structure reported by Muccini et al. [46]. The Crystallographic Information File (CIF) includes the H coordinates as well as C, N, O, and Al coordinates, and can be used for the chemical shift calculations without modification. This original structure is denoted as “***f*- γ -M-orig**” (Figure 4.2a). In the second case, we carried out geometry optimization using *f*- γ -M-orig as an initial structure. The geometry coordinates is optimized only for H atoms with all other coordinates for Al, N, O, and C atoms being fixed (H-optimization). This crystal structure is abbreviated as “***f*- γ -M-Hopt**”. We carried out further optimization; all the atoms were optimized using the *f*- γ -M-Hopt as an initial structure (ALL-optimization). This third crystal structure is called “***f*- γ -M-ALLOpt**”.

For δ -Alq₃, two types of X-ray-analyzed crystal structures have been proposed [59, 63]. Rajeswaran et al. [63] proposed the crystal structure consisting purely of *facial* isomers with proton geometry. Firstly, we used this original structure for the chemical shift calculations without geometry optimizations. The crystal structure is abbreviated as “***f*- δ -R-orig**” (Figure 4.2b). The chemical shift calculations were carried out also for the H-optimized structure of *f*- δ -R-orig. This crystal structure is abbreviated as “***f*- δ -R-Hopt**”. The other crystal structure consisting purely of *facial* isomers was that proposed by Cölle et al. (Figure 4.2c) [59]. The CIF does not contain the H coordinates; therefore, we attached H atoms in the crystal structure and carried out H-optimization. The crystal structure is abbreviated as “***f*- δ -C-Hopt**”. Additionally, Cölle et al. reported the crystal structure of δ -Alq₃ under the assumption that it comprises entirely

of *meridional* isomers [59]. Although Cölle et al. shows this as an incorrect structure, we also carried out chemical shift calculations for the δ -Alq₃ structure consisting of *meridional* isomer. Since this crystal structure also does not contain the H coordinate, we attached Hs for the crystal and carried out H-optimization. This structure is abbreviated as “***m- δ -C-Hopt***” (Figure 4.2d). As shown in the Results and Discussion section, the agreement with experiments is better for *f- δ -C-Hopt* than for *f- δ -R-orig*, *f- δ -R-Hopt*, and *m- δ -C-Hopt*. However, even for *f- δ -C-Hopt*, the agreement is not satisfactory. Therefore, we carried out ALL-optimization for *f- δ -C-Hopt*. This crystal structure is abbreviated as “***f- δ -C-ALLOpt***”. For comparison, we also carried out ALL-optimization for *f- δ -R-Hopt* and *m- δ -C-Hopt*, which are abbreviated as “***f- δ -R-ALLOpt***” and “***m- δ -C-ALLOpt***,” respectively.

All the above geometry optimizations were carried out not for molecules in gas phase but for molecules in crystals under the periodic boundary condition using the CASTEP program (Dassault Systèmes Biovia Corp., San Diego, CA, USA). Cell parameters and space groups were kept constant for all the structures and remained original ones (δ -Alq₃: $P\bar{1}$, γ -Alq₃: $P\bar{3}$).^{46,59,63} Under the constraints, atomic coordinates are optimized; all bond lengths, bond angles, and torsion angles are treated as variables. Two Alq₃ molecules exist in one unit cell in all the original and optimized crystals. The Perdew–Burke–Ernzerhof (PBE) approximation and ultrasoft pseudopotentials with a plane-wave energy cutoff of 380 eV were used. A 2 x 2 x 4 Monkhorst-Pack *k*-point grid was used for Brillouin zone sampling for all the above crystal structures.

¹³C NMR chemical shift calculations were carried out under the periodic boundary condition by the GIPAW module implemented in NMR-CASTEP for all the above crystal structures. The PBE approximation and “On the fly” pseudopotentials were used. The energy cutoff of the plane wave was set to 610 eV. All the chemical shifts in this paper are referenced by fitting a straight

line of slope minus one to the plots of experimentally obtained chemical shifts against calculated chemical shifts [38]. A $2 \times 2 \times 4$ Monkhorst-Pack k -point grid was used for Brillouin zone sampling for all the structures. Prior to the study, we checked the validity for ALL-optimization procedure on γ -Alq₃ and for δ -Alq₃ as follows. The geometry optimization procedure can be justified by a consideration of forces acting on the atoms [38]. If these forces are reasonably small, there is little need of further geometry optimization. If the forces are considerably greater than 1.0 eV \AA^{-1} , it is reasonable to perform H-optimization. If large forces on atoms remain even after the H-optimization, the positions of heavy atom may be optimized. Table 4.1 shows the calculated forces for f - γ -M-orig, f - γ -M-Hopt, f - δ -R-orig, f - δ -R-Hopt, f - δ -C-Hopt, and m - δ -C-Hopt (in eV \AA^{-1}). For the original and H-optimized crystals (f - γ -M-orig, f - γ -M-Hopt, and f - δ -C-Hopt), the forces are greater than 1.0 eV \AA^{-1} (the maximum values are 3.69, 3.61, and 2.02 eV \AA^{-1} , respectively), indicating that these crystals are not fully appropriate structures. In contrast, all the forces are considerably smaller than 1.0 eV \AA^{-1} for the ALL-optimized crystals, as shown in Table 4.2.

To clarify the effect of intermolecular interaction, the ¹³C NMR chemical shift calculations were also carried out for isolated Alq₃ molecules extracted from respective crystals without changing the intramolecular structures. The isolated molecules are denoted by adding “IM” to the ends of the abbreviated names of respective crystal structures. For example, the isolated molecule extracted from the crystal “ f - δ -C-ALLOpt” is called “ f - δ -C-ALLOpt-IM”. To avoid differences arising through the use of different calculation methods, we use the same GIPAW method for the calculations under the same calculations conditions. GIPAW calculations always use the periodic boundary conditions; therefore, one molecule extracted from the crystal is placed in a large cubic lattice without further geometry optimization. We systematically changed the size of the cube and found that a cube with dimensions of 32 \AA is enough to neglect the effect of

intermolecular interaction on the isotropic chemical shifts. The energy cutoff of the plane wave was set to 610 eV. A 1 x 1 x 1 Monkhorst-Pack k -point grid was used for Brillouin zone sampling for the IM structures.

The powder WAXD profiles were calculated by the Mercury program (The Cambridge Crystallographic Data Centre, Cambridge, UK) [64].

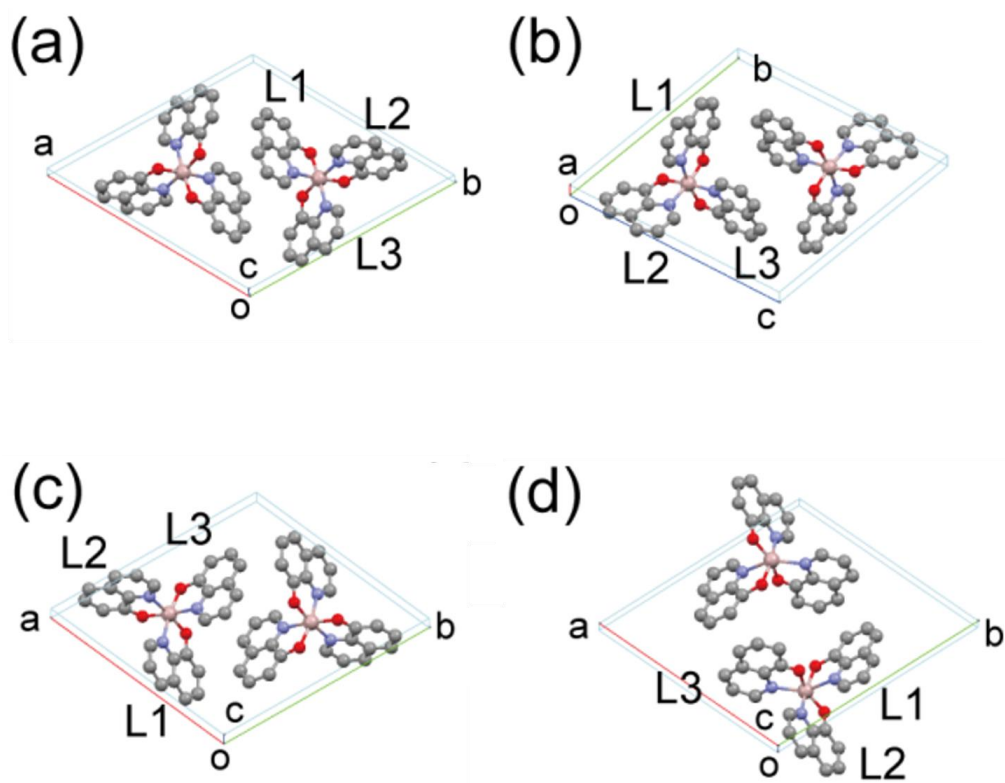


Fig. 4.2. Crystal structures of (a) γ -Alq₃ proposed by Muccini et al. [46], (b) δ -Alq₃ proposed by Rajeswaran et al. [63], (c) δ -Alq₃ proposed by Cölle et al. [59], and (d) δ -Alq₃ in *meridional* form shown by Cölle et al. [59]. All Alq₃ molecules in (a) – (c) are in *facial* form. Hydrogen atoms are omitted for clarity.

Table 4.1. Calculated forces for $f\text{-}\gamma\text{-M}\text{-orig}$, $f\text{-}\gamma\text{-M}\text{-Hopt}$, $f\text{-}\delta\text{-R}\text{-orig}$, $f\text{-}\delta\text{-R}\text{-Hopt}$, $f\text{-}\delta\text{-C}\text{-Hopt}$, and $m\text{-}\delta\text{-C}\text{-Hopt}$ (in eV \AA^{-1}). The forces acting on the atoms greater than 1.0 eV \AA^{-1} are displayed in red.

Ligand	Site	$f\text{-}\gamma\text{-M}\text{-orig}$	$f\text{-}\gamma\text{-M}\text{-Hopt}$	$f\text{-}\delta\text{-R}\text{-orig}$	$f\text{-}\delta\text{-R}\text{-Hopt}$	$f\text{-}\delta\text{-C}\text{-Hopt}$	$m\text{-}\delta\text{-C}\text{-Hopt}$
L1	C2	2.98	3.11	8.56	0.65	1.84	3.26
	C3	1.05	0.68	7.33	1.77	0.76	1.25
	C4	1.68	1.60	7.62	1.27	1.71	0.94
	C5	1.46	1.46	6.31	2.85	1.78	1.13
	C6	0.96	0.71	8.95	2.45	1.86	2.44
	C7	0.34	0.20	8.27	0.94	1.64	3.06
	C8	3.69	3.61	1.32	1.25	1.43	0.94
	C9	2.34	2.34	2.41	2.35	1.77	0.43
	C10	1.10	1.06	1.68	1.58	0.93	1.38
	L2	C2	2.98	3.11	8.96	1.81	1.36
C3		1.05	0.68	8.99	0.27	0.55	1.81
C4		1.68	1.60	8.85	1.25	1.24	1.79
C5		1.46	1.46	6.66	4.33	1.64	1.18
C6		0.96	0.71	7.97	3.17	1.96	1.07
C7		0.34	0.20	6.87	1.56	1.87	0.95
C8		3.69	3.61	0.89	0.98	1.30	2.76
C9		2.34	2.34	1.79	1.76	1.20	3.48
C10		1.10	1.06	1.58	1.59	0.43	1.39
L3		C2	2.98	3.11	7.36	1.93	1.59
	C3	1.05	0.68	6.51	2.29	0.82	1.26
	C4	1.68	1.60	8.23	3.70	1.03	3.01
	C5	1.46	1.46	8.29	3.33	0.99	2.45
	C6	0.96	0.71	6.74	3.31	1.80	2.59
	C7	0.34	0.20	8.70	0.46	1.71	1.79
	C8	3.69	3.61	1.11	1.10	2.02	2.06
	C9	2.34	2.34	0.81	0.81	1.80	1.53
	C10	1.10	1.06	1.62	1.62	0.72	1.11
	L1	H2	0.48	0.01	8.76	0.02	0.02

	H3	0.23	0.02	8.85	0.03	0.02	0.02
	H4	0.42	0.02	8.70	0.03	0.02	0.02
	H5	0.47	0.02	8.88	0.03	0.01	0.01
	H6	0.47	0.02	8.86	0.02	0.01	0.01
	H7	0.43	0.03	8.87	0.03	0.02	0.01
L2	H2	0.48	0.01	8.81	0.02	0.02	0.02
	H3	0.23	0.02	8.81	0.02	0.02	0.02
	H4	0.42	0.02	8.72	0.02	0.02	0.02
	H5	0.47	0.02	9.03	0.03	0.02	0.02
	H6	0.47	0.02	8.76	0.03	0.01	0.02
	H7	0.43	0.03	8.76	0.03	0.02	0.02
	L3	H2	0.48	0.01	8.76	0.02	0.02
H3		0.23	0.02	8.67	0.03	0.02	0.01
H4		0.42	0.02	8.92	0.03	0.02	0.02
H5		0.47	0.02	8.63	0.03	0.01	0.02
H6		0.47	0.02	8.90	0.03	0.01	0.01
H7		0.43	0.03	8.97	0.03	0.01	0.02
L1		N	0.97	0.92	0.96	0.89	0.43
L2	N	0.97	0.92	2.98	3.00	0.48	0.90
L3	N	0.97	0.92	0.99	0.94	1.17	2.16
L1	O	2.83	2.82	1.10	1.07	0.80	2.86
L2	O	2.83	2.82	1.51	1.51	0.41	1.37
L3	O	2.83	2.82	0.65	0.65	0.75	4.39
	AI	0.53	0.50	0.39	0.38	0.61	3.35

Table 4.2. Calculated forces for $f\text{-}\gamma\text{-M-ALLOpt}$, $f\text{-}\delta\text{-R-ALLOpt}$, $f\text{-}\delta\text{-C-ALLOpt}$, and $m\text{-}\delta\text{-C-}$

ALLOpt (in eV Å⁻¹).

Ligand	Site	$f\text{-}\gamma\text{-M-}$	$f\text{-}\delta\text{-R-}$	$f\text{-}\delta\text{-C-}$	$m\text{-}\delta\text{-C-}$
		ALLOpt	ALLOpt	ALLOpt	ALLOpt
L1	C2	0.01	0.21	0.25	0.24
	C3	0.20	0.07	0.12	0.10
	C4	0.11	0.07	0.10	0.11
	C5	0.10	0.07	0.09	0.10
	C6	0.11	0.07	0.11	0.10
	C7	0.28	0.09	0.12	0.12
	C8	0.26	0.10	0.29	0.30
	C9	0.11	0.18	0.20	0.20
	C10	0.11	0.02	0.01	0.02
	L2	C2	0.01	0.20	0.23
C3		0.20	0.07	0.12	0.11
C4		0.11	0.07	0.11	0.10
C5		0.10	0.07	0.10	0.12
C6		0.11	0.07	0.11	0.12
C7		0.28	0.08	0.11	0.10
C8		0.26	0.10	0.29	0.32
C9		0.11	0.18	0.20	0.20
C10		0.11	0.03	0.02	0.02
L3		C2	0.01	0.21	0.23
	C3	0.20	0.07	0.11	0.10
	C4	0.11	0.07	0.11	0.12
	C5	0.10	0.08	0.11	0.12
	C6	0.11	0.07	0.10	0.10
	C7	0.28	0.08	0.10	0.12
	C8	0.26	0.12	0.28	0.32
	C9	0.11	0.18	0.20	0.21
	C10	0.11	0.02	0.02	0.02
	L1	H2	0.02	0.06	0.02
H3		0.02	0.07	0.03	0.02
H4		0.03	0.07	0.03	0.01

	H5	0.02	0.07	0.02	0.02
	H6	0.03	0.07	0.02	0.01
	H7	0.02	0.08	0.03	0.02
L2	H2	0.02	0.06	0.02	0.02
	H3	0.02	0.07	0.02	0.01
	H4	0.03	0.07	0.03	0.01
	H5	0.02	0.07	0.02	0.02
	H6	0.03	0.08	0.02	0.02
	H7	0.02	0.08	0.02	0.02
L3	H2	0.02	0.07	0.02	0.01
	H3	0.02	0.08	0.02	0.02
	H4	0.03	0.06	0.01	0.02
	H5	0.02	0.07	0.02	0.02
	H6	0.03	0.07	0.02	0.02
	H7	0.02	0.07	0.02	0.01
L1	N	0.08	0.05	0.09	0.08
L2	N	0.08	0.05	0.08	0.09
L3	N	0.08	0.05	0.08	0.09
L1	O	0.11	0.09	0.12	0.15
L2	O	0.11	0.11	0.12	0.14
L3	O	0.11	0.11	0.13	0.13
	AI	0.06	0.04	0.06	0.04

4.2.2. Experimental

The Alq₃ sample in γ form was obtained by the thermal annealing of the sublimed Alq₃ at 407 °C for 10 s under vacuum [48]. The respective resonance lines in the CP/MAS ¹³C NMR spectrum of γ -Alq₃ are sufficiently resolved in our 400 MHz solid-state NMR. The measurement was carried out on a Chemagnetics CMX-400 Infinity spectrometer operating at a frequency of 398.76 and 100.28 MHz for ¹H and ¹³C nuclei, respectively. A double resonance probe with a 4-mm MAS probehead was used. The MAS frequency was 12.3 kHz and the contact time was 5 ms. In contrast, some of the respective resonance lines in the CP/MAS spectrum of δ -Alq₃ are overlapped. Therefore, we carried out CP/MAS experiments for δ -Alq₃ using our 800 MHz solid-state NMR. CP/MAS ¹³C NMR measurements were conducted on a Bruker Avance III spectrometer operating at a frequency of 800.15 and 201.23 MHz for ¹H and ¹³C nuclei, respectively. A double resonance probe with a 4-mm MAS probehead was used. The MAS frequency was 15 kHz and the contact time was 8 ms. To distinguish proton-attached tertiary carbons and quaternary carbons, CP/MAS NMR experiments with a short contact time of 50 μ s were also carried out. This is denoted as a “short-CP/MAS” experiment. The Alq₃ sample in δ form was obtained by thermal annealing of the sublimed Alq₃ under vacuum at 420 °C for 5 h in a vacuum-encapsulated quartz glass tube, followed by slow cooling to room temperature [65]. All ¹³C chemical shifts were expressed as values relative to tetramethylsilane (Me₄Si) using the CH₃ resonance line at 17.36 ppm for hexamethyl benzene crystals as an external reference. All the experiments throughout this work were performed at 300 K. The polymorph was identified by powder WAXD measurements on a Rigaku RINT2000 diffractometer (Tokyo, Japan) using Cu-K α radiation under the conditions of 300 mA and 40 kV. The diffraction pattern agreed with those of δ -Alq₃ as described previously [47, 48].

4.3. Results and discussion

4.3.1. Isotropic chemical shifts of γ -Alq₃.

Figure 4.3a shows the experimental CP/MAS ¹³C NMR spectrum of γ -Alq₃. The ¹³C isotropic chemical shifts of γ -Alq₃ calculated using the GIPAW approach for *f*- γ -M-orig are shown in Figure 4.3b. All the calculated chemical shift values and the difference from the experimental values for *f*- γ -M-orig, *f*- γ -M-Hopt, and *f*- γ -M-ALLOpt are summarized in Table 4.3. Compared with the experimental results in Figure 4.3a, there is relatively good agreement of the chemical shifts for C8, C3, and C5 carbons. However, there is insufficient agreement for the other carbon species; the disagreements of C2 and C10 carbons are notable (see also Table 4.3). The atomic coordinates of protons often cannot be reliably determined by WAXD analysis. Therefore, a GIPAW calculation was also performed for the H-optimized γ -Alq₃ crystals, *f*- γ -M-Hopt (Figure 4.3c). However, the result in Figure 4.3c does not show any improvement; indeed, the agreement was worse. We further performed ALL-optimization, and the result for *f*- γ -M-ALLOpt is shown in Figure 4.3d. The agreement of the calculation and the experiment was found to be excellent. Figures 4.4a-c show the experimental versus calculated isotropic chemical shifts for respective structures. The straight lines represent a perfect agreement between experiments and calculations. In general, the tolerable difference between experimental and calculated chemical shift values was 2–3 ppm [38]. The deviation from the experiment was within 1.6 ppm for all carbons for *f*- γ -M-ALLOpt (see Table 4.3). Therefore, the GIPAW-optimized crystal structure under the periodic boundary condition for all the atoms was found to be the most reliable structure for γ -Alq₃, and the crystal structure determined by WAXD analysis was refined by the combination of CP/MAS ¹³C experiments and GIPAW calculations.

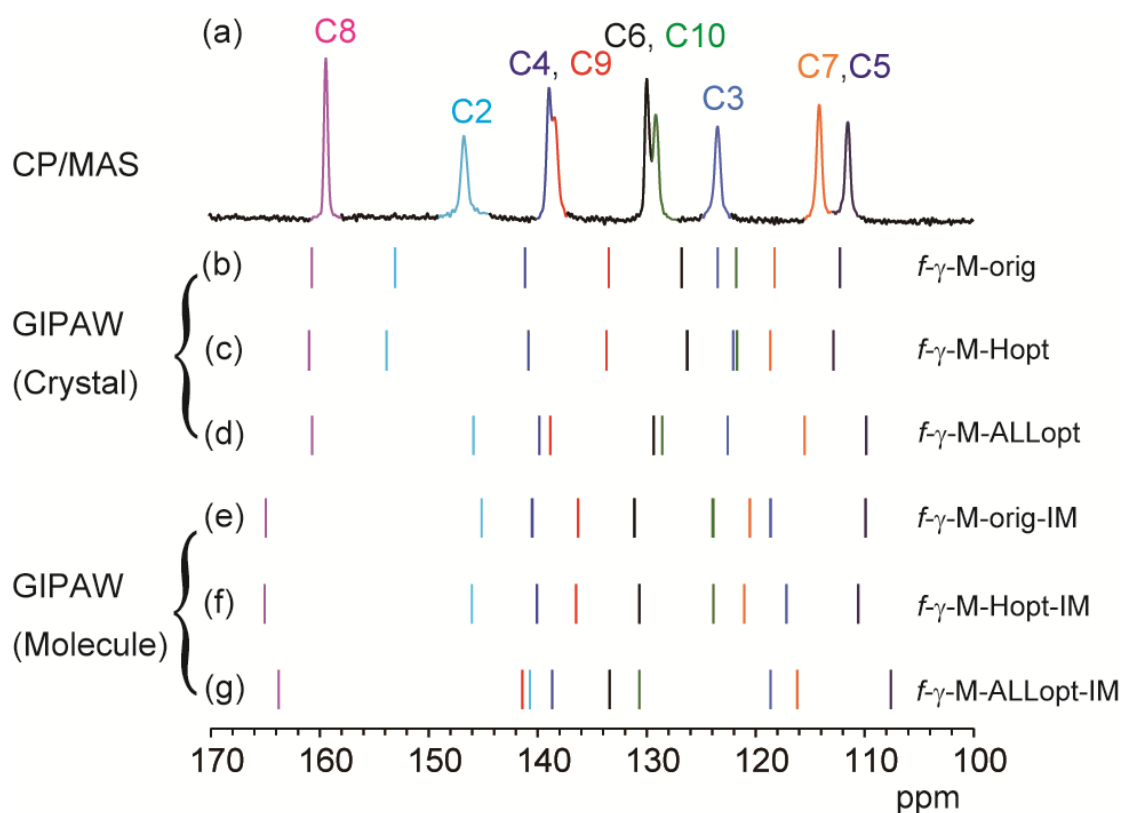


Fig. 4.3. (a) Experimental CP/MAS ^{13}C NMR spectrum of $\gamma\text{-Alq}_3$. (b)–(g) Isotropic resonance lines of $\gamma\text{-Alq}_3$ calculated using the GIPAW method. The calculations were carried out for the crystal structures (b) proposed by Muccini et al.⁴⁴ without further structural optimization ($f\text{-}\gamma\text{-M-orig}$), (c) after the optimization of the atomic coordinates for protons alone ($f\text{-}\gamma\text{-M-Hopt}$), and (d) after the optimization of the atomic coordinates for all atoms ($f\text{-}\gamma\text{-M-ALLOpt}$). Calculations of (e)–(g) were carried out for single molecules extracted from the crystal structures used for the calculations of (b)–(d), respectively.

Table 4.3. Calculated isotropic chemical shifts of *f*- γ -M-orig, *f*- γ -M-Hopt, and *f*- γ -M-ALLopt (in ppm). The differences from the experimental values are given in parentheses. The values are given in black when the differences are within 2 ppm. The other values are given in red. All of the molecules in these crystals have C_3 symmetry and the three ligands, L1, L2, and L3 (see Fig. 4.2a), provide the same isotropic chemical shifts for all carbon species.

Ligand	Site	<i>f</i> - γ -M-orig	<i>f</i> - γ -M-Hopt	<i>f</i> - γ -M-ALLopt
L1, L2, L3	C2	153.07 (+6.41)	153.74 (+7.08)	145.87 (-0.79)
	C3	123.50 (+0.10)	122.12 (-1.28)	122.54 (-0.86)
	C4	141.18 (+2.81)	140.80 (+2.43)	139.85 (+1.48)
	C5	112.28 (+0.86)	112.98 (+1.56)	109.84 (-1.58)
	C6	126.79 (-3.11)	126.33 (-3.57)	129.36 (-0.54)
	C7	118.26 (+4.21)	118.74 (+4.69)	115.50 (+1.45)
	C8	160.73 (+1.40)	160.82 (+1.49)	160.69 (+1.36)
	C9	133.48 (-5.36)	133.69 (-5.16)	138.82 (-0.02)
	C10	121.77 (-7.29)	121.78 (-7.28)	128.55 (-0.51)

To clarify the effect of intermolecular interaction, chemical shift calculations were also made without intermolecular interactions. The molecules were extracted from the respective crystals, *f*- γ -M-orig, *f*- γ -M-Hopt, and *f*- γ -M-ALLOpt, without changing the intramolecular structures. The results of the GIPAW calculations for the isolated molecules, “*f*- γ -M-orig-IM,” “*f*- γ -M-Hopt-IM,” and “*f*- γ -M-ALLOpt-IM,” are shown in Figure 4.3e–g, and in Table 4.4. Note that two molecules exist in the unit cell of the γ -Alq₃ crystals, but the structures of the two molecules are the same. The results of the GIPAW calculation for the isolated molecule, “*f*- γ -M-ALLOpt-IM,” are shown in Figures 4.3g and 4.4f (see also Table 4.4). The results clearly show that the adjacent molecules affect the isotropic chemical shifts. The chemical shift is therefore found to include information on intermolecular packing, and CP/MAS experiments can be used for the analysis.

The calculated resonance lines of the isolated Alq₃ molecules (Figure 4.3e–g) do not split into three and there is only one single resonance line for the respective carbon species. This shows that the Alq₃ molecules in the γ -Alq₃ crystals are in *facial* form where the three ligands attached to an Alq₃ molecule are equivalent and possesses C_3 symmetry. Figure 4.3b–d (and the experimental spectrum in Figure 4.3a) also shows single resonance lines for respective carbon species. The resonance lines do not split even by the intermolecular packing, such as ligand π – π stacking, as well as the intramolecular interaction. Figure 4.5a shows overwriting of the crystal structures with 0°, 120°, and 240° rotations about the C_3 axis of a molecule, which is parallel to the c-axis of *f*- γ -M-ALLOpt. The three patterns completely overlap, showing that *f*- γ -M-ALLOpt has a three-fold axis including intermolecular packing (the *f*- γ -M-ALLOpt crystal possesses $\overline{P3}$ symmetry). Therefore, the three ligands of one Alq₃ molecule have the same intermolecular interaction, which results in the appearance of single resonance lines for respective carbon species as shown experimentally in Figure 4.3a.

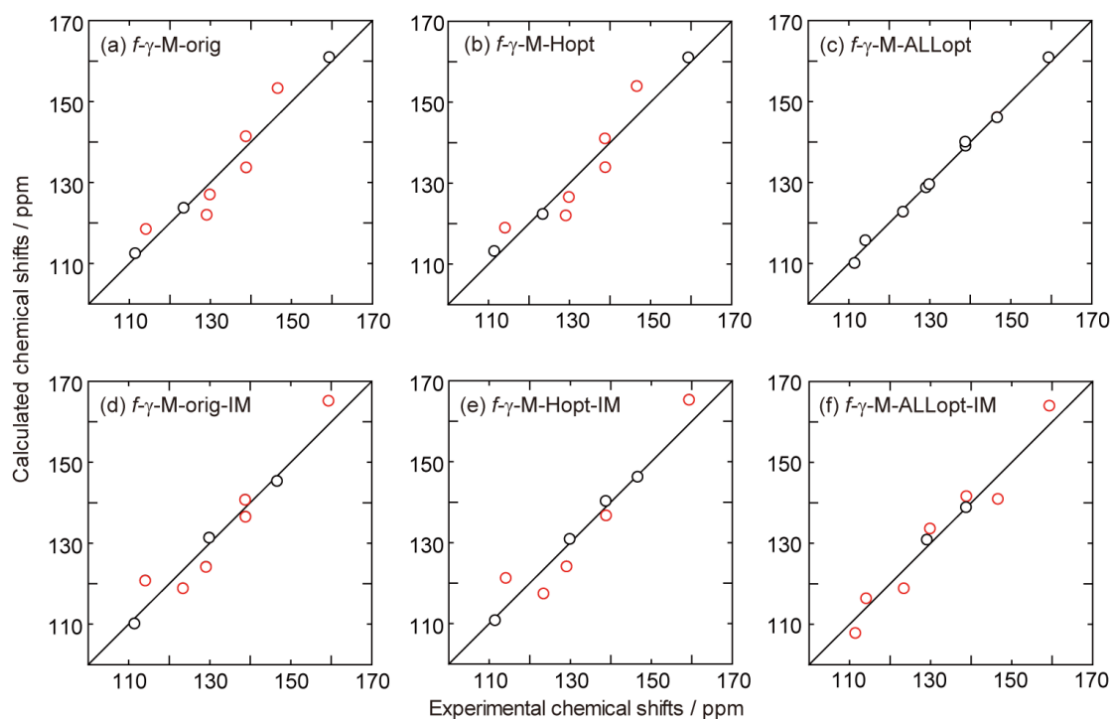


Fig. 4.4. Experimental versus calculated isotropic ^{13}C chemical shifts for (a) $f\text{-}\gamma\text{-M}\text{-orig}$, (b) $f\text{-}\gamma\text{-M}\text{-Hopt}$, (c) $f\text{-}\gamma\text{-M}\text{-ALLOpt}$, (d) $f\text{-}\gamma\text{-M}\text{-orig}\text{-IM}$, (e) $f\text{-}\gamma\text{-M}\text{-Hopt}\text{-IM}$, and (f) $f\text{-}\gamma\text{-M}\text{-ALLOpt}\text{-IM}$. The straight line represents a perfect agreement between calculations and experiments. \circ : The difference between experimental and calculated values is within 2 ppm, \circ : beyond 2 ppm.

Table 4.4. Calculated isotropic chemical shifts of *f*- γ -M-orig-IM, *f*- γ -M-Hopt-IM, and *f*- γ -M-ALLOpt-IM (in ppm). The differences from the experimental values are given in parentheses. The values are given in black when the differences are within 2 ppm. The other values are given in red.

Ligand	Site	<i>f</i> - γ -M-orig-IM	<i>f</i> - γ -M-Hopt-IM	<i>f</i> - γ -M-ALLOpt-IM
	C2	145.15 (-1.51)	146.04 (-0.62)	140.73 (-5.93)
	C3	118.65 (-4.75)	117.17 (-6.23)	118.64 (-4.76)
	C4	140.53 (+2.16)	140.06 (+1.69)	138.67 (+0.30)
	C5	109.94 (-1.48)	110.58 (-0.84)	107.59 (-3.84)
L1, L2, L3	C6	131.14 (+1.24)	130.66 (+0.76)	133.42 (+3.52)
	C7	120.54 (+6.49)	121.04 (+6.99)	116.17 (+2.11)
	C8	164.95 (+5.62)	165.07 (+5.74)	163.76 (+4.43)
	C9	136.32 (-2.53)	136.48 (-2.36)	141.40 (+2.55)
	C10	123.94 (-5.12)	123.89 (-5.17)	130.67 (+1.61)

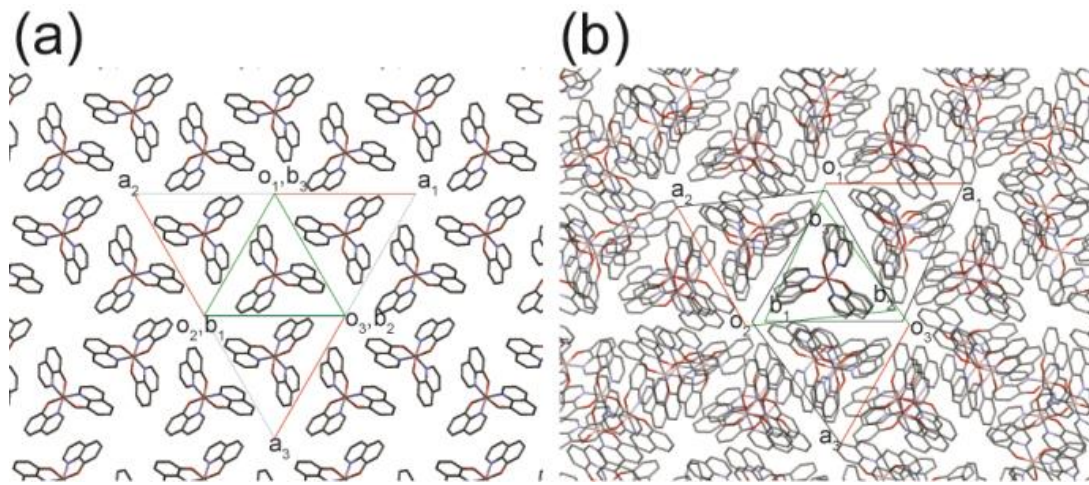


Fig. 4.5. Overwriting of the crystal structures with 0° , 120° , and 240° rotations about the axis through an Al atom parallel to the c axis of (a) $f\text{-}\gamma\text{-M-ALLOpt}$ and (b) $f\text{-}\delta\text{-C-ALLOpt}$.

4.3.2. Isotropic chemical shifts of δ -Alq₃.

At the top of Figure 4.6a, we show the experimental CP/MAS ¹³C NMR spectrum of δ -Alq₃. In the spectrum, the resonance lines of C8, C2, and C3 carbons are well separated from the other carbon resonance lines. However, the C4 and C9 carbons, the C6 and C10 carbons, and the C7 and C5 carbons overlap and the chemical shifts are ambiguous. The C4 carbon is a tertiary carbon, which possesses one directly bonded proton. In contrast, the C9 carbon is quaternary and does not have directly bonded protons. In CP/MAS NMR experiments, the polarizations are transferred from ¹H to ¹³C during the contact time in the CP process. For the CP/MAS experiments at the top of Figure 4.6a, the contact time was set to 8 ms and polarizations were transferred from ¹H to all ¹³C species irrespective of the number of directly bonded protons. In contrast, the polarizations can be transferred selectively from ¹H to directly bonded ¹³C using only a short contact time; the resonance lines for quaternary carbons then disappear. Therefore, we can distinguish tertiary carbons and quaternary carbons by shortening the contact time. The experimentally obtained CP/MAS ¹³C NMR spectra with contact times of 50 μ s are shown at the middle of Figure 4.6a. In the middle short-CP/MAS spectrum, quaternary C8 resonance lines disappear and tertiary C2 and C3 carbons are observed. This result clearly shows that we can distinguish tertiary carbons and quaternary carbons. Additionally, the difference between the two experimental spectra is shown at the bottom of Figure 4.6a. This is the spectrum for quaternary carbons. From these spectra, the isotropic chemical shifts of C4 and C9 carbons are distinguished. The same is true for those of the C6 and C10 carbons. In contrast, the C7 and C5 carbons, both of which are tertiary, cannot be separated and the chemical shifts are ambiguous. Therefore, the experimental chemical shifts of the C7 and C5 carbons are not used for further detailed analysis.

All chemical shift values are also given in Tables 4.5 and 4.6. In the Tables 4.5 and 4.6, the differences from the experimental values are also shown. The values are given in black when the differences are within a tolerance level of 2 ppm. The other values are given in red. The three ligands of Alq_3 are denoted by L1, L2, and L3 in Figure 4.2. As described in the Introduction, two types of crystal structures have been proposed for $\delta\text{-Alq}_3$; by Cölle et al. [59] and by Rajeswaran et al. [63]. Similarly with the case of $\gamma\text{-Alq}_3$, the GIPAW-calculated chemical shifts for the original structures and H-optimized structures do not match the experimental results for both the proposed structures (Figure 4.6b-2.6e and Tables 4.5). The information for proton coordinates is not included for the other crystal structure reported by Cölle et al. [59] and we cannot present the results of the chemical-shift calculations without structure optimization for Cölle's structure. The chemical shifts calculated for the structure $f\text{-}\delta\text{-R}\text{-orig}$ in Figure 4.6b obviously deviate from the experimental values. The proton-optimized structure, $f\text{-}\delta\text{-R}\text{-Hopt}$, in Figure 4.6c shows better results, but the calculated chemical shifts still do not match the experimental results well (see also Table 4.5). In Figure 4.6d and 4.6e, we show the GIPAW-calculated chemical shifts for Cölle's $\delta\text{-Alq}_3$ crystals with H-optimization under the assumption that the Alq_3 molecules are exclusively in *meridional* and *facial* isomers ($m\text{-}\delta\text{-C}\text{-Hopt}$ and $f\text{-}\delta\text{-C}\text{-Hopt}$), respectively. The calculated chemical shifts for $m\text{-}\delta\text{-C}\text{-Hopt}$ with *meridional* isomers (Figure 4.6d) significantly differ from the experimental results. Figure 4.7 shows the experimental versus calculated isotropic chemical shifts for respective structures. Compared with the chemical shifts for $f\text{-}\delta\text{-R}\text{-orig}$ (Figure 4.7a), $f\text{-}\delta\text{-R}\text{-Hopt}$ (Figure 4.7b), and $m\text{-}\delta\text{-C}\text{-Hopt}$ (Figure 4.7c), the chemical shifts for the $f\text{-}\delta\text{-C}\text{-Hopt}$ (Figure 4.7d) structure more closely match the experimental results. For the $f\text{-}\delta\text{-C}\text{-Hopt}$ structure, the deviation is within 3 ppm for the C2, C3, C4, C8, and C10 carbons (see Table 4.5). However, the deviation is beyond a tolerable level

for C6 and C9 carbons and the maximum deviation is 7.72 ppm. Therefore, further investigation was carried out using the structure reported by Cölle et al. [59] with *facial* isomers.

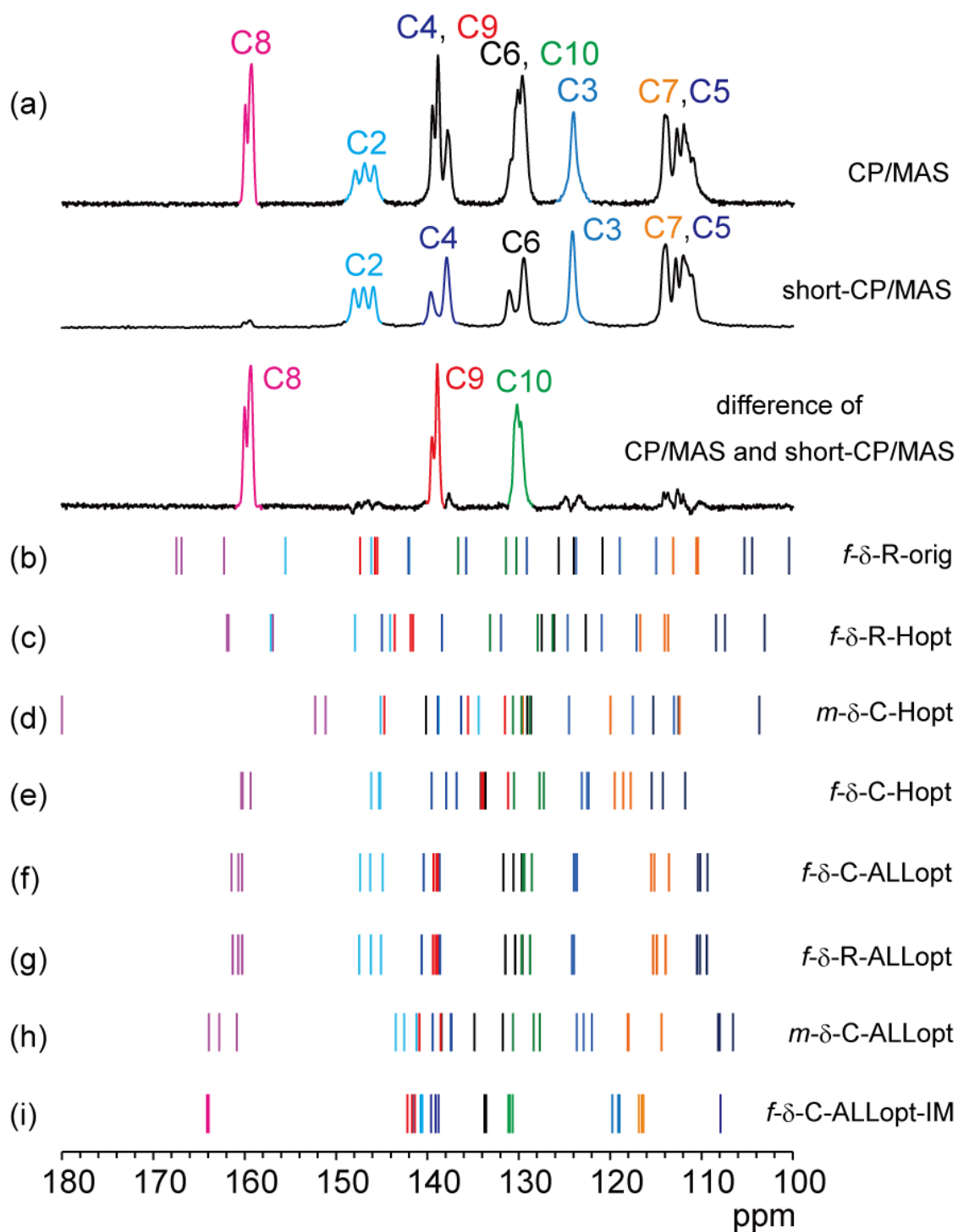


Fig. 4.6. (a) Experimental CP/MAS, short-CP/MAS, and the difference spectra of δ -Alq₃. (b)–(i) Isotropic resonance lines of δ -Alq₃ calculated using the GIPAW method. The calculations were carried out for the crystal structures (b) proposed by Rajeswaran et al. without structural optimization (*f*- δ -R-orig), (c) after the optimization only for protons (*f*- δ -R-Hopt), (d) provided by Cölle et al. under the assumption that all molecules are meridional isomers after the optimization only for protons (*m*- δ -C-Hopt), (e) proposed by Cölle et al. after the optimization of the atomic coordinates only for protons (*f*- δ -C-Hopt), (f) proposed by Cölle et al.⁵⁹ after the optimization of the atomic coordinates for all atoms (*f*- δ -C-ALLOpt), (g) proposed by Rajeswaran et al.⁶³ after the optimization of the atomic coordinates for all atoms (*f*- δ -R-ALLOpt). Calculation of (h) was carried out for the crystal structure reported by Cölle et al.⁵⁹ consisting entirely of *meridional* isomer after the optimization of the atomic coordinates for all atoms (*m*- δ -C-ALLOpt). Calculation of (i) was carried out for single molecules extracted from the crystal structure used for the calculations of (f). All Alq₃ molecules in (b), (c), (e), (f), (g) and (i) are in *facial* form.

Table 4.5. Calculated isotropic chemical shifts for f - δ -R-orig, f - δ -R-Hopt, m - δ -C-Hopt and f - δ -C-Hopt (in ppm). The differences from the experimental values are given in parentheses. The values are given in black when the differences are within 2 ppm. The other values are given in red. The definitions of ligand L1, L2, and L3 are given in Fig. 4.2b. The chemical shift references, σ_{ref} , are also shown at the bottom.

Ligand	Site	f - δ -R-orig	f - δ -R-Hopt	m - δ -C-Hopt	f - δ -C-Hopt
L1	C2	146.16 (-0.76)	147.94 (+1.02)	145.11 (-1.81)	145.17 (-1.75)
	C3	118.96 (-5.10)	120.96 (-3.10)	117.62 (-6.44)	123.14 (-0.92)
	C4	129.15 (-8.71)	131.98 (-5.88)	129.66 (-8.20)	137.96 (+0.10)
	C6	125.64 (-5.43)	127.52 (-3.55)	129.12 (-0.31)	133.66 (+4.23)
	C8	162.30	156.93 (-2.39)	179.89 (+20.6)	159.39 (+0.07)
	C9	147.40	143.60 (+4.11)	144.72 (+5.80)	134.11 (-4.81)
	C10	130.28	126.33 (-3.38)	128.82 (-1.38)	130.53 (+0.33)
L2	C2	155.56	157.16 (+9.18)	134.42 (-13.6)	146.16 (-1.82)
	C3	123.72 (-0.34)	124.68 (+0.62)	113.13 (-10.9)	122.38 (-1.68)
	C4	142.07	145.00 (+5.38)	136.34 (-3.28)	139.58 (-0.04)
	C6	120.85 (-8.58)	122.69 (-6.74)	128.71 (-2.36)	134.19 (-3.12)
	C8	167.51	161.96 (+1.96)	151.14 (-8.86)	160.26 (+0.26)
	C9	145.75	141.84 (+2.92)	131.55 (-7.94)	133.93 (-5.56)
	C10	131.43	127.96 (-1.75)	130.68 (+0.48)	127.29 (-2.91)
L3	C2	142.01 (-3.89)	144.11 (-1.79)	138.76 (-7.14)	145.33 (-0.57)
	C3	114.98 (-9.08)	117.15 (-6.91)	124.58 (+0.52)	122.55 (-1.51)
	C4	135.77 (-3.85)	138.42 (-1.20)	138.90 (+1.04)	136.82 (-1.04)
	C6	124.00 (-7.07)	126.15 (-4.92)	140.18 (+9.11)	133.71 (2.64)
	C8	166.92	161.79 (+1.79)	152.25 (-7.07)	160.39 (1.07)
	C9	145.48	141.62 (+2.70)	135.59 (-3.33)	131.20 (-7.72)
	C10	136.65	133.17 (+3.15)	129.77 (-0.01)	127.75 (-2.03)
σ_{ref}		175.24	170.73	175.24	164.51

Table 4.6. Calculated isotropic chemical shifts for *f*- δ -R-ALLOpt, *m*- δ -C-ALLOpt and *f*- δ -C-ALLOpt (in ppm). The differences from the experimental values are given in parentheses. The values are given in black when the differences are within 2 ppm. The other values are given in red. The definitions of ligand L1, L2, and L3 are given in Figs. 4.2c and 4.2d. The chemical shift references, σ_{ref} , are also shown at the bottom.

Ligand	Site	<i>f</i> - δ -R-ALLOpt	<i>m</i> - δ -C-ALLOpt	<i>f</i> - δ -C-ALLOpt
L1	C2	146.21 (-0.71)	142.51 (-4.41)	146.33 (-0.59)
	C3	123.90 (-0.16)	122.92(-1.14)	123.67 (-0.39)
	C4	138.61 (+0.75)	137.44 (-0.42)	138.73 (+0.87)
	C6	129.57 (-1.50)	134.86 (+5.43)	129.74 (+0.31)
	C8	160.76 (+1.44)	163.80 (+4.48)	160.77 (+1.45)
	C9	138.86 (-0.63)	140.86 (+1.94)	138.90 (-0.02)
	C10	129.61 (-0.10)	127.74 (-2.46)	129.44 (-0.76)
L2	C2	147.48 (-0.50)	143.43 (-4.55)	147.44 (-0.54)
	C3	123.93 (-0.13)	122.05 (-2.01)	124.03 (-0.03)
	C4	140.63 (+1.01)	139.38 (-0.24)	140.47 (+0.85)
	C6	130.38 (+0.95)	131.73 (+0.66)	130.66 (-0.41)
	C8	161.38 (+1.38)	160.75 (+0.75)	161.54 (+1.54)
	C9	139.37 (+0.45)	138.53 (-0.96)	139.41 (-0.08)
	C10	129.67 (-0.04)	128.38 (-1.82)	129.63 (-0.57)
L3	C2	145.07 (-0.83)	141.18 (-4.72)	144.97 (-0.93)
	C3	124.12 (+0.06)	123.67 (-0.39)	123.82 (-0.24)
	C4	138.92 (-0.70)	137.36 (-0.50)	139.06 (+1.20)
	C6	131.43 (+0.36)	138.45 (+7.38)	131.76 (+0.69)
	C8	160.32 (+0.32)	162.69(+3.37)	160.36 (+1.04)
	C9	139.05 (+0.13)	140.88 (+1.96)	139.08 (+0.16)
	C10	128.71 (-1.31)	130.64 (+0.86)	128.62 (-1.16)
σ_{ref}		170.48	170.73	170.19

We also show the GIPAW-calculated ^{13}C isotropic chemical shifts only for ALL-optimized crystals in Figure 4.6f-i. The GIPAW calculation for ALL-optimized crystals for Cölle's $\delta\text{-Alq}_3$ composed entirely of *facial* isomers, *f*- $\delta\text{-C-ALLOpt}$, in Figure 4.6f excellently reproduces the resonance line splittings for respective carbon species. Experimentally, the intensity of the upfield resonance line of the C8 carbon is stronger than that of the downfield one. This is explained by the GIPAW calculation in Figure 4.6f that the calculated two resonance lines mostly overlap on the upfield side. The three equally spaced C2 resonance lines and mostly single C3 resonance lines are excellently reproduced as shown in Figure 4.6f. Including these resonance line splitting patterns, the agreement between the calculations for *f*- $\delta\text{-C-ALLOpt}$ and the experiment is satisfactory, as shown in Figure 4.7e. The calculated chemical shifts agree with the experimental chemical shifts within 1.54 ppm (see in the rightmost column of Table 4.6). Therefore, it is found that the ALL-optimized structure is most reliable structure also for $\delta\text{-Alq}_3$. The H-optimized Rajeswaran's structure, *f*- $\delta\text{-R-Hopt}$, and H-optimized Cölle's structure, *f*- $\delta\text{-C-Hopt}$, provide different GIPAW-calculated chemical shifts, reflecting the different crystal structures (Figure 4.6c and 4.6e). However, the calculated chemical shifts for ALL-optimized Cölle's structure (Figure 4.6f) and those for ALL-optimized Rajeswaran's structure (Figure 4.6g) both in the *facial* form are found to become almost indistinguishable after ALL-optimizations (See also Figures 4.7e and 4.7f). The deviation from the experiment is within 1.50 ppm for *f*- $\delta\text{-R-ALLOpt}$. The results show that both the proposed structures converge on similar refined structures after the optimization of the atomic coordinates for all atoms.

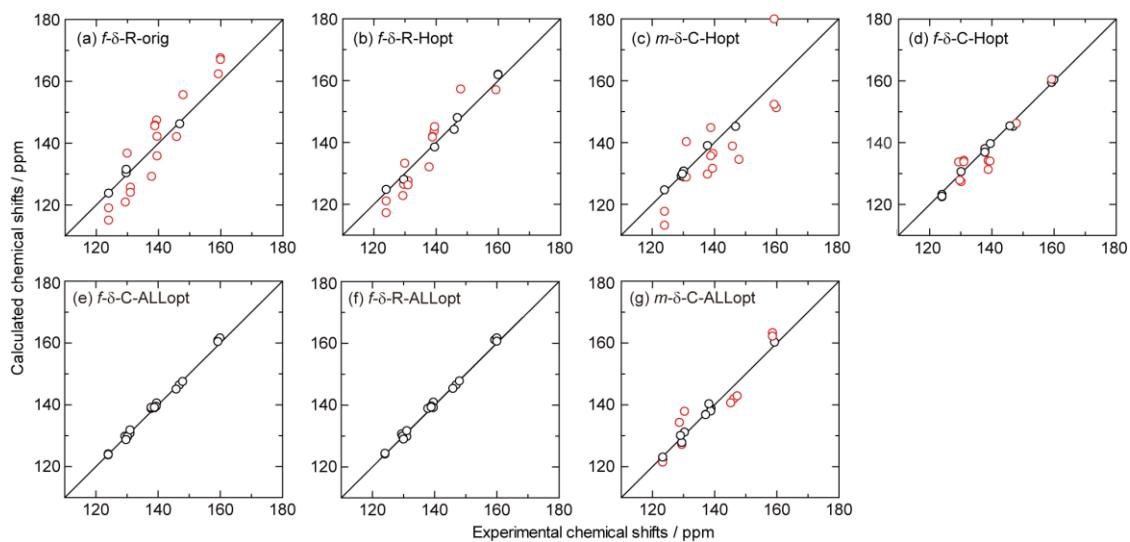


Fig. 4.7. Experimental versus calculated isotropic ^{13}C chemical shifts for (a) $f\text{-}\delta\text{-R-orig}$, (b) $f\text{-}\delta\text{-R-Hopt}$, (c) $m\text{-}\delta\text{-C-Hopt}$, (d) $f\text{-}\delta\text{-C-Hopt}$, (e) $f\text{-}\delta\text{-C-ALLOpt}$, (f) $f\text{-}\delta\text{-R-ALLOpt}$ and (g) $m\text{-}\delta\text{-C-ALLOpt}$. The straight line represents a perfect agreement between calculations and experiments. \circ : the difference between experimental and calculated values is within 2 ppm, \circ : beyond 2 ppm.

Figure 4.6h shows the calculated chemical shifts for the ALL-optimized δ -Alq₃ structure consisting of *meridional* isomers, *m*- δ -C-ALLOpt. The result significantly deviates from the experimental chemical shifts (see also Figure 4.7g). The results clearly show that the δ -Alq₃ is composed of *facial* isomers, not of *meridional* isomers. The resonance line splitting observed in CP/MAS ¹³C NMR spectrum of δ -Alq₃ is considered to originate from the intermolecular interaction.

The chemical shift calculations for molecules in δ -Alq₃ in the isolated state are important in revealing the origin of the resonance line splitting for respective carbon species. The GIPAW-calculated chemical shifts for the isolated molecule, *f*- δ -C-ALLOpt-IM, which is extracted from the *f*- δ -C-ALLOpt crystals, are shown in Figure 4.6i. The calculated chemical shifts in the isolated state differ from those in the crystal packing (Figure 4.6f), indicating the effect of intermolecular interaction in δ -form crystals on the isotropic chemical shifts. Although the resonance line splittings are found for *f*- δ -C-ALLOpt in Figure 4.6f, the resonance lines for respective carbon species coalesce into a single resonance line or show smaller splitting for the *f*- δ -C-ALLOpt-IM in Figure 4.6i. The results show that the Alq₃ molecules in the refined crystal structure, *f*- δ -C-ALLOpt, are in the *facial* isomeric state with not complete but nearly complete C₃ symmetry. Therefore, the resonance line splitting observed in the experimental CP/MAS ¹³C NMR spectrum (Figure 4.6a) is found to originate from the intermolecular interaction. Figure 4.5b shows overwriting of the crystal structures with 0°, 120°, and 240° rotations about the C₃ axis of a molecule, which is parallel to the c-axis of *f*- δ -C-ALLOpt. As opposed to the case of γ -Alq₃ in Figure 4.5a, the three structures do not completely overlap. This indicates that the δ -Alq₃ crystals do not have a threefold axis, although the molecule has near-C₃ symmetry. The three ligands of Alq₃ crystals have different intermolecular interactions.

Both γ - and δ -Alq₃ emit blue luminescence with a maximum wavelength of 466–470 nm [47, 48, 58, 60, 61] which differs from the normal green luminescence of Alq₃ with a maximum wavelength of 504–541 nm [47, 48, 55, 60, 61]. As described in the Introduction, the origin of the different fluorescence properties has not been well established. Our analysis conducting CP/MAS ¹³C NMR experiments and GIPAW calculations clearly shows that both the γ - and δ -Alq₃ are in the *facial* isomeric state with different intermolecular interaction. Figure 4.8 directly compares the chemical shifts of the isolated Alq₃ molecules (without intermolecular interaction) extracted from the refined crystal structures of γ - and δ -Alq₃, *f*- γ -M-ALLOpt, and *f*- δ -C-ALLOpt. These patterns mostly agree with each other, indicating that the intramolecular structures of Alq₃ in the γ - and δ -Alq₃ crystals are basically the same. The difference between the experimental CP/MAS ¹³C NMR spectra of γ - and δ -Alq₃ crystals provides clear evidence of the difference in the intermolecular interaction. The γ - and δ -Alq₃ crystals in this study have similar PL spectra with maximum wavelengths of 470 and 468 nm, respectively, in spite of the clear difference between the intermolecular interactions of the γ - and δ -Alq₃ crystals as clarified by CP/MAS ¹³C NMR measurements. The difference in the intermolecular interaction in γ - and δ -Alq₃ crystals has a negligible impact on the emission wavelength.

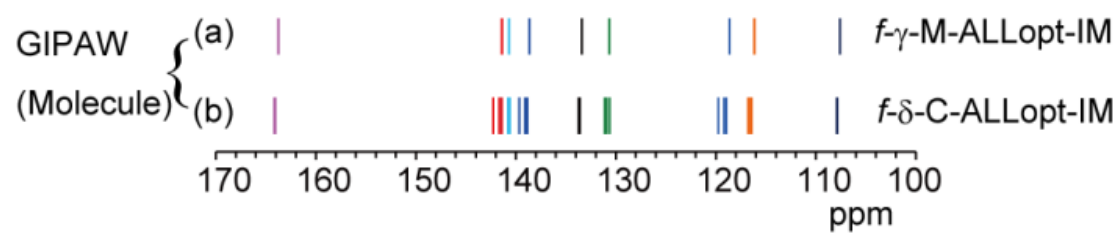


Fig. 4.8. GIPAW-calculated isotropic resonance lines for the structures (a) $f\text{-}\gamma\text{-M-ALLOpt-IM}$ and (b) $f\text{-}\delta\text{-C-ALLOpt-IM}$.

The ALL-optimized structures consisting of *facial* isomers (*f*- γ -M-ALLOpt, *f*- δ -C-ALLOpt, and *f*- δ -R-ALLOpt) are found to be the most refined crystal structures in both of γ -Alq₃ and δ -Alq₃. By comparing the data for isolated molecules and those for molecules in the most refined crystals, it was found that the agreement between the experiments and calculations is significantly improved by introducing intermolecular interactions in the crystals.

Finally, powder WAXD profiles reproduced from the original and GIPAW-optimized crystal structures are shown in Figures 4.9 and 4.10 for γ - and δ -Alq₃, respectively. For γ -Alq₃ (Figure 4.9), all the patterns look similar. The patterns for δ -Alq₃ in Figure 4.10 also look similar (except for *m*- δ -C-ALLOpt, as described below). The results show that powder WAXD profiles of the structures composed of *facial* isomers do not show a clear difference for the structural changes by H-optimization and ALL-optimization (the atomic coordinate changes are shown in Figure 4.11). It is also found that the difference between the structure obtained by Rajeswaran et al. [63] and that obtained by Cölle et al. [59] is difficult to distinguish through powder WAXD experiments. Therefore, two different crystal structures have been proposed. Although the distinction between *meridional* and *facial* isomers is important, the pattern composed purely of *facial* isomers and that composed purely of *meridional* isomers do not show a significant difference for H-optimized structures (Figure 4.10c and 4.10e). An exception is the ALL-optimized structure composed of *meridional* isomers, *m*- δ -C-ALLOpt, in Figure 4.10f. In this case, diffraction intensities change by ALL-optimization procedure, although the diffraction angles remain the same. To put it the other way around, crystal structures composed of *meridional* isomers can provide X-ray diffraction patterns similar to those of *facial* isomers by manipulating the atomic coordinates without changing the isomeric state, as shown in Figure 4.10e. This indicates the difficulty of the distinction between *meridional* and *facial* isomeric states by powder WAXD measurements. In some cases, the coexistence of *meridional* and

facial isomers should be considered, but the analysis is also difficult only by powder WAXD measurements. In contrast, CP/MAS NMR spectra provide clearly different patterns for the different isometric states as shown in Figures 4.5a and 4.5b. Our analysis found that neither γ - nor δ -Alq₃ contains *meridional* isomers and they are composed exclusively of *facial* isomers. The combination of simple CP/MAS ¹³C NMR experiments and GIPAW calculations (optimizations and chemical-shift calculations) can be easily employed as a structural refinement method. Currently, iterative analysis is nearly impossible owing to the limitation of computation time. It is currently necessary to use adequate initial crystal structures; i.e., the X-ray-determined structures in this study. However, precise structural analysis is expected to become possible through only simple CP/MAS (or MAS) NMR experiments and GIPAW calculations with a future increase in calculation speed.

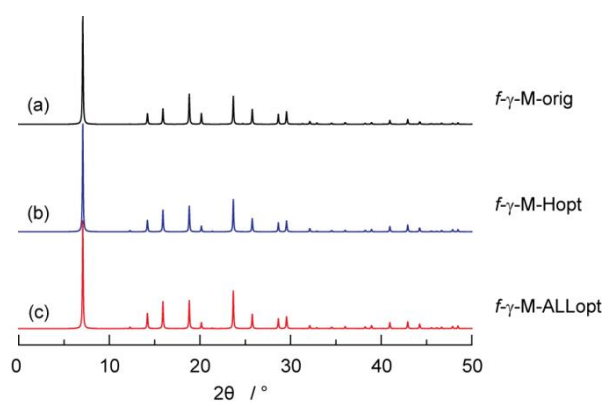


Fig. 4.9. Calculated powder X-ray diffraction profiles for the structures of (a) $f\text{-}\gamma\text{-M-orig}$, (b) $f\text{-}\gamma\text{-M-Hopt}$, and (c) $f\text{-}\gamma\text{-M-ALLOpt}$.

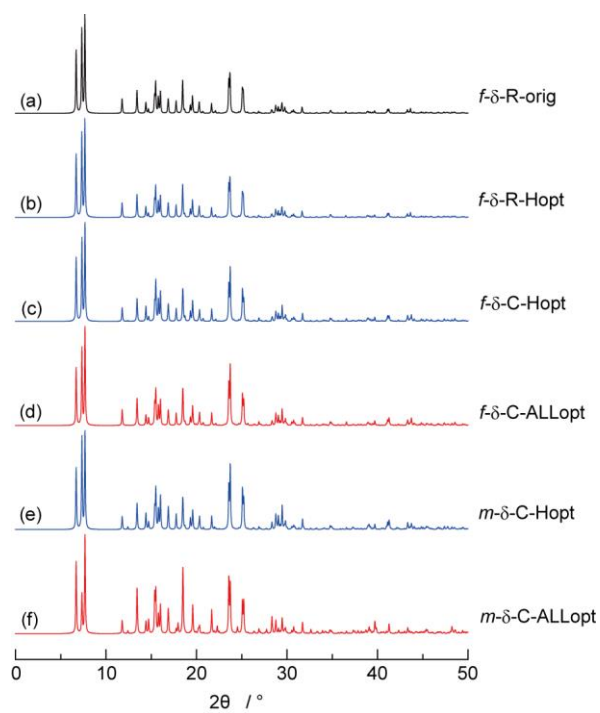


Fig. 4.10. Calculated powder X-ray diffraction profiles for the structures of (a) f - δ -R-orig, (b) f - δ -R-Hopt, (c) f - δ -C-Hopt, (d) f - δ -C-ALLopt, (e) m - δ -C-Hopt, and (f) m - δ -C-ALLopt.

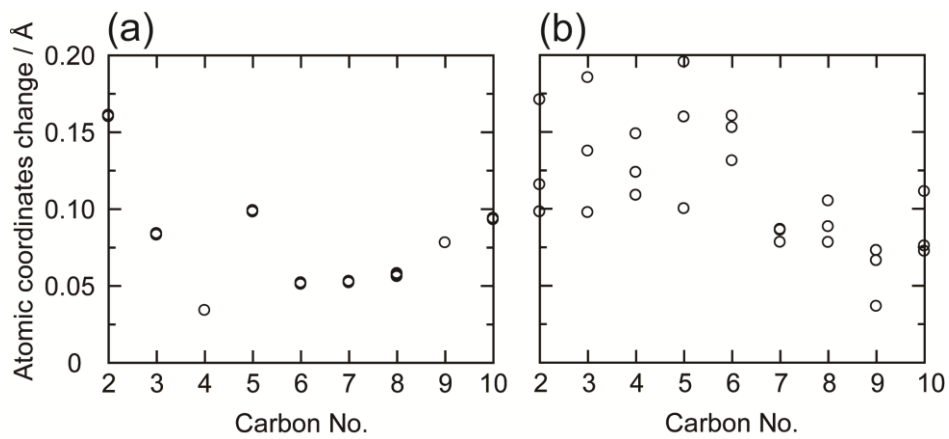


Fig. 4.11. Atomic coordinate displacements of the carbons between the H-optimization and ALL-optimization structures for (a) γ -Alq₃ and (b) Cölle's δ -Alq₃.

4.4. Conclusion

The intra- and intermolecular structures of an important organic device material, Alq₃, were investigated in detail by the combination of simple CP/MAS ¹³C experiments and GIPAW isotropic chemical-shift calculations. The X-ray-determined crystal structures were refined for γ -Alq₃ and δ -Alq₃, using the combined method. For γ -Alq₃, single resonance lines were observed for the respective carbon species in the CP/MAS ¹³C spectrum, showing that γ -Alq₃ consists of *facial* isomers. The result also indicated that the three ligands are equivalent not only in terms of intramolecular interaction, but also in terms of intermolecular interaction. In contrast, the splitting of resonance lines was observed for the respective carbon species in the CP/MAS ¹³C spectrum of δ -Alq₃. There is a possibility that the splitting might originate from intramolecular interaction; i.e., δ -Alq₃ might consist of *meridional* isomers whose three ligands are not equivalent. However, the additional GIPAW calculations for the isolated molecules extracted from γ -Alq₃ and δ -Alq₃ crystals clearly showed that the isolated Alq₃ molecules have similar intramolecular structures exclusively in *facial* form and provide similar isotropic chemical shifts when the intermolecular interactions are neglected. Therefore, the resonance line splitting for the δ -Alq₃ crystals is definitely found to originate from the intermolecular packing effect, not from the intramolecular interaction. Both γ -Alq₃ and δ -Alq₃ crystals have unconventional blue emission with similar photoluminescence spectra, although they have different intermolecular packing, as shown above. The intra- and intermolecular structures of γ -Alq₃ and δ -Alq₃ determined in this Chapter indicate that the *facial* isomeric states are the origin of the blue emission, not the intermolecular interactions.

CP/MAS ¹³C spectra contain precise information on inter- and intramolecular structures. The crystal structures determined by WAXD analysis were refined for both γ -Alq₃ and δ -Alq₃ through the combined use of GIPAW calculations. This method can reveal whether the molecules are

purely *meridional* or purely *facial*, or a mixture. The coexistence of different polymorphs can be also revealed. These distinctions are sometimes difficult to make by conducting WAXD experiments alone. This method can also clarify the origin of the chemical-shift change, which is important as described above.

In this Chapter, the crystal structures determined by WAXD were used as initial structures. In the future, iterative analysis is expected to become possible by performing only simple CP/MAS experiments and GIPAW calculations with the increasing processing power of computers. The structural analysis of materials in disordered or amorphous states is also expected.

(Chapter 4 is the unedited Author's version of a Submitted Work that was subsequently accepted for publication in *J. Phys. Chem. C*, copyright © American Chemical Society after peer review.

To access the final edited and published work see the following website:
<http://pubs.acs.org/doi/abs/10.1021/jp404430v>)

References

- [1] T. Gullion and J. Schaefer, *J. Magn. Reson.*, 81 (1989) 196.
- [2] G. R. Marshall, D. D. Beusen, K. Kocielek, A. S. Redlinski, M. T. Leplawy, Y. Pan and J. Schaefer, *J. Am. Chem. Soc.*, 112 (1990) 963.
- [3] G. Dabbagh, D. P. Weliky and R. Tycko, *Macromolecules*, 27 (1994) 6183.
- [4] A. E. Bennett, C. M. Rienstra, M. Auger, K. V. Lakshmi and R. G. Griffin, *J. Chem. Phys.*, 103 (1995) 6951.
- [5] K. Schmidt-Rohr, *Macromolecules*, 29 (1996) 3975.
- [6] D. M. Grant and R. K. Harris, eds., *Encyclopedia of Nuclear Magnetic Resonance*, Wiley, Chichester, U. K. 1996.

- [7] M. Hong, J. D. Gross and R. G. Griffin, *J. Phys. Chem. B*, 101 (1997) 5869.
- [8] K. Schmidt-Rohr, W. Hu and N. Zumbulyadis, *Science*, 280 (1998) 714.
- [9] I. Schnell, S. P. Brown, H. Y. Low, H. Ishida and H. W. Spiess, *J. Am. Chem. Soc.*, 120 (1998) 11784.
- [10] S. P. Brown, I. Schnell, J. D. Brand, K. Mullen and H. W. Spiess, *J. Am. Chem. Soc.*, 121 (1999) 6712.
- [11] K. Takegoshi, S. Nakamura and T. Terao, *Chem. Phys. Lett.*, 344 (2001) 631.
- [12] H. Kaji and K. Schmidt-Rohr, *Macromolecules*, 34 (2001) 7368.
- [13] H. Kaji and K. Schmidt-Rohr, *Macromolecules*, 34 (2001) 7382.
- [14] T. Asakura, J. Ashida, T. Yamane, T. Kameda, Y. Nakazawa, K. Ohgo and K. Komatsu, *J. Mol. Biol.*, 306 (2001) 291.
- [15] S. P. Brown and H. W. Spiess, *Chem. Rev.*, 101 (2001) 4125.
- [16] H. Kaji and K. Schmidt-Rohr, *Macromolecules*, 35 (2002) 7993.
- [17] A. E. Tonelli, *NMR Spectroscopy and Polymer Microstructure: The Conformational Connection*, VCH, Verlagsgesellschaft, Weinheim, 1989.
- [18] F. Auriemma, R. Born, H. W. Spiess, C. Derosa and P. Corradini, *Macromolecules*, 28 (1995) 6902.
- [19] R. Born, H. W. Spiess and J. Seelig, *Ab Initio Calculations of Conformational Effects on ¹³C NMR Spectra of Amorphous Polymers*, Springer, New York, 1997.
- [20] F. London, *J. Phys. Radium.*, 8 (1937) 397.
- [21] Ditchfie.R, *Mol. Phys.*, 27 (1974) 789.
- [22] K. Wolinski, J. F. Hinton and P. Pulay, *J. Am. Chem. Soc.*, 112 (1990) 8251.
- [23] G. Schreckenbach and T. Ziegler, *J. Phys. Chem.*, 99 (1995) 606.
- [24] G. Rauhut, S. Puyear, K. Wolinski and P. Pulay, *J. Phys. Chem.*, 100 (1996) 6310.

- [25] C. J. Pickard and F. Mauri, *Phys. Rev. B*, 63 (2001) 245101.
- [26] J. R. Yates, T. N. Pham, C. J. Pickard, F. Mauri, A. M. Amado, A. M. Gil and S. P. Brown, *J. Am. Chem. Soc.*, 127 (2005) 10216.
- [27] A. C. Uldry, J. M. Griffin, J. R. Yates, M. Perez-Torralba, M. D. S. Maria, A. L. Webber, M. L. L. Beaumont, A. Samoson, R. M. Claramunt, C. J. Pickard and S. P. Brown, *J. Am. Chem. Soc.*, 130 (2008) 945.
- [28] J. C. Johnston, R. J. Iuliucci, J. C. Facelli, G. Fitzgerald and K. T. Mueller, *J. Chem. Phys.*, 131 (2009) 144503.
- [29] J. Schmidt, A. Hoffmann, H. W. Spiess and D. Sebastiani, *J. Phys. Chem. B*, 110 (2006) 23204.
- [30] C. Gervais, M. Profeta, V. Lafond, C. Bonhomme, T. Azais, H. Mutin, C. J. Pickard, F. Mauri and F. Babonneau, *Magn. Reson. Chem.*, 42 (2004) 445.
- [31] J. R. Yates, S. E. Dobbins, C. J. Pickard, F. Mauri, P. Y. Ghi and R. K. Harris, *Phys. Chem. Chem. Phys.*, 7 (2005) 1402.
- [32] R. K. Harris, P. Y. Ghi, R. B. Hammond, C. Y. Ma, K. J. Roberts, J. R. Yates and C. J. Pickard, *Magn. Reson. Chem.*, 44 (2006) 325.
- [33] R. K. Harris, S. A. Joyce, C. J. Pickard, S. Cadars and L. Emsley, *Phys. Chem. Chem. Phys.*, 8 (2006) 137.
- [34] R. K. Harris, P. Hodgkinson, C. J. Pickard, J. R. Yates and V. Zorin, *Magn. Reson. Chem.*, 45 (2007) S174.
- [35] L. M. Shao, J. R. Yates and J. J. Titman, *J. Phys. Chem. A*, 111 (2007) 13126.
- [36] C. J. Pickard, E. Salager, G. Pintacuda, B. Elena and L. Emsley, *J. Am. Chem. Soc.*, 129 (2007) 8932.
- [37] S. Cadars, A. Lesage, C. J. Pickard, P. Sautet and L. Emsley, *J. Phys. Chem. A*, 113 (2009)

902.

[38] R. K. Harris, R. E. Wasylshen and M. Duer, eds., *NMR Crystallography*, Wiley, Chichester 2009.

[39] R. K. Harris, P. Hodgkinson, V. Zorin, J. N. Dumez, B. Elena-Herrmann, L. Emsley, E. Salager and R. S. Stein, *Magn. Reson. Chem.*, 48 (2010) S103.

[40] E. Salager, G. M. Day, R. S. Stein, C. J. Pickard, B. Elena and L. Emsley, *J. Am. Chem. Soc.*, 132 (2010) 2564.

[41] C. W. Tang and S. A. VanSlyke, *Appl. Phys. Lett.*, 51 (1987) 913.

[42] M. Braun, J. Gmeiner, M. Tzolov, M. Cölle, F. D. Meyer, W. Milius, H. Hillebrecht, O. Wendland, J. U. von Schütz and W. Brütting, *J. Chem. Phys.*, 114 (2001) 9625.

[43] A. Curioni, M. Boero and W. Andreoni, *Chem. Phys. Lett.*, 294 (1998) 263.

[44] M. Amati and F. Lelj, *Chem. Phys. Lett.*, 358 (2002) 144.

[45] M. Amati and F. Lelj, *J. Phys. Chem. A*, 107 (2003) 2560.

[46] M. Muccini, M. A. Loi, K. Kenevey, R. Zamboni, N. Masciocchi and A. Sironi, *Adv. Mater.*, 16 (2004) 861.

[47] H. Kaji, Y. Kusaka, G. Onoyama and F. Horii, *Jpn. J. Appl. Phys.*, 44 (2005) 3706.

[48] H. Kaji, Y. Kusaka, G. Onoyama and F. Horii, *J. Am. Chem. Soc.*, 128 (2006) 4292.

[49] M. M. Levichkova, J. J. Assa, H. Fröb and K. Leo, *Appl. Phys. Lett.*, 88 (2006) 201912.

[50] L.-L. Li, C.-J. Fang, Q. Yuan and C.-H. Yan, *Appl. Phys. Lett.*, 90 (2007) 231908.

[51] Y. Nishiyama, T. Fukushima, K. Takami, Y. Kusaka, T. Yamazaki and H. Kaji, *Chem. Phys. Lett.*, 471 (2009) 80.

[52] T. Tsuboi and Y. Torii, *Mol. Cryst. Liq. Cryst.*, 529 (2010) 42.

[53] T. Tsuboi and Y. Torii, *J. Non-Cryst. Solids*, 356 (2010) 2066.

[54] H. Bi, H. Y. Zhang, Y. Zhang, H. Z. Gao, Z. M. Su and Y. Wang, *Adv. Mater.*, 22 (2010)

1631.

[55] M. Brinkmann, G. Gadret, M. Muccini, C. Taliani, N. Masciocchi and A. Sironi, *J. Am. Chem. Soc.*, 122 (2000) 5147.

[56] M. Tagaya and M. Ogawa, *Phys. Chem. Chem. Phys.*, 10 (2008) 6849.

[57] G. Baldacchini, P. Chiacchiaretta, R. Reisfeld and E. Zigansky, *J. Lumin.*, 129 (2009) 1849.

[58] H. Bi, D. Chen, D. Li, Y. Yuan, D. Xia, Z. Zhang, H. Zhang and Y. Wang, *Chem. Commun.*, 47 (2011) 4135.

[59] M. Cölle, R. E. Dinnebier and W. Brütting, *Chem. Commun.*, 23 (2002) 2908.

[60] M. Cölle, J. Gmeiner, W. Milius, H. Hillebrecht and W. Brütting, *Adv. Funct. Mater.*, 13 (2003) 108.

[61] M. Cölle and W. Brütting, *Phys. Status Solidi A*, 201 (2004) 1095.

[62] M. Rajeswaran, T. N. Blanton, C. W. Tang, W. C. Lenhart, S. C. Switalski, D. J. Giesen, B. J. Antalek, T. D. Pawlik, D. Y. Kondakov, N. Zumbulyadis and R. H. Young, *Polyhedron*, 28 (2009) 835.

[63] M. Rajeswaran, T. N. Blanton and K. P. Klubek, *Z. Kristallogr. New Cryst. Struct.*, 218 (2003) 439.

[64] C. F. Macrae, I. J. Bruno, J. A. Chisholm, P. R. Edgington, P. McCabe, E. Pidcock, L. Rodriguez-Monge, R. Taylor, J. van de Streek and P. A. Wood, *J. Appl. Crystallogr.*, 41 (2008) 466.

[65] T. Fukushima and H. Kaji, *Org. Electron.*, 13 (2012) 2985.

Chapter 5

Clarification of Isomeric Structures and the Effect of Intermolecular Interactions in Blue-emitting Aluminum Complex Alq₃ using First-principles ²⁷Al NMR Calculations

5.1. Introduction

As described in Chapter 4, tris(8-hydroxyquinoline) aluminum(III) (Alq₃) has been widely used as light-emitting and electron-transporting material in organic light-emitting diodes (OLEDs) since its use was first reported by Tang and VanSlyke [1]. Originally, the emission of Alq₃ was observed as the green color. However, recently, blue-emitting Alq₃ crystals in γ - and δ -polymorphs (γ - and δ -Alq₃) have been found [2-5]. These blue-emitting species exhibit photoluminescence quantum yields of ca. 50%, twofold greater than that of conventional Alq₃. To understand the different luminescence properties, investigations into the origin of the variation in emission wavelength have been carried out and two possible explanations are presently considered. The first one is related to intermolecular interactions that should change the wavelength by the effect of intermolecular packing [6-9]. The second explanation is related to a change of the intramolecular structure, that is to say, the isomeric states [2, 5, 10-20]. Two isomeric forms are known for Alq₃, the “*facial*” and “*meridional*” isomers (Figure 5.1). The *facial* isomer has C_3 symmetry with three equivalent ligands, while the *meridional* isomer has lower C_1 symmetry and its three ligands are non-equivalent.

In Chapter 4, we carried out a structural analysis using a combination of ¹³C cross-polarization/magic angle spinning (CP/MAS) NMR experiments and gauge-including projector-augmented wave (GIPAW) [21] chemical shift calculations. From the analysis, we found that the crystal structures determined by wide-angle X-ray diffraction could be refined, and that there

was a clear difference between the experimental CP/MAS ^{13}C NMR spectra of γ - and δ -Alq₃ crystals. It was shown: (i) that this difference originates from the intermolecular interactions in each crystal, and (ii) that the intramolecular structures of Alq₃ in γ - and δ -Alq₃ are similar.

In this Chapter, we attempt a further joint analysis by ^{27}Al MAS NMR and GIPAW calculations. As shown below, it is found that the ^{27}Al NMR spectra of the γ - and δ -Alq₃ crystals are very sensitive to the intramolecular structures but are little affected by the intermolecular interactions. This is opposite to what has been determined by the ^{13}C analysis, which allows carrying a detailed analysis of intra- and intermolecular structures using the combination of ^{27}Al and ^{13}C MAS spectra. We also evaluate intermolecular interactions by using GIPAW calculations on the isolated molecules and those in crystalline-packed molecules.

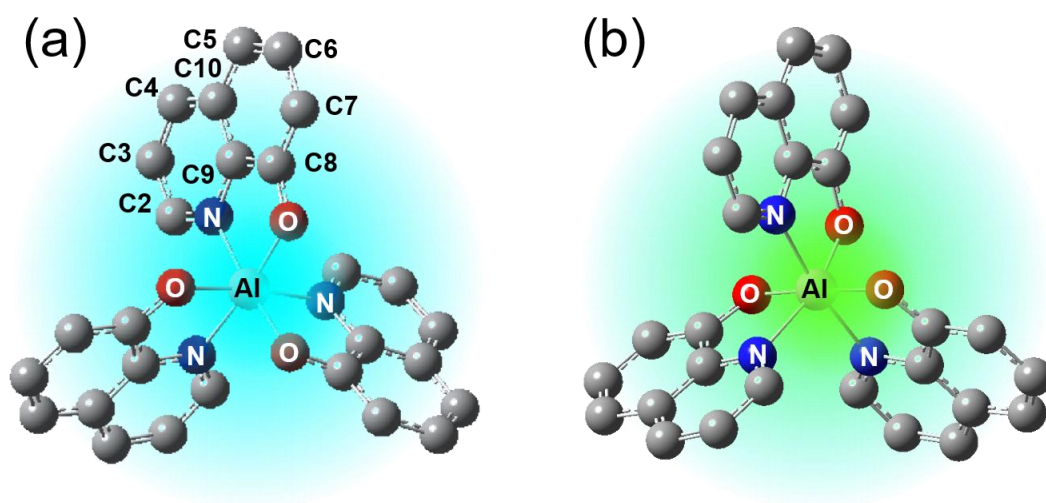


Fig. 5.1. Molecular structures of Alq_3 in (a) *facial* and (b) *meridional* isomeric states.

Hydrogen atoms are omitted for clarity.

5.2 Experimental and computational section

5.2.1. Experimental

The γ -Alq₃ sample was prepared by thermal annealing of sublimed Alq₃ at 407 °C for 10 s under vacuum [14]. The δ -Alq₃ sample was prepared by thermal annealing of sublimed Alq₃ under vacuum at 420 °C for 5 h in a vacuum-encapsulated quartz glass tube, followed by slow cooling to room temperature [22]. The NMR experiments were performed using a Chemagnetics CMX-400 Infinity spectrometer at room temperature. The ²⁷Al operating frequency was set to 100.7 MHz. A double resonance probe with a 4-mm MAS probe-head was used. The MAS spinning speed was set to 15 kHz. ¹H dipolar decoupled ²⁷Al MAS NMR spectra under ¹H dipolar decoupling were measured with a ²⁷Al pulse length of 2.2 μ s. 1M Al(NO₃)₃ aqueous solution was used as a chemical shift reference. ²⁷Al MAS spectrum was simulated by quadrupolar asymmetry parameter (η_q) and quadrupolar coupling constant (C_q) determines the peak width and the isotropic chemical shifts. C_q solidify the spectrum width, η_q solidify spectrum shape, and the isotropic chemical shift determines upfield and downfield shift. Analysis of these parameters provides local structure information.

5.2.2. Computation

For GIPAW calculations, the following crystal structures were used: 1) γ -Alq₃ in *facial* form proposed by Muccini *et al.* [5], 2) δ -Alq₃ in *facial* form proposed by Rajeswaran *et al.* [23], 3) δ -Alq₃ in *facial* form proposed by Cölle *et al.* [3] and 4) δ -Alq₃ in *meridional* form reported by Cölle *et al.* [3]. Note that for 4), δ -Alq₃ in *meridional* form was reported by Cölle *et al.* [3] as being an inaccurate structure but we used this structure for comparison. Among these, the Crystallographic Information File (CIF) of 1) and 2) include the H, C, N, O, and Al coordinates, and can be used for the chemical shift calculations without modification. The CIFs of 3) and 4) do not contain the H coordinates. Therefore, for these cases we attached H atoms to the crystal structure. The geometry coordinates are optimized only for the H atoms with all other coordinates for the Al, N, O, and C atoms kept fixed (Hopt) as initial structures. We also carried out further optimizations whereby all atom positions were optimized using the H-optimized structures (ALLOpt). All of the above geometry optimizations were carried out under periodic boundary conditions. The space group is $P\bar{3}$ for γ -Alq₃ and $P\bar{1}$ for δ -Alq₃, irrespective of the isomeric states. Cell parameters and space groups were kept constant for all of the structures. The geometry optimization calculations were carried out using the CASTEP program (Dassault Systèmes Biovia Corp., San Diego, CA, USA). ²⁷Al and ¹³C NMR calculations were carried out under periodic boundary conditions using the GIPAW module implemented in NMR-CASTEP. For the geometry optimization, the Perdew–Burke–Ernzerhof (PBE) approximation and ultrasoft pseudopotentials with a plane-wave energy cutoff of 380 eV were used. A 2×2×4 Monkhorst-Pack *k*-point grid was used for Brillouin zone sampling for all of the above crystal structures. For the GIPAW calculation, the PBE approximation and “On the fly” pseudopotentials were used. The energy cutoff of the plane wave was set to 610 eV.

GIPAW calculations were also carried out on isolated molecules extracted from the respective

crystals without further structural optimization. The isolated molecules are denoted by appending “IM” to the abbreviated names of each corresponding crystal structure. These abbreviations of the crystal structures are summarized in Table 5.1. For the isolated molecule calculations, we systematically changed the size of the cubic cell and found that a cube with dimensions of 32 Å is sufficient to neglect the effect of intermolecular interactions on the ^{27}Al and ^{13}C NMR parameters (Figures 5.2 and 5.3). A $1\times 1\times 1$ Monkhorst-Pack k -point grid was used for Brillouin zone sampling for all of the isolated molecule models. The forces for the original and H-optimized crystals are greater than 1.0 eV \AA^{-1} , indicating that these crystals are not truly appropriate structures (see Table 4.1 in Chapter 4 for the details). There remain large forces on the heavy atoms even after H-optimization. Therefore, our full optimization for all atoms is thought to be a reasonable procedure. All of the forces are within 1.0 eV \AA^{-1} for the ALL-optimized crystals (see Table 4.2 in Chapter 4). Using the parameters obtained by the GIPAW calculations, ^{27}Al MAS NMR spectra were calculated by an in-house written C++ program [24]. The chemical shift reference, σ_{ref} , was set to 491.6 ppm and 490.6 ppm for $\gamma\text{-Alq}_3$ and $\delta\text{-Alq}_3$, respectively.

Table 5.1. Abbreviations used for Alq₃ crystals.

crystal structure	γ -form	δ -form by	δ -form	
	by Muccini et al. [5]	Rajeswaran et al. [23]	by Cölle et al. [3]	
isomeric state	<i>facial</i>	<i>facial</i>	<i>facial</i>	<i>meridional</i>
original	<i>f-γ-M-orig</i>	<i>f-δ-R-orig</i>	-	-
H- optimization	<i>f-γ-M-Hopt</i>	<i>f-δ-R-Hopt</i>	<i>f-δ-C- Hopt</i>	<i>m-δ-C- Hopt</i>
ALL- optimization	<i>f-γ-M- ALLOpt</i>	<i>f-δ-R- ALLOpt</i>	<i>f-δ-C- ALLOpt</i>	<i>m-δ-C- ALLOpt</i>

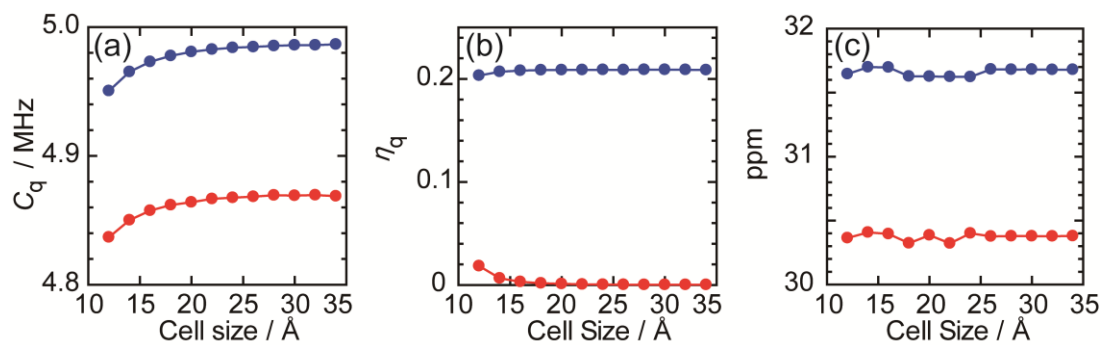


Fig. 5.2. Cell size dependencies of (a) C_q , (b) η_q and (c) isotropic chemical shift values calculated by GIPAW for γ -Alq₃ (●) and δ -Alq₃ (●) molecules in a cubic cell. Each molecule was extracted from the crystal structure after optimization of the coordinates of all atoms.

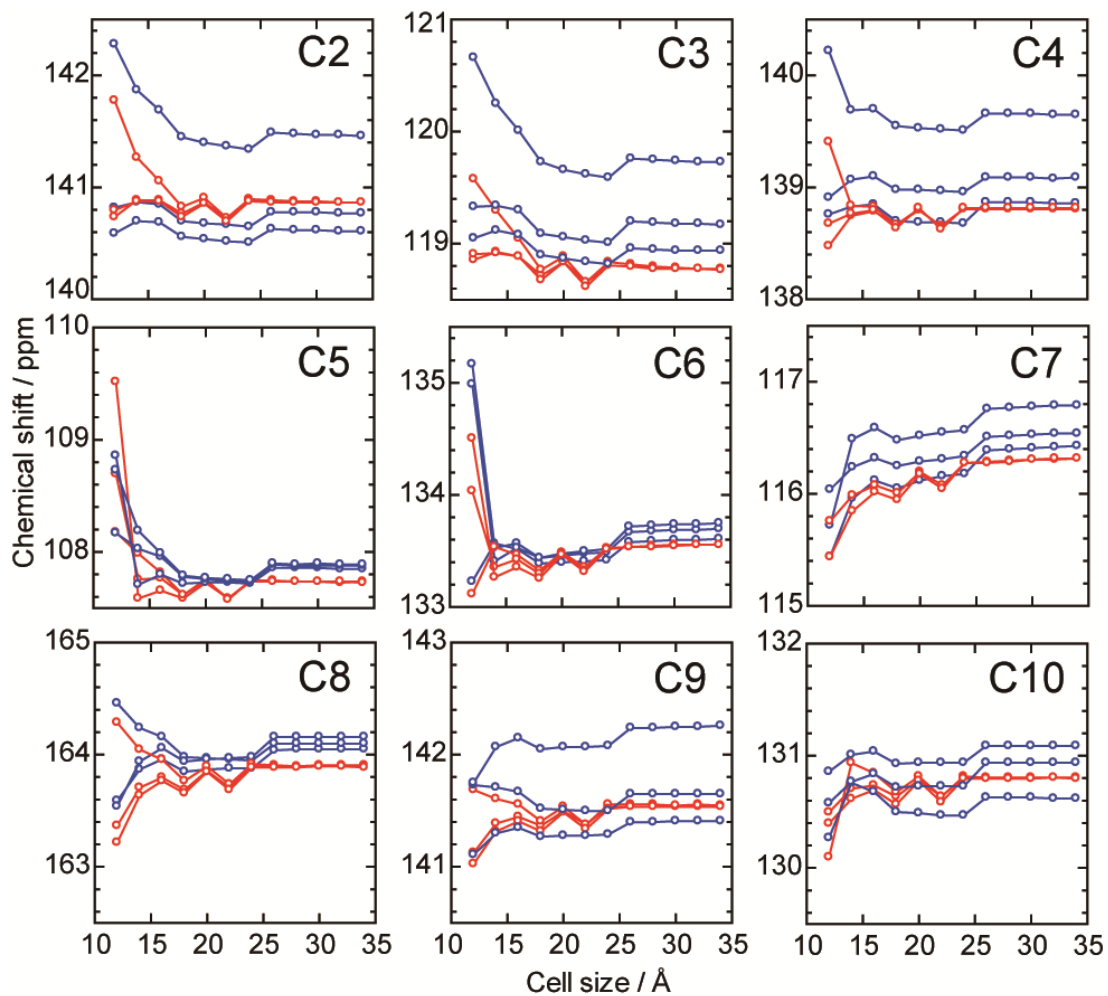


Fig. 5.3. Cell size dependence of ^{13}C isotropic chemical shift values calculated by GIPAW for $\gamma\text{-Alq}_3$ (●) and $\delta\text{-Alq}_3$ (●) molecules in a cubic cell. Each molecule was extracted from the crystal structure after optimization of the coordinates of all atoms.

5.3. Results and discussion

5.3.1. ^{27}Al NMR of $\gamma\text{-Alq}_3$

We have investigated ^{27}Al NMR spectra of $\gamma\text{-Alq}_3$ by GIPAW calculations in the crystalline structure; both intra- and intermolecular interactions are considered. Figure 5.4a shows the experimental ^{27}Al MAS spectrum of $\gamma\text{-Alq}_3$. The quadrupolar parameters, η_q and the quadrupolar coupling constant, C_q , obtained from the experimental spectrum are also shown. The η_q value reflects the spectral line shape and the C_q value determines the peak width. The experimental spectrum shows axially symmetric quadrupolar tensor; the η_q value is thus zero, which indicates that $\gamma\text{-Alq}_3$ possesses an axially symmetric *facial* structure. Figure 5.4b shows the GIPAW-calculated ^{27}Al MAS spectrum of $\gamma\text{-Alq}_3$ crystal in a *facial* form. To obtain this spectrum, a single point GIPAW-calculation was performed using the crystal structure determined by Muccini *et al.* [5]. We label this original structure *f- γ -M-orig*. We also carried out GIPAW calculations on the crystal obtained either by only optimizing the proton positions while keeping the other nuclear positions fixed (Hopt), or on systems where all atom positions were optimized (ALLOpt). All the results are given in Table 5.2. These crystals optimized from *f- γ -M-orig* are labeled *f- γ -M-Hopt* and *f- γ -M-ALLOpt* (see Table 5.1). The GIPAW-calculated ^{27}Al MAS spectra for these crystals are shown in Figures 5.4b-5.4d. All geometry optimizations were carried out under periodic boundary conditions, including the structures described *vide infra*. We could not find clear relationship between the chemical shielding parameters and the structures (Table 5.2). The key parameters for the determination of intra- and intermolecular structures are C_q and η , as discussed in below. All of the spectra in Figures 5.4b-d are axially symmetric with $\eta_q = 0$. The calculated results show that the symmetry axis of the quadrupole tensor is parallel to the C_3 symmetry axis of the molecules. As will be described later, the η_q values are not zero

if the Alq_3 molecular structure is *meridional*. Even for the *facial* isomer, the η_q values are not zero when the structure is distorted from C_3 symmetry. Although all of the η_q values are zero in Figure 5.4, the peak widths differ largely from each other. Those for *f- γ -M-orig* and *f- γ -M-Hopt* are significantly narrower compared with the experimentally observed peak widths. *f- γ -M-ALLOpt* shows a wider pattern, reproducing the experimental one. This result clearly shows that *f- γ -M-ALLOpt* is the most appropriate structure among the three considered, confirming ^{13}C NMR study in Chapter 4.

To clarify the effect of intermolecular interactions, GIPAW calculations were also carried out on isolated molecules extracted from the respective crystals without further structural optimization (Fig. 5.4e-g). The isolated molecules are denoted by appending “IM” to the abbreviated names of the respective crystals. Figure 5.4g shows the GIPAW-calculated ^{27}Al MAS spectrum for *f- γ -M-ALLOpt-IM* (see also Table 5.2). In Chapter 4, it is found that ^{13}C isotropic chemical shifts show significant dependence on the intermolecular interactions. On the contrary, the ^{27}Al MAS spectra do not show significant dependence on intermolecular interactions (compare Figures 5.4b and 5.4e, 5.4c and 5.4f, 5.4d and 5.4g, respectively). The difference between the ^{13}C and ^{27}Al NMR may be easily explained. ^{13}C chemical shifts are affected by the whole electric cloud spanning all molecules, whereas quadrupole interactions are dominated by the local electric field gradients. Thus, ^{27}Al NMR spectra little depend on intermolecular interactions as the aluminum atom is located at the center of the Alq_3 molecule, which is far from any neighboring molecule. This clearly shows that it is possible to precisely determine the intramolecular structure from ^{27}Al NMR analysis of Alq_3 without the need to consider the intermolecular interactions.

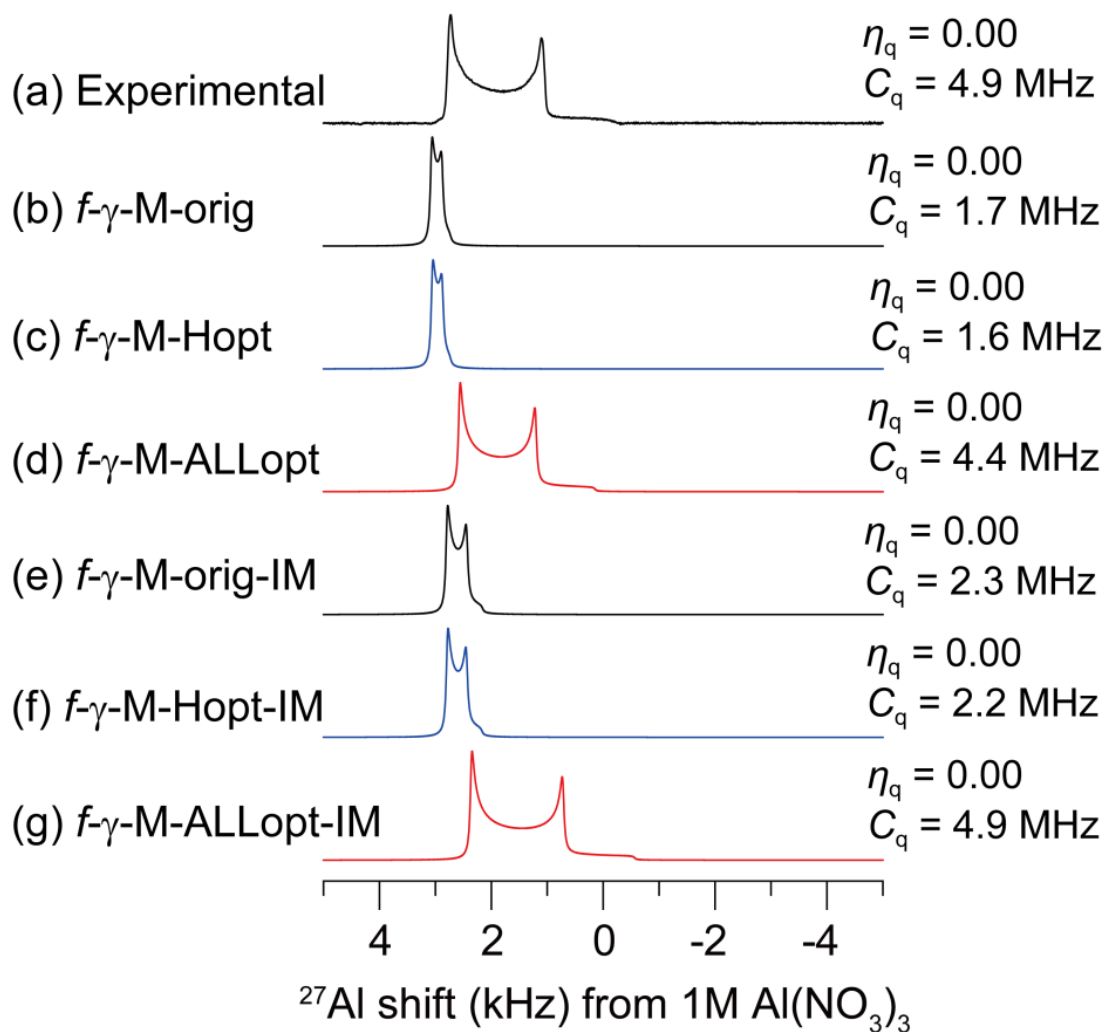


Fig. 5.4. (a) Experimental and (b)–(g) calculated dipolar decoupled ^{27}Al MAS spectra of γ - Alq_3 . For all spectra, $\eta_q = 0$.

Table 5.2. GIPAW-calculated C_q and η_q for ^{27}Al of $\gamma\text{-Alq}_3$.

	C_q (MHz)	η_q	δ_{iso} (ppm)
Experimental	4.9	0.00	31.3
<i>f</i> - γ -M-orig	1.7	0.00	33.1
<i>f</i> - γ -M-Hopt	1.6	0.00	32.9
<i>f</i> - γ -M-ALLOpt	4.4	0.00	31.6
<i>f</i> - γ -M-orig-IM	2.3	0.00	30.9
<i>f</i> - γ -M-Hopt-IM	2.2	0.00	30.8
<i>f</i> - γ -M-ALLOpt-IM	4.9	0.00	30.4

5.3.2. ^{27}Al NMR of $\delta\text{-Alq}_3$

We also investigate ^{27}Al NMR of $\delta\text{-Alq}_3$. Figure 5.5a shows the experimental ^{27}Al MAS spectrum of $\delta\text{-Alq}_3$, and Figures 5.5b–h show the GIPAW calculated spectra. The following crystal structures were used for the calculations. For the *facial* form, we have used the two crystal structures proposed by Rajeswaran *et al.* [23] and by Cölle *et al.* [3]. The crystal composed of the *meridional* form reported by Cölle *et al.* was also used for comparison, although it was shown in Ref. 3 to be an inaccurate structure. As with the $\gamma\text{-Alq}_3$ case, Hopt and ALLOpt optimizations were carried out for the three proposed crystals (see Table 5.1). Because the H coordinates are not provided in Ref. 3, GIPAW calculations were not carried out on Cölle's original structure. All the results are given in Table 5.3. Similar in the case of $\gamma\text{-Alq}_3$, we could not find clear relationship between the chemical shielding parameters and the structures. The η_q and C_q values determined from the experimental spectrum are 0.23 and 4.8 MHz, respectively. The calculated η_q values for *f*- δ -R-orig (Figure 5.5b) and *f*- δ -R-Hopt (Figure 5.5c) do not match the experimental value, although the C_q values perfectly agree with the experiment. In contrast, the C_q value for *f*- δ -C-Hopt (Figure 5.5d) does not match perfectly the experiment, although the η_q value becomes close to that experimentally observed. The calculated spectrum for *m*- δ -C-Hopt (Figure 5.5e) significantly deviates from the experimental spectrum (see also Figure 5.6e for the complete spectra of Figure 5.5e), with both the η_q and C_q values inconsistent with the experiment. On the contrary, the spectrum of *f*- δ -R-ALLOpt (Figure 5.5f) agrees well with experiment ($\eta_q = 0.27$ and $C_q = 4.5$ MHz) and that of *f*- δ -C-ALLOpt in Figure 5.5g shows better agreement ($\eta_q = 0.23$ and $C_q = 4.6$ MHz). The results indicate that ALLOpt crystals composed of *facial* isomers provide more refined structures compared with the original and Hopt structures. The calculated spectrum for *m*- δ -C-ALLOpt (Figure 5.5h) significantly differs from the experiment (see also Fig. 5.6h for the complete spectra). This clearly shows that $\delta\text{-Alq}_3$ is only

composed of *facial* isomers, not of *meridional* ones, though the experimental η_q is not zero. Even if a small proportion of the *meridional* isomers were present, they could be difficult to detect experimentally because of the large second-order quadrupolar broadening of the *meridional* isomers.

Figures 5.5i–o shows the GIPAW-calculated ^{27}Al MAS spectra for isolated molecules extracted from the respective crystals in Figures 5.5b–h (See also Table 5.3). One observes that the spectra calculated for isolated molecules are very similar to those for the crystals. This confirms that the ^{27}Al MAS spectra of Alq_3 do not depend on the intermolecular interactions and are determined solely from the intramolecular structure.

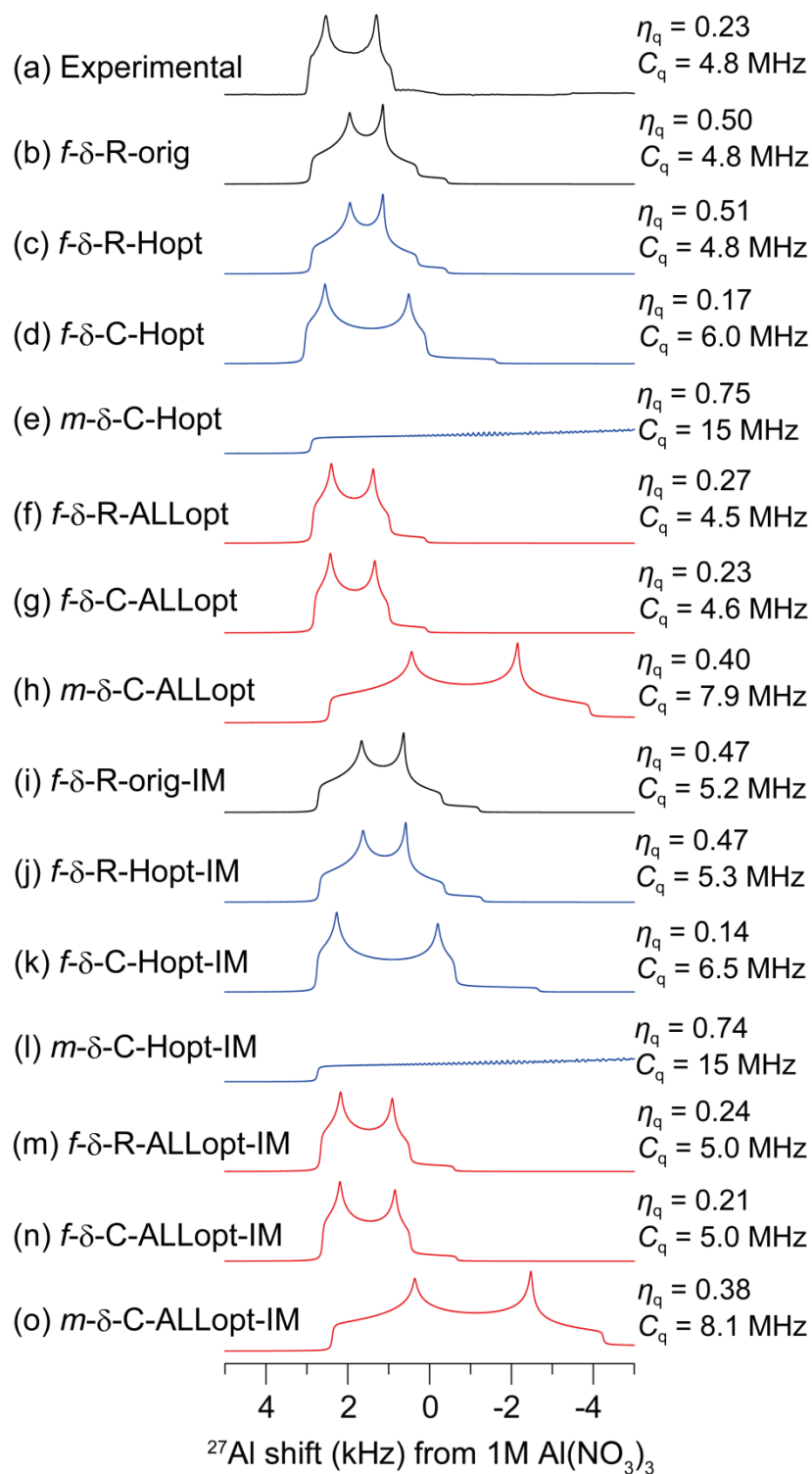


Fig. 5.5. (a) Experimental and (b)–(k) calculated ^{27}Al MAS spectra of $\delta\text{-Alq}_3$. See Fig. 5.6

for the full spectrum of Fig. 5.5e and 5.6l.

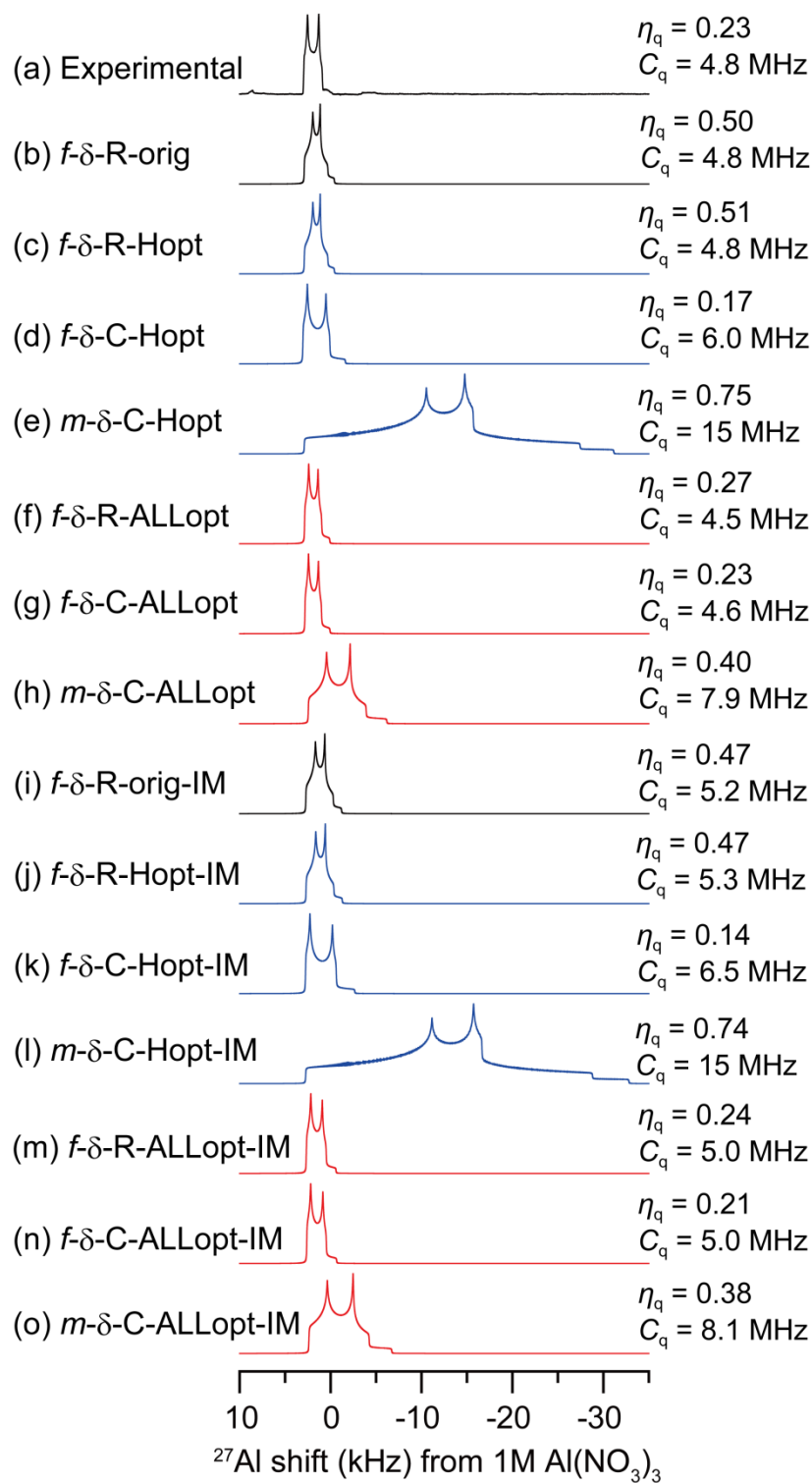


Fig. 5.6. Complete spectra of Fig. 5.5.

Table 5.3. GIPAW-calculated C_q and η_q for ^{27}Al of $\delta\text{-Alq}_3$.

	C_q (MHz)	η_q	δ_{iso} (ppm)
Experimental	4.8	0.24	31.0
<i>f</i> - δ -R-orig	4.8	0.50	32.5
<i>f</i> - δ -R-Hopt	4.8	0.51	32.4
<i>f</i> - δ -C-Hopt	6.0	0.17	37.7
<i>m</i> - δ -C-Hopt	14.8	0.75	34.1
<i>f</i> - δ -R-ALLOpt	4.5	0.27	33.1
<i>f</i> - δ -C-ALLOpt	4.6	0.23	33.0
<i>m</i> - δ -C-ALLOpt	7.9	0.40	31.4
<i>f</i> - δ -R-orig-IM	5.2	0.47	31.2
<i>f</i> - δ -R-Hopt-IM	5.3	0.47	30.9
<i>f</i> - δ -C-Hopt-IM	6.5	0.14	36.1
<i>m</i> - δ -C-Hopt-IM	15.1	0.74	32.9
<i>f</i> - δ -R-ALLOpt-IM	5.0	0.24	31.9
<i>f</i> - δ -C-ALLOpt-IM	5.0	0.21	31.7
<i>m</i> - δ -C-ALLOpt-IM	8.1	0.38	31.4

In our previous work on ^{27}Al NMR [13], we made the hypothesis that the non-zero η_q value of δ - Alq_3 crystal was related to the intermolecular interaction. For this assumption to be correct, η_q values should be zero for isolated molecules extracted from the crystals f - δ -R-ALLOpt and f - δ -C-ALLOpt. However, it is clear from Figures 5.5m and 5.5n that the η_q values for isolated molecules are similar to those for the crystals (Figures 5.5f and 5.5g). This demonstrates that the origin of the non-zero η_q value of δ - Alq_3 crystal is not the intermolecular interaction but the structural deviation of Alq_3 from C_3 symmetry.

The asymmetry parameter, η_q , reflects the structural symmetry around the observed atom. The *facial* isomer has C_3 symmetry, while the *meridional* isomer has C_1 symmetry (see Figure 5.1). At the beginning, we expected η_q values for *facial* isomer to be very small compared with that for *meridional* isomer because of its higher symmetry. However, it is not perfectly true. Actually the *facial* shows a η_q of 0-0.51 while the *meridional* gives 0.38-0.75. Also, Figure 5.6 and Table 5.4 show intra-molecular geometrical parameters (bond length, angles, and torsions) for f - γ -M-ALLOpt-IM and f - δ -C-ALLOpt-IM. The geometrical parameters mostly agree with each other, indicating that the intramolecular structures of Alq_3 in the γ - and δ - Alq_3 crystals are basically the same. However, unlike the case of f - γ -M-ALLOpt-IM, f - δ -C-ALLOpt-IM do not have three-fold axis, although has near- C_3 axis. From those comparisons, it is considered that small structural changes of three ligands in Alq_3 molecule would perceptively effect on the η_q values. Thus, we cannot determine whether the structure is *facial* or *meridional* isomer solely from the η_q value. Instead, the structure symmetry can be precisely determined from the η_q values, at least for *facial* isomers, because the η_q value is found to be very sensitive to any deviation from C_3 symmetry. The γ - and δ - Alq_3 crystals both exhibited sky-blue emission and the maximum wavelengths are very close to each other, 470 and 468 nm, respectively. The reason that these Alq_3 crystals show a different emission color compared with normal green

emission must be that the molecules in these crystals are *facial* isomers, not *meridional*. Neither the different intermolecular packings nor deviation from C_3 symmetry affect the emission wavelengths.

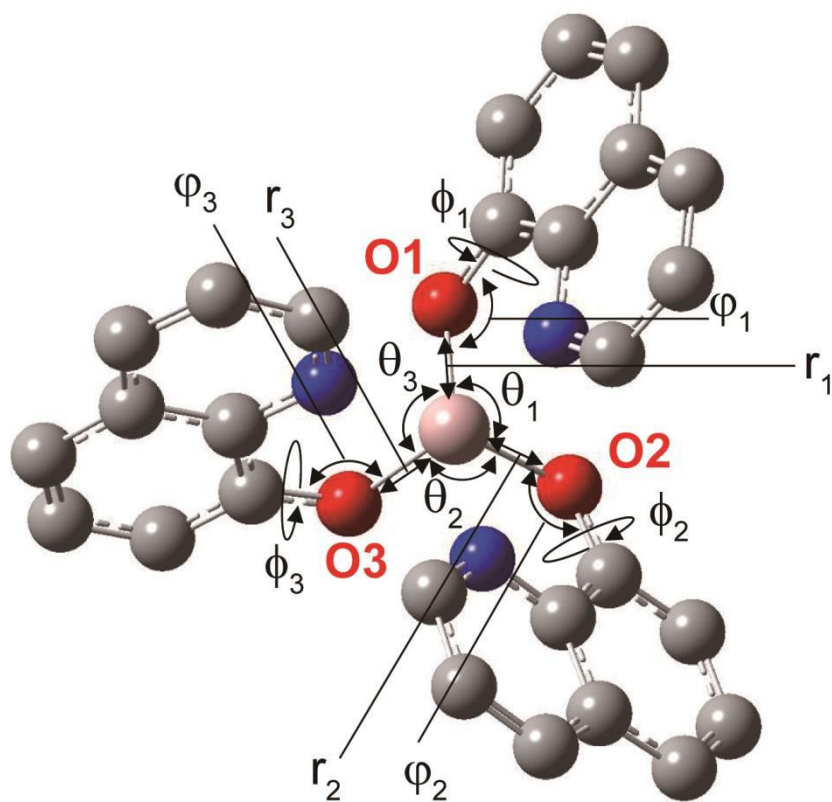


Fig. 5.6. Geometry parameters of Alq₃: bond lengths r_1 , r_2 , and r_3 ; bond angles θ_1 , θ_2 , and θ_3 ; and torsion angles ϕ_1 , ϕ_2 , and ϕ_3 .

Table 5.4. Representative geometric parameters for the original and optimized γ -Alq₃ and δ -Alq₃ crystals.

Structure	Bond angle / °			Torsion angle / °			Bond length / Å		
	θ_1	θ_2	θ_3	ϕ_1	ϕ_2	ϕ_3	r_1	r_2	r_3
<i>f</i> - γ -M-orig	90.6	90.6	90.6	-2.58	-2.58	-2.58	1.90	1.90	1.90
<i>f</i> - γ -M-Hopt	90.6	90.6	90.6	-2.58	-2.58	-2.58	1.90	1.90	1.90
<i>f</i> - γ -M-ALlopt	95.4	95.4	95.4	1.43	1.43	1.43	1.88	1.88	1.88
<i>f</i> - δ -R-orig	95.7	97.3	94.5	4.11	4.94	5.81	1.86	1.83	1.85
<i>f</i> - δ -R-Hopt	95.7	97.3	94.5	4.11	4.94	5.81	1.86	1.83	1.85
<i>f</i> - δ -C-Hopt	99.0	100	95.0	0.520	5.10	-3.23	1.88	1.89	1.88
<i>m</i> - δ -C-Hopt	100	149	84.6	-8.13	-11.8	-1.93	1.87	1.84	1.86
<i>f</i> - δ -R-ALlopt	95.4	97.0	94.8	-2.56	-5.11	4.07	1.88	1.88	1.87
<i>f</i> - δ -C-ALlopt	95.3	96.8	95.1	2.87	5.09	-3.97	1.88	1.88	1.87
<i>m</i> - δ -C-ALlopt	87.9	172	99.8	10.4	-15.3	0.84	1.85	1.92	1.86

5.4. Conclusions

In this Chapter, we have performed structure analysis on blue-emitting aluminum complex crystals γ - and δ -Alq₃ by a combination of ²⁷Al MAS NMR and GIPAW calculations. In contrast to the isotropic chemical shifts obtained by ¹³C CP/MAS NMR experiments, quadrupolar parameters obtained by ²⁷Al MAS NMR are found to be mostly sensitive to intramolecular structures. Our GIPAW calculation of ¹³C isotropic chemical shifts shows that the intramolecular structures of Alq₃ molecules in γ -Alq₃ and δ -Alq₃ with C₃ and approximate C₃ symmetries, respectively, are very similar, but that their intermolecular structures are significantly different. ¹³C CP/MAS NMR is very sensitive to the intermolecular structure and little sensitive to the intramolecular structure. In this meaning, GIPAW analyses of ¹³C and ²⁷Al NMR are complementary to each other.

We would like to apply this method to Alq₃ in amorphous phase in the future. One problem is distinguishing the effects of intra- and intermolecular interactions upon NMR parameters. Generally, NMR parameters, such as chemical shifts, quadrupolar coupling constants, and anisotropy parameters, depend on both the intra- and intermolecular structures, which make structure analysis difficult. However, in the present case, to a good approximation ²⁷Al NMR does not depend on intermolecular interactions, which enables us to carry out precise intramolecular structure determination without considering intermolecular interactions. After the determination of the intramolecular structure, intermolecular packing can be determined by ¹³C NMR. This approach will be very useful for the analysis of amorphous systems of Alq₃.

(Chapter 5 is the unedited Author's version of a Submitted Work that was subsequently accepted for publication in *Chem. Phys. Lett*, copyright © Elsevier B.V after peer review. To access the final edited and published work see the following website:

<http://dx.doi.org/10.1016/j.cplett.2014.05.015>

References

- [1] C. W. Tang and S. A. VanSlyke, *Appl. Phys. Lett.*, 51 (1987) 913.
- [2] M. Braun, J. Gmeiner, M. Tzolov, M. Cölle, F. D. Meyer, W. Milius, H. Hillebrecht, O. Wendland, J. U. von Schütz and W. Brütting, *J. Chem. Phys.*, 114 (2001) 9625.
- [3] M. Cölle, R. E. Dinnebier and W. Brütting, *Chem. Commun.*, 23 (2002) 2908-2909.
- [4] M. Cölle, J. Gmeiner, W. Milius, H. Hillebrecht and W. Brütting, *Adv. Funct. Mater.*, 13 (2003) 108.
- [5] M. Muccini, M. A. Loi, K. Kenevey, R. Zamboni, N. Masciocchi and A. Sironi, *Adv. Mater.*, 16 (2004) 861.
- [6] M. Brinkmann, G. Gadret, M. Muccini, C. Taliani, N. Masciocchi and A. Sironi, *J. Am. Chem. Soc.*, 122 (2000) 5147.
- [7] M. Tagaya and M. Ogawa, *Phys. Chem. Chem. Phys.*, 10 (2008) 6849.
- [8] G. Baldacchini, P. Chiacchiarretta, R. Reisfeld and E. Zigansky, *J. Lumin.*, 129 (2009) 1849.
- [9] H. Bi, D. Chen, D. Li, Y. Yuan, D. Xia, Z. Zhang, H. Zhang and Y. Wang, *Chem. Commun.*, 47 (2011) 4135.
- [10] A. Curioni, M. Boero and W. Andreoni, *Chem. Phys. Lett.*, 294 (1998) 263.
- [11] M. Amati and F. Lelj, *Chem. Phys. Lett.*, 358 (2002) 144.
- [12] M. Amati and F. Lelj, *J. Phys. Chem. A*, 107 (2003) 2560.
- [13] H. Kaji, Y. Kusaka, G. Onoyama and F. Horii, *Jpn. J. Appl. Phys.*, 44 (2005) 3706.
- [14] H. Kaji, Y. Kusaka, G. Onoyama and F. Horii, *J. Am. Chem. Soc.*, 128 (2006) 4292.
- [15] M. M. Levichkova, J. J. Assa, H. Fröb and K. Leo, *Appl. Phys. Lett.*, 88 (2006) 201912.
- [16] L. L. Li, C. J. Fang, Q. Yuan and C. H. Yan, *Appl. Phys. Lett.*, 90 (2007) 231908.

- [17] H. Bi, H. Y. Zhang, Y. Zhang, H. Z. Gao, Z. M. Su and Y. Wang, *Adv. Mater.*, 22 (2010) 1631.
- [18] T. Tsuboi and Y. Torii, *Mol. Cryst. Liq. Cryst.*, 529 (2010) 42.
- [19] T. Tsuboi and Y. Torii, *J. Non-Cryst. Solids*, 356 (2010) 2066.
- [20] F. Suzuki, T. Fukushima, M. Fukuchi and H. Kaji, *J. Phys. Chem. C*, 117 (2013) 18809.
- [21] C. J. Pickard and F. Mauri, *Phys. Rev. B*, 63 (2001) 245101.
- [22] T. Fukushima and H. Kaji, *Org. Electron.*, 13 (2012) 2985.
- [23] M. Rajeswaran, T. N. Blanton and K. P. Klubek, *Z. Kristallogr. New Cryst. Struct.*, 218 (2003) 439.
- [24] Y. Nishiyama, T. Fukushima, K. Takami, Y. Kusaka, T. Yamazaki and H. Kaji, *Chem. Phys. Lett.*, 471 (2009) 80.

Chapter 6

Probing Intermolecular Structures of β Sheet of Alanine Oligomer and Silk Fibroin by High Resolution ^1H NMR Spectroscopy with Ultra-Fast MAS under Ultra-High Field ^1H Resonant Frequency

6.1. Introduction

The solid state crystalline structures in the chemical and biological materials are often dominated by the driving force of forming maximum of hydrogen bonds [1]. Investigations of hydrogen bonds, particularly their geometry, provide profound understandings of the structures and properties of the materials. Single crystal X-ray diffraction (XRD) is the most commonly used for the analysis of solid state crystal structures. However, determination of accurate positions of hydrogen atoms in the hydrogen bond network is usually not possible via XRD. As an alternative, ^1H solid state NMR is attractive for structural analysis because of its ubiquitous nature. ^1H is sensitive to intermolecular proximities because it locates on molecular surface and directly involved with hydrogen bonding. In particular, ^1H chemical shift is most simply interpreted in terms of intermolecular hydrogen bond such as $\text{NH}\dots\text{OC}$ interaction in oligo peptides and proteins [2-5]. Thus, the precise determination of ^1H chemical shift and subsequently accessible hydrogen bond distances lead to not only modification of hydrogen bond network geometry in heavy atom coordinates but also determination of unknown structures.

Polyalanine (poly-Ala) β sheet structures and their polymorph are key factors in the structure of silk fiber [6] and amyloid fibers [7, 8]. However, there have not been obtained β sheet single crystals longer than trimer that were large enough for XRD experiments. Therefore, the exact coordinate of heavy atoms in the β sheet structure for longer poly-Ala could so far not be described. To apply ^1H solid state NMR in determination of longer poly-Ala β sheet structures, which are

actually observed in silk and amyloid fibers, precise ^1H chemical shifts of poly-Ala should be confirmed based on known coordinates. For the purpose, it is required ^1H spectral resolution in the solid state especially NH region, which is broadened more than other protons because of residual dipolar splitting to the ^{14}N quadrupolar nuclei. ^1H NMR spectra of the crystalline antiparallel (AP) [9] and parallel (P) [10] β sheets of alanine trimer (Ala_3) were previously recorded, which the single crystalline X-ray structures were reported under ultra-high field (930 MHz of ^1H resonant frequency) with fast MAS (20 kHz) [11]. Amide NH and amino NH_3^+ ^1H signals of the P structure were well resolved, whereas they were not resolved for the AP structure. The results showed that N-H ^1H chemical shift was conveniently utilized as a diagnostic probe to distinguish the two structures. However, determination of further detailed structures such as NH...OC distances is not available due to still remained limited peak separation even under such an ultra-high field magnet.

Recent development of fast MAS technologies (up to 80 kHz [12]) gives ever more resolved spectra by decoupling ^1H - ^1H dipolar coupling network. This leads to additional applications of ^1H solid state NMR such as ^1H double quantum (DQ) spectroscopy [13-15] without careful synchronized rotations between the physical rotation of MAS and the nuclear spins using rf pulses, which is required in the combined rotation and multiple-pulse spectroscopy (CRAMPS) approach [16-18]. Moreover, it is expected that the combination of the ultra-fast MAS with the ultra-high field can increase in further resolution of ^1H spectra particularly NH group with quantitatively leading to assignment of NH protons in the poly-Ala.

In this Chapter, we presents ^1H chemical shifts of atomic coordinate known as AP and P β sheet structures of Ala_3 as a successful example of the solid state structure analysis of oligo peptides and proteins by high resolution ^1H NMR spectroscopy with ultra-high field 920 MHz and fast 70 kHz MAS. The high resolution ^1H - ^1H DQMAS approach with first principles

gauge-including projector augmented wave (GIPAW) chemical shift calculations for the full periodic crystal structure provides quantitative insight into intermolecular proximities from the relationship between chemical shifts of amide protons and intermolecular hydrogen bonding. Furthermore, we apply the analysis to discuss the hydrogen bonding character of *Bombyx mori* silk fibroin with different crystalline forms.

6.2. Experimental and computational section

6.2.1. Solid-state ^1H NMR experiment

Ala_3 were purchased from Bachem AG (Bubendorf, Switzerland). AP and P Ala_3 are prepared by the method reported previously [19]. The solid-state NMR experiments were performed at ^1H frequencies of 920 MHz using a JEOL JNM-ECA system equipped with JEOL 1.0 mm CP/MAS probes. The sample spinning speed was actively stabilized by a pneumatic solenoid valve so that the spinning fluctuations were less than ± 10 Hz. The ^1H rf field strength for the excitation $\pi/2$ pulse (1.29 μs) was 200 kHz. The ^1H chemical shift was referenced to the peak of silicon rubber and set to 0.12 ppm from TMS. For DQMAS, dipolar homonuclear homogeneous hamiltonian double-quantum/single-quantum (DQ–SQ) correlation measurement was employed [20]. This sequence consists of five pulses, which is identical to the refocused INADEQUATE sequence, and suffers less from the problems of B_1 inhomogeneity and frequency offset. The 2τ delay was optimized, and 0.3 ms giving maximum S/N was used.

6.2.2. Computation

The generalized gradient approximation (GGA) for the exchange correlation energy using the Perdew, Bruke and Ernzerhof (PBE) functional and ultrasoft pseudopotentials were used for

geometry optimization and the GIPAW chemical shift calculations. The geometry optimization was performed starting with the XRD crystal structure of AP [9] and P [10] Al₃, and applied only for protons under the periodic boundary condition. All calculations were carried out by the CASTEP program (Dassault Systèmes Biovia Corp., San Diego, CA, USA). ¹H NMR chemical shift calculations were carried out under the periodic boundary condition by the GIPAW module implemented in NMR-CASTEP for all the crystal structures. The PBE approximation and “On the fly” pseudopotentials were used. All the chemical shifts in this study are referenced by fitting a straight line of slope minus one to the plots of experimentally obtained chemical shifts against calculated chemical shifts.

6.3. Results and discussion

6.3.1. Solid-state ¹H NMR experiments

Figure 6.1a shows ¹H NMR spectra of the AP and the P Al₃ under the 920 MHz magnetic field with sample rotation rates of 17.8 kHz and 70.0 kHz on a 1 mm double resonance probe. At least three peaks are resolved for the amide NH, the H_α and the H_β regions from the lower to upper field for both MAS frequencies. For the spectra at 70.0 kHz, however, the NH region in P structure is clearly dissolved in two peaks at 9.0 and 7.4 ppm with an area ratio of 3:2, and even in AP a shoulder is visible, and the H_α region is also dissolved in two or three peaks. Further assignments of ¹H chemical shifts are anticipated from the highly resolved spectra by DQMAS.

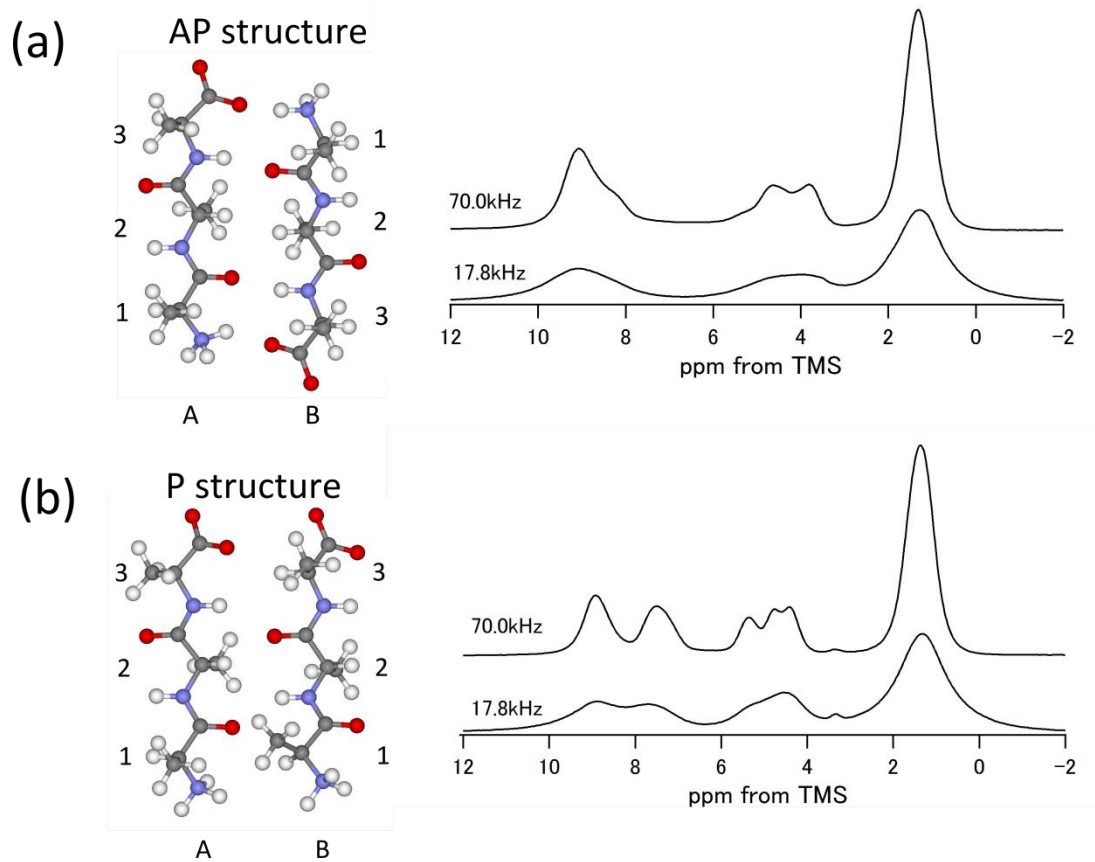


Fig. 6.1. Geometry optimized structures of (a) AP and (b) P β sheet structures of Ala₃, and their ¹H solid state NMR spectra with MAS rates of 17.8 and 70.0 kHz. Both structures have different A and B types molecules in a same lattice. The numbers of residues are listed from the N terminal.

6.3.2. DQMAS ^1H NMR experiments

Figure 6.2 shows DQMAS spectra of the AP and P Ala_3 . DQ–SQ correlation measurement was employed for the pulse sequence [20]. For DQMAS, correlation between indistinguishable protons such as NH_3 and CH_3 is observed as a diagonal peak (actually slope = 2). Therefore the peaks of NH_3 and NH protons are easily distinguished, leading to further assignment through cross peaks between NH and C_αH regions.

For AP Ala_3 , the NH_3 peak is estimated at 9.1 ppm from the diagonal peak. Cross peaks between NH_3 and H_α are observed at $\delta_{\text{DQ}} = 9.1+4.1 = 13.2$, $9.1+4.5 = 13.6$, $9.1+3.9 = 13.0$ ppm. Both AP and P structures of Ala_3 contain two different A and B type molecules as shown in Figure 6.1. Thus, two in the three peaks are probably due to difference in the environment of A and B structures. The XRD data suggest that the nearest intramolecular 1- H_α protons (for A type molecules, nearest proton in NH_3 ; 2.21 Å; in average of three protons of NH_3 ; 2.62 Å, for B type molecule, nearest 2.41 Å; average 2.63 Å), and intermolecular correlation with 3- H_α (for A, nearest 3.73 Å; average; 4.25 Å, for B, nearest 3.76 Å; average 4.34 Å) can be attributed to these cross peaks, and the stronger peaks at $\delta_{\text{DQ}} = 13.2$ and 13.6 ppm could be assigned to 1- H_α . Regarding proximities of 1- H_α and 3- H_α , only intermolecular proximities between 1- H_α and 3- H_α^* (2.43 and 2.57 Å) are available to show a cross peak. Thus, cross peaks at $\delta_{\text{DQ}} = 4.1+3.9 = 8.0$ ppm and $4.5+3.8 = 8.3$ ppm are estimated as intermolecular 1- H_α and 3- H_α proximities, resulting that the peaks at 3.9 and 3.8 ppm are estimated to 3- H_α . Consequently, the remained H_α peak at 4.7 ppm can be assigned to 2- H_α . Intermolecular distance between 2- H_α -2- H_α^* is 2.36 Å, therefore the diagonal peak of 2- H_α is a proof of this assignment. The peaks of 2- and 3-NH are assigned from the correlation with 2- and 3- H_α . 2- H_α should correlate with 2- and 3-NH in a same molecule (2.96 and 2.25 Å) whereas 3- H_α with only 3-NH (2.90 Å). Thus, the cross peak between 3- H_α and 3-NH should be $\delta_{\text{DQ}} = 3.8$ or $3.9+8.3 = 12.1$ or 12.2 ppm, which are difference

in A and B molecules, and that between 2-H_α and 2- and 3-NH are the two cross peaks at $\delta_{DQ} = 4.7+8.6 = 13.3$ ppm and $\delta_{DQ} = 4.7+8.3=13.0$ ppm, respectively.

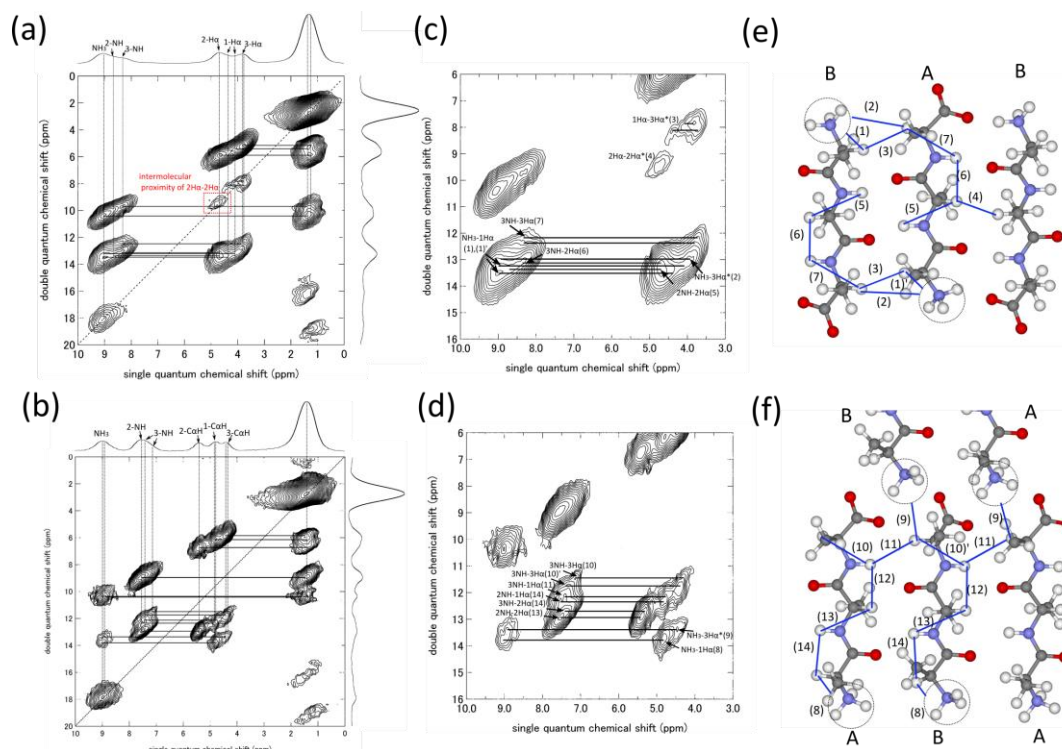


Fig. 6.2. ^1H DQMAS spectra for (a) anti-parallel and (b) parallel β sheet structures of Ala_3 . The expanded spectra at the NH and H_α regions are also shown in (c) for AP and (d) for P. The numbers of cross peak correspond to those in (e) and (f), respectively.

In contrast to AP, there is no diagonal H_α peak for P Ala_3 . A diagonal peak of H_α can be an indicator of intermolecular proximity up to 3.5 Å because there is no equivalent proton in the same molecule. In fact, the intermolecular distance 2- H_α -2- H_α^* is 4.98 Å. The assignment of chemical shifts for P Ala_3 is available in a similar way to AP although no H_α diagonal peaks are observed. The peak of NH_3 is assigned to 9.0 ppm from the diagonal peak. The area ratio of NH_3 and NH protons, 3:2, in the 1D spectrum corresponds with the assignment. The cross peaks between the NH_3 and H_α are apparent at $\delta_{DQ} = 9.0 + 4.9 = 13.9$ ppm with strong intensity and $\delta_{DQ} = 9.0 + 4.4 = 13.4$ ppm with weak intensity. The former is correlation with 1- H_α in a same residue (for A, nearest; 2.29 Å, average of three distances; 2.60 Å, for B, nearest; 2.33 Å, average; 2.63 Å), and the latter is intermolecular head-to-tail correlation with 3- H_α . (for $NH_3(A)$ - $H_\alpha(B)$, nearest; 2.81 Å, average; 3.22 Å, for $NH_3(B)$ - $H_\alpha(A)$, nearest; 3.07 Å, average 3.46 Å). Consequently, 2- H_α should be the remained peak at 5.5 ppm. 2- and 3-NH are assigned by the similar manner with AP except that intermolecular proximities of same residues between A and B molecules are observable. The assignments are consequently resulted in 2-NH = 7.5 ppm, and 3-NH = 7.2 and 7.4 ppm. The upfield shift of NH chemical shift of P structure in comparison to AP structure is consistent with weaker hydrogen bond due to longer NH...OC [21].

The assignments by the DQMAS measurements were validated by means of GIPAW chemical shift calculations. The calculations were performed based on the single crystal XRD data only (No-opt.) and that with geometry optimization of 1H position (H-opt.) as shown in Table 6.1. Note that the H-opt. chemical shifts markedly correspond with the experimental results in comparison to the No-opt. values as observed in the plots of the experimentally observed chemical shifts against the calculated chemical shifts (Figure 6.3). Surprisingly, a couple of differences in the chemical shifts of A and B type molecules in a same lattice are represented such as 1- H_α in AP and 3-NH in P. These results suggest that the localization of 1H is not possible based on X-

ray data as reported previously [22], and ^1H DQMAS with ultra-high field and fast MAS with GIPAW calculations provides very accurate hydrogen bond structure for a known structure of heavy atoms only as represented in Figure 6.4a and 6.4b.

^1H chemical shifts of NH in oligopeptides or proteins, as is well known, depend on hydrogen bonding length. Figure 6.4c shows the plot of the experimentally determined amide proton chemical shift values of AP and P Ala₃ against the hydrogen bond length between amide H and carbonyl O determined by XRD with GIPAW geometry optimization of ^1H position. ^1H chemical shifts of amide protons moved to downfield with decrease in hydrogen bond length. The physical origins for the correlation between chemical shift and hydrogen bond length are electric field effects, local magnetic anisotropies and a polarization of the electron cloud by the proximity of an oxygen atom, and in accordance with the following equation in the case without ring current shifts [2],

$$\delta = ad^3 + b, \quad (6.1)$$

From Eq. (6.1), we obtained

$$\delta_{\text{NH}} = 19.3d^3 + 5.9, \quad (6.2)$$

with 0.07 Å the root-mean-square deviation. The coefficient 19.3 ppm·Å³ is excellent agreement with the previously determined antiparallel β sheet in the basic pancreatic trypsin inhibitor (BPTI), 19.2 ppm·Å³, determined by liquid state NMR [2]. We previously reported the amide proton chemical shifts of (Ala-Gly)₁₅ for the crystalline domain of *Bombyx mori* silk fibroin in Silk I and Silk II structures by 2D ^1H - ^{15}N HETCOR experiment using 930 MHz NMR spectrometer although the linewidths of ^1H signals were slightly broader due to lower MAS rate 20kHz [23]. The values are 7.9 ppm (Ala) and 9.0 ppm (Gly) for Silk I, and 9.0 ppm (Ala) and 9.2 ppm (Gly) for Silk II. The hydrogen bond distances, $d(\text{NH}\dots\text{OC})$ can be calculated from the above equation, and to be 2.13 Å (AlaNH-GlyCO) and 1.84 Å (GlyNH-AlaCO) for Silk I. The

corresponding distances calculated from the ^1H -optimized Silk I structure are 2.01 and 1.85 Å. Thus, the calculated distance obtained from the observed chemical shift is in agreement with the ^1H optimized calculated distance given the lower resolution of the observed data. For the Silk II structure, the corresponding distances calculated from the structure reported by Marsh et al. [24], that includes only heavy atom coordinates and we added ^1H and modified their positions by the polymer consistent force field (PCFF) force field, were 1.77 Å (AlaNH-AlaCO) and 1.76 Å (GlyNH-GlyCO). The calculated distances from the chemical shift are 1.84 and 1.80 Å, respectively. Thus, the latter distances are also in agreement with the former ones.

Table 6.1. Experimental and calculated (GIPAW) ^1H isotropic chemical shifts (ppm) for AP and PAla₃ (single quantum).

		Expt.	Calc. No-opt. ^a	Calc. H-opt. ^a
AP Ala ₃	NH ₃	9.1	9.35(A), 7.52(B)	9.47(A), 9.41(B)
	2NH	8.6	5.38(A), 6.36(B)	9.14(A), 9.43(B)
	3NH	8.3	7.22(A), 7.85(B)	8.73(A), 8.40(B)
	1CH	4.5, 4.1	6.72(A), 6.03(B)	4.52(A), 4.05(B)
	2CH	4.7	5.16(A), 6.61(B)	4.86(A), 4.76(B)
	3CH	3.8, 3.9	5.24(A), 6.11(B)	3.85(A), 3.72(B)
P Ala ₃	NH ₃	9.0	7.18(A), 7.13(B)	9.31(A), 9.15(B)
	2NH	7.5	6.87(A), 6.87(B)	7.50(A), 7.61(B)
	3NH	7.4, 7.2	6.73(A), 6.49(B)	7.50(A), 7.26(B)
	1CH	4.9	4.95(A), 4.97(B)	4.75(A), 4.84(B)
	2CH	5.5	5.80(A), 5.58(B)	5.52(B), 5.44(B)
	3CH	4.4	4.50(A), 4.57(B)	4.37(A), 4.55(B)

^a The calculated ^1H chemical shifts are referenced to the average of three chemical shifts of CH₃, and set to experimentally obtained values, 1.30 ppm for AP and 1.36 ppm PAla₃.

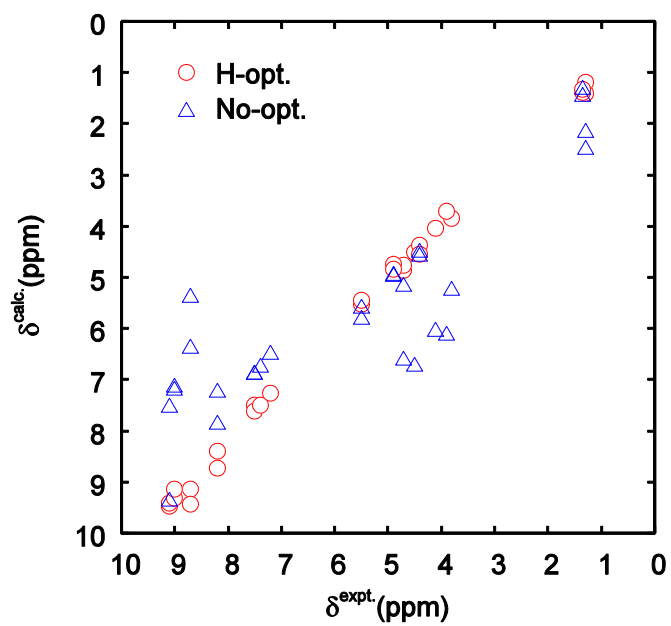


Fig. 6.3. Comparison of experimentally observed ($\delta^{\text{expt.}}$) and calculated ($\delta^{\text{calc.}}$) ^1H chemical shifts. For NH_3 and CH_3 , three calculated ^1H chemical shifts are averaged.

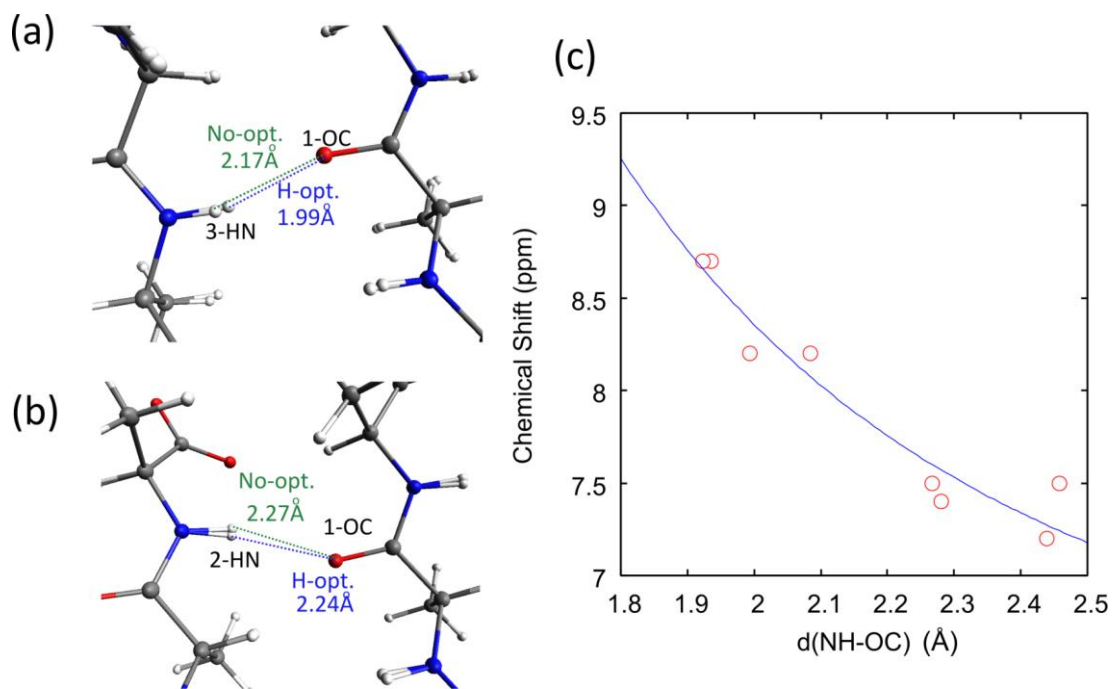


Fig. 6.4. Representations of difference in hydrogen bond distance between No-opt. and H-opt. for (a) 3NH(A)-1OC(B) in AP Ala₃ and (b) 2NH(A)-1OC(B) in P Ala₃. (c) The plot of the experimentally determined ¹H chemical shifts for the hydrogen-bonded amide protons in AP and P β sheet structures of Ala₃ vs. the distance between these protons and the nearest oxygen atoms.

6.4. Conclusion

In this Chapter, ^1H chemical shifts of antiparallel and parallel β sheet structures of alanine trimer are assigned by using DQMAS measurements with ultra-high field and ultra-fast MAS NMR. The assignments are consistent with the chemical shift calculation by first principles GIPAW approach for ^1H geometry optimized structures. This is, to the best of our knowledge, the first attempt analyzing the relationship between ^1H chemical shifts and intermolecular hydrogen bonding in the solid state for antiparallel and parallel β sheet structures of alanine trimer. The equation obtained will be applied for analyses of intermolecular hydrogen bond distances of peptides and proteins. High-resolution ^1H solid state NMR with GIPAW calculation provided precise ^1H positions. In particular, the chemical shifts of amide protons are described by the inverse third power distance of intermolecular $\text{NH}\dots\text{OC}$ hydrogen bond. This relationship can be used to evaluate intermolecular $\text{NH}\dots\text{OC}$ hydrogen bond distances of peptides and proteins in the solid state from amide proton chemical shifts.

(Chapter 6 is the unedited Author's version of a Submitted Work that was subsequently accepted for publication in *Chem. Commun.* copyright © Royal Chemical Society after peer review. To access the final edited and published work see the following website:

<http://pubs.rsc.org/en/content/articlepdf/2012/cc/c2cc36300c>)

REFERENCES

- [1] D. F. Sticke, L. G. Presta, K. A. Dill and G. D. Rose, *J. Mol. Biol.*, 226 (1992) 1143.
- [2] G. Wagner, A. Pardi and K. Wuethrich, *J. Am. Chem. Soc.*, 105 (1983) 5948.
- [3] K. Yamauchi, S. Kuroki, K. Fujii and I. Ando, *Chem. Phys. Lett.*, 324 (2000) 435.
- [4] T. Asakura, K. Taoka, M. Demura and M. Williamson, *J. Biomol. NMR*, 6 (1995) 227.
- [5] J. M. Griffin, D. R. Martin and S. P. Brown, *Angew. Chem.*, 119 (2007) 8182.
- [6] J. D. van Beek, L. Beaulieu, H. Schafer, M. Demura, T. Asakura and B. H. Meier, *Nature*, 405 (2000) 1077.
- [7] R. Nelson, M. R. Sawaya, M. Balbirnie, A. O. Madsen, C. Riekel, R. Grothe and D. Eisenberg, *Nature*, 435 (2005) 773.
- [8] J.-P. Colletier, A. Laganowsky, M. Landau, M. Zhao, A. B. Soriaga, L. Goldschmidt, D. Flot, D. Cascio, M. R. Sawaya and D. Eisenberg, *Proc. Natl. Acad. Sci. USA*, 108 (2011) 16938.
- [9] J. K. Fawcett, N. Camerman and A. Camerman, *Acta Crystallogr. B*, 31 (1975) 658.
- [10] A. Hempel, N. Camerman and A. Camerman, *Biopolymers*, 31 (1991) 187.
- [11] Y. Suzuki, M. Okonogi, K. Yamauchi, H. Kurosu, M. Tansho, T. Shimizu, H. Saito and T. Asakura, *J. Phys. Chem. B*, 111 (2007) 9172.
- [12] Y. Nishiyama, Y. Endo, T. Nemoto, H. Utsumi, K. Yamauchi, K. Hioka and T. Asakura, *J. Magn. Reson.*, 208 (2011) 44.
- [13] I. Schnell and H. W. Spiess, *J. Magn. Reson.*, 151 (2001) 153.
- [14] S. P. Brown, A. Lesage, B. Elena and L. Emsley, *J. Am. Chem. Soc.*, 126 (2004) 13230.
- [15] S. P. Brown, *Prog. Nucl. Magn. Reson. Spectrosc.*, 50 (2007) 199.
- [16] B. C. Gerstein, R. G. Pembleton, R. C. Wilson and L. M. Ryan, *J. Chem. Phys.*, 66 (1977) 361.

- [17] L. Mafra, J. R. B. Gomes, J. Trébosc, J. Rocha and J.-P. Amoureux, *J. Magn. Reson.*, 196 (2009) 88.
- [18] J. P. Bradley, S. P. Velaga, O. N. Antzutkin and S. P. Brown, *Cryst. Growth Des.*, 11 (2011) 3463.
- [19] T. Asakura, M. Okonogi, Y. Nakazawa and K. Yamauchi, *J. Am. Chem. Soc.*, 128 (2006) 6231.
- [20] M. Deschamps, F. Fayon, S. Cadars, A.-L. Rollet and D. Massiot, *Phys. Chem. Chem. Phys.*, 13 (2011) 8024.
- [21] L. Yao, A. Grishaev, G. Cornilescu and A. Bax, *J. Am. Chem. Soc.*, 132 (2010) 4295.
- [22] L. Seyfarth and J. Senker, *Phys. Chem. Chem. Phys.*, 11 (2009) 3522.
- [23] Y. Suzuki, R. Takahashi, T. Shimizu, M. Tansho, K. Yamauchi, M. P. Williamson and T. Asakura, *J. Phys. Chem. B*, 113 (2009) 9756.
- [24] R. E. Marsh, R. B. Corey and L. Pauling, *Biochim. Biophys. Acta*, 16 (1955) 1.

Summary

In this thesis, the author studied molecular structure and its relationship to light-emission and charge-transport properties of materials for organic light-emitting diodes (OLEDs), using charge transport simulations, solid-state NMR, and first-principle calculations. The author established the promising approaches to directly link macroscopic emission and charge-transfer properties with microscopic molecular structures. The author also applied the approaches to reveal the structure-property relationships of biological-based materials. The results and findings in the respective chapters are summarized as follows:

In the Chapter 2, multiscale charge transport simulations for amorphous structures of *N,N'*-dicarbazole-3,5-benzene (mCP), which has been widely used as a host material for blue-emitting organic light-emitting diodes, was performed. Organic molecules were explicitly considered in order to link the macroscopic charge transfer and the microscopic molecular structure directly. The calculated hole mobility of mCP was three to four times larger than the electron mobility, which was in good agreement with the experimentally determined ratio of the charge mobility for hole and electron transfer. It was also clearly found that while the diffusion transport was dominant at low applied electric fields, the contribution of the drift transport increases as the applied electric field increased. At a low electric field strength, both holes and electrons reached the counter electrode not through simple routes directly toward the direction of the applied electric field but through complicated routes, including the direction opposite to and perpendicular to the electric field. At a high electric field strength, charge hopping in the direction of the applied electric field can be advantageous and becomes significantly efficient. The contribution of respective molecular pairs to whole charge transport were also investigated. Charge hopping for molecular pairs with large

electronic coupling was mainly diffusive; hopping in both the forward and backward directions occurs frequently with almost equal probability. Therefore, these molecular pairs are not crucial for charge transports. We found other important molecular pairs, which improve charge mobilities and form effective charge transfer path, although the electronic coupling was not substantially large.

In the Chapter 3, molecular-level charge transport simulations were performed to investigate the effect of off-diagonal (structural) and diagonal (energetic) disorder on charge transport using thin layer of *N,N'*-diphenyl-*N,N'*-bis(1-naphthyl)-1,1'-biphenyl-4,4'-diamine (NPD) in the crystal and the amorphous phase. The molecular origin of bipolar charge transport ability of NPD in amorphous phase was also examined. Both the crystal and the amorphous phase were found to exhibit electron transport ability as well as hole transport ability. Experimental charge mobility and its applied electric field dependence in the amorphous thin layer were qualitatively reproduced by the charge transport simulation, especially for electron transfer. Intermolecular spatial overlap between LUMOs on naphthyl segments was found to provide effective electron transport. In the crystal phase, charges showed linear and less diffusional transport. On the other hand, complicated and strongly diffusive routes were observed in the amorphous phase under low applied electric field. However, under higher applied electric field, charge transport pathway in the amorphous phase became similar with that of the crystal phase. It was found that not only applied electric field strength but also structural disorder play a major role for the linearity of charge transport pathway. Energetic disorder plays a significant role to the applied electric field dependence of charge transport. These characteristics can be well understood by the analysis of different hopping probability from a molecule to various adjacent molecules. The charge-hopping probability to move out of each molecular pair is proposed to be a key factor for the degree of contribution of the molecular pair to charge transport.

In the Chapter 4, the intra- and intermolecular structures of an important organic device material, tris(8-hydroxyquinoline) aluminum(III) (Alq_3), in the γ and δ crystalline forms, were analyzed by the combined use of cross polarization/magic-angle spinning (CP/MAS) ^{13}C NMR experiments and gauge-including projector-augmented wave (GIPAW) chemical-shift calculations. It had been difficult to clearly distinguish the intra- and/or intermolecular origins of the blue shift of light emission from these Alq_3 polymorphs. In this Chapter, the investigation on origin of blue-emission of these newly appearing Alq_3 was successfully demonstrated. The crystal structures determined by wide-angle X-ray diffraction (WAXD) method were refined for $\gamma\text{-Alq}_3$ and $\delta\text{-Alq}_3$ by the above combined approach. CP/MAS ^{13}C NMR spectrum provided the single resonance lines for respective carbon species of $\gamma\text{-Alq}_3$. The result shows that $\gamma\text{-Alq}_3$ consists of *facial* isomers and indicates that the three ligands are equivalent not only in terms of intramolecular interaction, but also in terms of intermolecular interaction. In contrast, in the CP/MAS ^{13}C NMR spectrum of $\delta\text{-Alq}_3$, the splittings of resonance lines were observed for the respective carbon species. GIPAW calculation was also performed for the isolated molecules extracted from $\gamma\text{-Alq}_3$ and $\delta\text{-Alq}_3$ crystals. It was clearly shown that the isolated Alq_3 molecules have similar intramolecular structures exclusively in *facial* form, and provide similar isotropic chemical shifts when the intermolecular interactions are neglected. Therefore, the resonance line splitting for the $\delta\text{-Alq}_3$ crystals is definitely found to originate from the intermolecular packing effect, not from the intramolecular interaction. The GIPAW calculations clearly show that γ - and $\delta\text{-Alq}_3$ have basically the same intramolecular structure, but have different intermolecular structures. These differences are important for the understanding of structure–property relationship. Both $\gamma\text{-Alq}_3$ and $\delta\text{-Alq}_3$ crystals have unconventional blue emission with similar photoluminescence spectra, although they have different intermolecular packing. The intra- and intermolecular structures of $\gamma\text{-Alq}_3$ and $\delta\text{-Alq}_3$

determined in this Chapter indicate that the *facial* isomeric states are the origin of the blue emission, not the intermolecular interactions. The crystal structures determined by WAXD analysis were refined for both γ -Alq₃ and δ -Alq₃ through the combined use of solid-state NMR and GIPAW calculations. Atomic coordinate displacements of the carbons between the H-optimization and ALL-optimization are within 0.2 Å. The distinction is difficult by WAXD analysis. However, NMR isotropic chemical shift is very sensitive to such small structural changes.

In the Chapter 5, a further joint analysis by the combined use of ¹H dipolar decoupled (DD) ²⁷Al MAS NMR and GIPAW calculations were performed on blue-emitting γ - and δ -Alq₃ crystals and the isolated molecules extracted from the crystals utilized in the Chapter 4. As shown in the Chapter 4, ¹³C CP/MAS NMR is very sensitive to the intermolecular interactions in each crystal and the intramolecular structures of Alq₃ in γ - and δ -Alq₃ are similar. In contrast to the isotropic chemical shifts obtained by ¹³C CP/MAS NMR experiments, NMR quadrupolar parameters obtained by DD/MAS ²⁷Al NMR are found to be insensitive to intermolecular interactions but very sensitive to intramolecular structures. Generally, NMR parameters, such as chemical shifts, quadrupolar coupling constants, and anisotropy parameters (η_q), depend on both the intra- and intermolecular structures, which makes structure analysis difficult. However, in the present case, ²⁷Al NMR does not depend on intermolecular interactions in a good approximation, which enables us to carry out precise intramolecular structure determination without considering intermolecular interactions. From the complementary analyses of ¹³C and ²⁷Al NMR, it was found that the origin of the non-zero η_q value of δ -Alq₃ crystal is not the intermolecular interaction, but the structural deviation of Alq₃ from C₃ symmetry. From these results, it can be reasonably conclude that neither the different intermolecular packings nor deviation from C₃ symmetry affect the emission wavelengths.

The origin of a different emission color of these newly-appeared Alq₃ compared with normal green emission must be that the molecules in these crystals are *facial* isomers. The complementary GIPAW analyses of ¹³C and ²⁷Al NMR described in Chapters 4 and 5 will be extremely useful for the analysis of amorphous systems.

In the Chapter 6, it was proved that the robustness of the combined approach of GIPAW calculation and solid-state NMR spectroscopy by structural investigation of the biological-based materials, crystals of alanine tripeptides (Ala₃). ¹H chemical shifts of Ala₃ in parallel and anti-parallel β sheet structures are both assigned by using double-quantum MAS measurements with ultra-high field and ultra-fast MAS NMR. The comparison of high resolution ¹H solid-state NMR with GIPAW calculation provided precise ¹H coordinates, including the hydrogen bonding systems. The determined chemical shifts of the amide protons could be described by a function of the intermolecular NH...OC distance. This relationship can be used to evaluate intermolecular NH...OC hydrogen bond distances of peptides and proteins in the solid state from amide proton chemical shifts.

In this thesis, the author aimed to analyze the fundamental relationship between light-emission and charge-transport properties and molecular structures of OLED materials. The results and findings are important not only for fundamental science but also for design of excellent luminescent and charge-transport materials. Combining the simple CP/MAS (or MAS) + GIPAW approach with atomistic charge transport simulation established in this thesis will further develop our understanding of material properties of organic crystals and thin films. In future, we will apply these approaches to amorphous systems, especially for multi-layered amorphous systems composed of hole transport, emission, and electron transport layers, and for more complex systems containing charge (or exciton) blocking layers, charge injection layers, and metal electrodes. For this purpose, sufficiently large-scaled amorphous structures are

needed to be considered as initial coordinates. At present, it is almost impossible to carry out GIPAW calculation for more than several tens of molecules because of the limitation of computational time. However, in near future, increasing computation speed can make possible precise structural analysis of large-scaled systems by simple CP/MAS (or MAS) experiments and GIPAW calculations in addition to charge transport simulation. This will enable us to develop more sophisticated strategies for designing advanced OLED materials.

List of Publication

Chapter 2

“Multiscale simulation of charge transport in a host material, *N,N'*-dicarbazole-3,5-benzene (mCP), for organic light-emitting diodes”

F. Suzuki, K. Shizu, H. Kawaguchi, S. Furukawa, T. Sato, K. Tanaka, H. Kaji

J. Mater. Chem. C 3 (2015) 5549-5555.

(Chapter 2 is the unedited Author's version of a Submitted Work that was subsequently accepted for publication in *J. Mater. Chem. C* copyright © Royal Chemical Society after peer review. To access the final edited and published work see the following website:

<http://pubs.rsc.org/-/content/articlelanding/2015/tc/c5tc00543d>)

Chapter 3

“Effect of Structural and Energetic Disorder on Charge Hopping in Amorphous Organic Thin Layer by Multiscale Charge Transport Simulation”

To be submitted.

Chapter 4

“Refined Structure Determination of Blue-Emitting Tris(8-Hydroxyquinoline) Aluminum(III) (Alq₃) by the Combined Use of Cross-Polarization/Magic-Angle Spinning ¹³C Solid-State NMR and First-Principles Calculation”

F. Suzuki, T. Fukushima, M. Fukuchi, H. Kaji

J. Phys. Chem. C 117 (2013) 18809-18817.

(Chapter 4 is the unedited Author's version of a Submitted Work that was subsequently

accepted for publication in *J. Phys. Chem. C*, copyright © American Chemical Society after peer review. To access the final edited and published work see the following website:

<http://pubs.acs.org/doi/abs/10.1021/jp404430v>)

Chapter 5

“Clarification of isomeric structures and the effect of intermolecular interactions in blue-emitting aluminum complex Alq₃ using first-principles ²⁷Al NMR calculations”

F. Suzuki, Y. Nishiyama, H. Kaji

Chem. Phys. Lett. 605-606 (2014) 1-4.

(Chapter 5 is the unedited Author’s version of a Submitted Work that was subsequently accepted for publication in *Chem. Phys. Lett*, copyright © Elsevier B.V after peer review.

To access the final edited and published work see the following website:

<http://dx.doi.org/10.1016/j.cplett.2014.05.015>)

Chapter 6

“Determination of accurate ¹H positions of an alanine tripeptide with anti-parallel and parallel β-sheet structures by high resolution ¹H solid state NMR and GIPAW chemical shift calculation”

K. Yazawa, F. Suzuki, Y. Nishiyama, T. Ohata, A. Aoki, K. Nishimura, H. Kaji, T. Shimizu, T. Asakura

Chem. Commun. 48 (2012) 11199-11201.

(Chapter 6 is the unedited Author’s version of a Submitted Work that was subsequently accepted for publication in *Chem. Commun.* copyright © Royal Chemical Society after peer

review. To access the final edited and published work see the following website:

<http://pubs.rsc.org/en/content/articlepdf/2012/cc/c2cc36300c>

Other Publications

““114”-Type Nitrides $\text{LnAl}(\text{Si}_{4-x}\text{Al}_x)\text{N}_7\text{O}_8$ with Unusual $[\text{AlN}_6]$ Octahedral Coordination”

S. Huang, Z. Huang, P. Cao, Z. Zujovic, J. R. Price, M. Avdeev, M. Que, F. Suzuki, T. Kido, X. Ouyang, H. Kaji, M. Fang, Y. Liu, W. Gao, T. Söhnel

Angew. Chem. Int. Ed. 56 (2017) 3886-3891; *Angew. Chem.* 129 (2017) 3944-3949.

“Detailed Analysis of Charge Transport in Amorphous Organic Thin Layer by Multiscale Simulation without Any Adjustable Parameters”

H. Uratani, S. Kubo, K. Shizu, F. Suzuki, T. Fukushima, H. Kaji

Sci. Rep. 6 (2016) 39128.

“Purely organic electroluminescent material realizing 100% conversion from electricity to light”

H. Kaji, H. Suzuki, T. Fukushima, K. Shizu, K. Suzuki, S. Kubo, T. Komino, H. Oiwa, E. Suzuki, A. Wakamiya, Y. Murata, C. Adachi

Nat. Commun. 6 (2015) [8476-1]-[8476-8].

“Intermolecular Packing in *B. mori* Silk Fibroin: Multinuclear NMR Study of the Model Peptide $(\text{Ala-Gly})_{15}$ Defines a Heterogeneous Antiparallel Antipolar Mode of Assembly in the Silk II form”

T. Asakura, T. Ohata, S. Kametani, K. Okushita, K. Yazawa, Y. Nishiyama, K. Nishimura, A.

Aoki, F. Suzuki, H. Kaji, A. S. Ulrich, M. P. Williamson

Macromolecules 48 (2015) 28-36.

"On-Top π -Stacking of Quasiplanar Molecules in Hole-Transporting Materials: Inducing Anisotropic Carrier Mobility in Amorphous Films"

A. Wakamiya, H. Nishimura, T. Fukushima, F. Suzuki, A. Saeki, S. Seki, I. Osaka, T. Sasamori, M. Murata, Y. Murata, H. Kaji

Angew. Chem. Int. Ed. 53 (2014) 5800-5804; *Angew. Chem.* 126 (2014) 5910-5914.

"A designed fluorescent anthracene derivative: Theory, calculation, synthesis, and characterization"

M. Uejima, T. Sato, M. Detani, A. Wakamiya, F. Suzuki, T. Fukushima, K. Tanaka, Y. Murata, C. Adachi, H. Kaji

Chem. Phys. Lett. 602 (2014) 80-83.

"Difference in the Structures of Alanine Tri- and Tetra-Peptides with Antiparallel β -Sheet Assessed by X-Ray Diffraction, Solid-State NMR and Chemical Shift Calculations by GIPAW

T. Asakura, K. Yazawa, K. Horiguchi, F. Suzuki, Y. Nishiyama, K. Nishimura, H. Kaji

Biopolymers 101 (2014) 13-20.

"Determination of Accurate ^1H Positions of (Ala-Gly) $_n$ as a Sequential Peptide Model of *Bombyx mori* Silk Fibroin before Spinning (Silk I)"

T. Asakura, Y. Suzuki, K. Yazawa, A. Aoki, Y. Nishiyama, K. Nishimura, F. Suzuki, H. Kaji

Macromolecules 46 (2013) 8046-8050.

“Structure and crystallization of sub-elementary fibrils of bacterial cellulose isolated by using a fluorescent brightening agent”

S. Suzuki, F. Suzuki, Y. Kanie, K. Tsujitani, A. Hirai, H. Kaji, F. Horii

Cellulose 19 (2012) 713-727.

“Fusion of Phosphole and 1,1'-Biacenaphthene: Phosphorus(V)-Containing Extended π -Systems with High Electron Affinity and Electron Mobility”

Y. Matano, A. Saito, T. Fukushima, Y. Tokudome, F. Suzuki, D. Sakamaki, H. Kaji, A. Ito, K. Tanaka, H. Imahori

Angew. Chem. Int. Ed. 50 (2011) 8016-8020; *Angew. Chem.* 123 (2011) 8166-8170.

“Revealing bipolar charge-transport property of 4,4'-*N,N'*-dicarbazolylbiphenyl (CBP) by quantum chemical calculations”

T. Yamada, F. Suzuki, A. Goto, T. Sato, K. Tanaka, H. Kaji

Org. Electron. 12 (2011) 169-178.

Acknowledgements

The studies presented in this thesis were carried out under the direction of Professor Hironori Kaji at Institute for Chemical Research, Kyoto University. The author would like to express his gratitude to Professor Hironori Kaji for his invaluable suggestion and kind guidance throughout the study.

The author is grateful to Professor Masahiro Shirakawa and Professor Hirofumi Sato, Department of Molecular Engineering, Graduate School of Engineering, Kyoto University, for their guidance in preparing this thesis.

Sincere appreciation is due to Professor Kazuyoshi Tanaka and Associate Professor Tohru Sato, Department of Molecular Engineering, Graduate School of Engineering, Kyoto University, for their enormous contributions in this study. The author is sincerely grateful to Professor Tetsuo Asakura, Department of Biotechnology, Tokyo University of Agriculture and Technology, for his active collaborations in this study. The author would like to express my sincere appreciation to Dr. Yusuke Nishiyama at RIKEN CLST-JEOL collaboration center and JEOL RESONANCE, for his considerable efforts. The author would like to express my gratitude to Dr. Koji Yazawa at JEOL RESONANCE, Associate Professor Katsuyuki Nishimura at Institute for Molecular Science and Dr. Tadashi Shimizu at National Institute for Materials Science, for their contributions in this study.

The author would like to express my gratitude to Associate Professor Atsushi Wakamiya and Professor Yasujiro Murata at Institute for Chemical Research, Kyoto University, for their collaborations and warm encouragements. The author is deeply grateful to Professor Chihaya Adachi, Center for Organic Photonics and Electronics Research, Kyushu University, for his significant contribution. The author would also like to express my gratitude to Professor

Shuhei Seki, Department of Molecular Engineering, Graduate School of Engineering, Kyoto University, for his active collaboration in this study. Sincere appreciation is due to Professor Hiroshi Imahori, Department of Molecular Engineering, Graduate School of Engineering, Kyoto University, for his collaboration and generous support in this study. The author would also like to thank to Professor Fumitaka Horii, Department of Molecular Engineering, Graduate School of Engineering, Kyoto University, for his helpful guidance. The author is particularly grateful to Associate Professor Tilo Söhnle, Dr. Saifang Huang and Dr. Scott Kang at the University of Auckland, for their kind assistance and contributions during the author's sabbatical research. Thanks are also given to other colleagues in the University of Auckland.

The author is sincerely grateful to Dr. Tomonori Yamada, Mr. Hisafumi Kawaguchi, Mr. Shinya Furukawa, Dr. Tatsuya Fukushima, Dr. Masashi Fukuchi, Dr. Katsuyuki Shizu, Mr. Tsuyoshi Kido, Mr. Yoshimasa Wada and Mr. Shosei Kubo at Institute for Chemical Research, Kyoto University, for their helpful collaborations and suggestions during this study. The author acknowledges to his colleagues, Mr. Yasunari Kusaka, Dr. Nawoki Tsukamoto and Mr. Masatoshi Fujinaka for their useful discussion and encouragement. Thanks are also given to other staffs and students in Institute for Chemical Research, Kyoto University, for their kindness during this study. The author sincerely appreciates the help of Mr. Shin Aihara, Mr. Tetsuya Okano, Mr. Masatsugu Ito, Mr. Nobuhiro Nishizawa and Mr. Shigeru Tamura at KAO Corporation, who provided a view-broadening opportunity.

Finally, the author heartily wishes to express his thanks to his wife, Yuko Suzuki, his children, Miko Suzuki, Amane Suzuki, his parents-in-law, Chie Nishiguchi, Yoshihisa Nishiguchi, his parents, Tamiyo Suzuki, Yoshinori Suzuki and all his relatives.

Furitsu Suzuki